Development of Flexible Parylene-Based Microtechnologies for Retinal and Spinal Cord Stimulation and Recording

Thesis by

Damien Craig Rodger

In Partial Fulfillment of the Requirements
for the Degree of

Doctor of Philosophy

California Institute of Technology

Pasadena, California

2008

(Defended August 9, 2007)

To my family and friends

Acknowledgements

My scholarly endeavors, of which the research contained within the pages of this dissertation is a major piece, could never have been possible if it were not for the many people who have encouraged me to use every moment of my life as a lesson to be learned. It is to all of these people that I am indebted. It would be an impossible task to mention all the people who have had a profound impact on my life, so I will only hope to try.

My teachers and mentors throughout my life, from preschool in England to medical studies at the University of Southern California and my graduate studies at the California Institute of Technology have imparted on me a real gift, the love of learning. To each and every teacher I have had, thank you.

My interest in MEMS was cultivated during my freshman year at Cornell University by Dr. Noel MacDonald, who was my undergraduate advisor and enabled me to work in his lab, along with Noel Elman, despite my lack of knowledge of the field at the time. It was he who encouraged me to think about the possibilities of MEMS in medicine, an idea that has led me here. Had I not worked with him and Dr. Kimberly Turner my first year, I could not even hazard a guess as to where I would be right now. While there, I was blessed to be mentored by Dr. Thomas Kudrle, whose lessons on all things MEMS as well as all things life, and on how to do top-notch research while maintaining a sense of humor, have served invaluable. Dr. Hercules Neves was also a source of encouragement, knowledge, and humor during my time at Cornell. I would also like to thank Dr. Carlo Montemagno for enabling me to perform novel and exciting bioMEMS research in his lab at Cornell.

All those I worked with at JPL were some of the most amazing people I have ever met. The level of professionalism, while maintaining a crucial sense of fun, was incredible. Dr. Tony Tang always believed in my abilities, and directed me in very significant work with kind, but trusting, oversight. He was a further source of encouragement for my medical pursuits, and is a trusted colleague and friend. I learned a great deal about MEMS late at night and on weekends at JPL from two great people, Dr. Stephen Vargo and Dr. Victor White. Their achievements, mixed with their sense of humor, always led to interesting discussions. I would also like to thank Drs. Bill Tang, Gisela Lin, Linda Miller, Roman Gutierrez, and many others for their knowledge and kindness.

If it were not for Dr. Yu-Chong Tai, I know I would not be where I am now. His love of what he does, coupled with his incredible knowledge, ideas, and insight are inspiring and very infectious. Indeed, after my first meeting with him, I knew that the Caltech Micromachining Laboratory is where I wanted to work for my PhD. His desire and ability to put his students first and foremost, despite the incredible pressures of academia, is incontrovertible. His work is of such high caliber, while at the same time he is a lesson in modesty. I can not express how much of a pleasure it has been to work in Dr. Tai’s lab, and I have learned so many important life lessons under his tutelage. I can only hope my collaboration with him will continue far into the future. If anyone is going to bring MEMS and engineering to solve the most important problems in medicine and life, I know it will be with his contribution. We are all blessed to be able to call ourselves his students.

Matthieu Liger was an incredible person to be able to work alongside in my first year in the Caltech Micromachining Lab. I learned an incredible amount about parylene processing from him, and am indebted to him for all that I know now. To Wen Li and Po-Jui Chen, thank you so much for enabling me to work alongside you and support you in your efforts as well. You are both incredible researchers who have furthered the field of bioMEMS, and you are also great friends, and I know you will both go very far in your lives, no matter what work you choose in the end. I also wish to thank my officemates (at one point or another) Ellis Meng, Justin Boland, and Scott Miserendino for humorous conversations and the knowledge you have instilled in me. And Quoc (Brandon) Quach for conversations, banter, and lunches at Ernie's. The other members of the Caltech Micromachining Lab during my tenure there have also been incredible colleagues: Angela Tooker, Ted Harder, Jun Xie, Jason Shih, Victor Shih, Nick Lo, Changlin Pang, Siyang Zheng, Mike Liu, Ray Huang, Monty Nandra, Luca Giacchino, Jeffrey Chun-Hui Lin, Justin Kim, and Juhwan Yoo. You are all amazing scholars, and I appreciate being able to call myself your colleague as well. To my undergraduate mentee, Parvathy Menon, thanks so much for working with us and helping in our understanding of parylene as a bioMEMS material for the retinal prosthesis. You are an incredible student, and I know you will go far. Thanks to Trevor Roper for maintaining equipment and especially helping to get all the equipment I needed for my research working at the drop of a hat. Thank you to Tanya Owen and Christine Matsuki for everything you have done for me.

Thanks should also be extended to Dr. Tai’s family for their friendliness and their amusing, voluminous, eating habits at group dinners.

I feel blessed that Dr. Mark Humayun came to the University of Southern California at approximately the same time that I did. I knew I wanted to work in the bioMEMS field and with parylene, but did not have a specific project in mind until I met him in his office. Since then, it has been an unbelievable journey that I feel is only just beginning. His incredible intuition about how to interface engineering with medicine to solve profound human disease is awe inspiring. It is not just about having intuition, but also actually being able to act on it while also being incredibly even keeled under pressure, as he has demonstrated. His modesty about the sea change he has fathered in ophthalmology is a lesson in itself. Dr. Humayun: the respect that your patients have for you is incredibly telling, because it shows how effortlessly you can interface with people from all spheres of life, and shows how genuine you are. Thank you for everything. I am lucky to have been able to get to know you as a mentor, a doctor, and as a friend, and hope I can put all the knowledge you have given to me to good use. I look forward to many more years of collaboration and friendship.

To Dr. James Weiland, thank you also for bringing me into your lab and having such important input in my work. You are an amazing researcher, teacher, and friend. It is rare that a P.I. be so universally respected and positively regarded by his students, but you are one of these people. Thank you for everything. To everyone in Jim’s lab, especially Ashish Ahuja, Matthew Behrend, and Aditi Ray: thank you for your knowledge, humor, insight, and support. Thanks especially to Doris Lee, and all the other administrative help at the BMES ERC. You are all such incredible people, and I know that this research would not be able to go on without you there.

To my other coauthors and colleagues, especially Drs. Ellis Meng and Hossein Ameri, I am blessed to have been able to work with you all. You are true scholars.

To my committee, Drs. Yu-Chong Tai, Joel Burdick, Mory Gharib, Ellis Meng, and James Weiland: thank you for all of your input, intelligent and creative insight into my work, and suggestions for improvement and strengthening of my work over these four years. You are amazing scientists, engineers, and colleagues, and I am lucky to have had such incredible support and interest from you all for the duration of this project.

My transition from USC to Caltech (and back) could not have gone as seamlessly as it has without the help of Sandy Mosteller, Roland Rapanot, and the MD/PhD program. Thank you for everything you do, every day, for each and every one of us.

To all my friends from medical school: you know who you are. Thanks for everything you have done for me and all the fun times we have had. You are all incredible people and current and future doctors and I wish you all the best in everything you do. I never want to lose touch with any of you. To my friends from Concord Academy and Cornell, thanks for always supporting me despite my quirks!

Andy Fong has been an incredible source of friendship and support during my time at Caltech. I know we will be friends for the rest of our lives, and I wish you all the best in your future endeavors as well. Thanks and best of luck to the Bioengineering Class of 2003. I do not think our first year could have been any better, despite it being so hard!

The amazing individuals who have volunteered themselves and their time, for such selfless reasons, to be pioneers as subjects for the study of these devices, you can not be thanked enough for your devotion to humanity and science. Your insights are invaluable, and you have served as an inspiration to me, every day, for this work.

This research was supported in part by the Engineering Research Centers Program of the National Science Foundation under NSF Award Number EEC-0310723 as part of the Biomimetic Microelectronic Systems ERC. I also held a Whitaker Foundation Graduate Fellowship from 2003 to 2006, for which I am eternally grateful. I was also funded by a Drinkward Postdoctoral Fellowship. My other research projects in addition to those within these pages have also been funded by Bausch and Lomb.

Finally, to my family, immediate as well as extended: you have always been a great source of inspiration to me. Words can not even begin to express the love that I have for you all. I owe everything I am to you. My dear brother, Christopher Rodger, has always been my best friend and true mentor, from the days when I depended on his translations to get what I wanted, to those when I followed and emulated his every move, to now. I love you Chris. You are an amazing brother, friend, confidante, and teacher. Mum, you are so kind, intelligent, strong, and just plain incredible. I could not have gone through my education and life the way I have without your guidance, knowledge, unwavering support, and instincts to guide me. Words will not possibly encapsulate it, but I thank you, truly, for everything, and I love you more than can be expressed. To Dad: you are an amazing father and teacher, and I do and will always love you with all my heart. Thank you for instilling in me a love of learning and an innate curiosity, and for always testing the limits of my knowledge. I love you.

As is clear, there have been so many influences on my life, and I truly hope that this dissertation serves as a fitting testament to everyone who has helped me get to where I am today. I also know that there is so much further to go after my time at Caltech, look forward to the challenge, and know, with all the support of all the great people I have met and have yet to meet, that I am ready, and I am looking forward to meeting these future challenges head on.

Abstract

Development of Flexible Parylene-Based Microtechnologies for Retinal and Spinal Cord Stimulation and Recording

Thesis by

Damien Craig Rodger

Doctor of Philosophy in Bioengineering

California Institute of Technology

The problems of outer retinal degeneration and spinal cord injury affect millions of people worldwide, often resulting in devastating blindness and para- or quadriplegia that strongly impair a person's activities of daily living and impact their level of happiness. To help thwart the effects of these diseases, novel flexible parylene-based microtechnologies have been developed for functional electrical stimulation and recording in retinal and spinal cord prosthetics. Microelectrode arrays have been microfabricated according to a single-metal-layer process and a revolutionary dual-metal-layer process that promises to meet the needs of extremely high-density stimulation applications. Arrays have been fabricated of thin-film platinum, electroplated platinum, and iridium, all on parylene substrates, some electrodes surviving for more than 430 million pulses without failing. In addition, a new annealing and heat-molding process has been implemented to improve parylene to parylene adhesion and conform electrode arrays to approximate the curvature of canine retinas. A chronic implantation study of the mechanical effects of parylene-based electrode arrays on the retina over a six month follow-up period has provided excellent results. Both retinal and spinal stimulation and recording from such arrays have been demonstrated.

The first packaging technology for high lead-count prostheses capable of fully scalable interconnection of a high-density electrode array, radiofrequency telemetry coils, and other discrete components such as chip capacitors, with prefabricated, stand-alone driver circuitry is also presented, combining the best features of chip-level and wafer-level packaging technologies. This parylene-based drop-chip technology enables application-specific integrated circuits (ASICs) to be directly integrated into the fabrication process of the other system components, such that the resulting device is flexible, facilitating surgical implantation. The ASIC-to-electrode interconnects are patterned using standard photolithography and standard microfabrication techniques, enabling the density of interconnects to scale to the limits of the lithographic equipment used to define the etch holes over the on-chip pads. Electrical test results verify the efficacy of this cost-effective packaging scheme, and pave the way for a monolithic implantable parylene-based prosthesis system, which has been designed. Surgical tests of monolithic geometries for all-intraocular retinal prostheses have been conducted, and an exciting new configuration for such a device has been discovered.

Table of Contents

List of Figures

List of Tables

1 THE CLINICAL PROBLEMS OF RETINAL DISEASE AND SPINAL CORD INJURY

This work is aimed toward finding bioengineered solutions to two of the most challenging problems in medicine: blindness due to outer retinal disease, and paralysis due to spinal cord damage. This dissertation will address these clinical problems as well as their current treatments, and use this as a stepping stone to the discussion of neural prosthetics. An introduction to the field of microelectromechanical systems (MEMS) follows, a discipline with the unique potential to serve as a bridge between engineering and medicine due to the unique materials used in the fabrication of MEMS devices and the small size of resulting devices. The benefits of the use of parylene in neural prosthetics, one such unique material, will then be discussed, as well as a brief exposition on the basics of microelectrodics. Chapter 3 discusses the fabrication, *in vitro* neural stimulation, and *in vivo* mechanical testing of high-density electrode arrays for retinal stimulation. In Chapter 4, the extension of this technology toward enabling spinal cord stimulation to facilitate stepping and standing in the case of spinal cord damage or transection is discussed, with associated *in vivo* testing results. Chapter 5 focuses on a novel parylene-based integration technology that combines the benefits of chip-level and wafer-level packaging, a fabrication methodology of critical importance to the fabrication of complete systems capable of the high-density neural stimulation and recording, as well as the extension of this in the design of a monolithically fabricated stimulation system. The chapter ends with a discussion of implantation testing results of a novel system geometry for an all-intraocular retinal prosthesis. Finally, Chapter 6 concludes with some final thoughts and a discussion of the possible extension of these technologies to other applications in medicine.

As a matter of course, it is important to note that there are animal studies presented and discussed within this thesis. Although always difficult to present, and even more difficult to have to perform, I believe these studies are a necessary consequence of the need and desire for my work and the work of others to ultimately benefit humanity. To the greatest extent possible, animals were not used until we thought that our results would be the most telling, and even then, with the greatest care, respect, and judiciousness. All animal studies presented herein were approved through all appropriate and required channels at the institutions at which they were performed, and were held to the highest ethical standards possible. All eye experiments conformed to the ARVO Statement on the Use of Animals in Ophthalmic and Vision Research. We are indebted to these and other animals for our knowledge gained, and indeed, for our very existence.

1.1 Outer Retinal Disease

In normal human vision, light enters the eye (Figure 1-1) through the transparent cornea, enters the pupil (whose dilation is controlled by the iris), and is focused by the transparent crystalline lens. The light then traverses the vitreous cavity of the posterior segment, through the layers of the inner retina, where it is ultimately focused onto the photoreceptors of the outer retina. The light is there transduced into an electrical signal that is then carried through synapses and neurons (horizontal, bipolar, and amacrine) toward the inner retina (Figure 1-2). Along the way, the delicate, tissue paper like retina also performs significant visual processing tasks such as center-surround encoding and data compression. At the inner retina, the retinal ganglion cells receive the signal and send it via action potentials through their axons across the inner retina toward the optic nerve, along which the signal is then carried to the lateral geniculate nucleus (LGN) of the thalamus, and ultimately through the optic radiation (geniculo-calcarine tract) to the visual cortex.

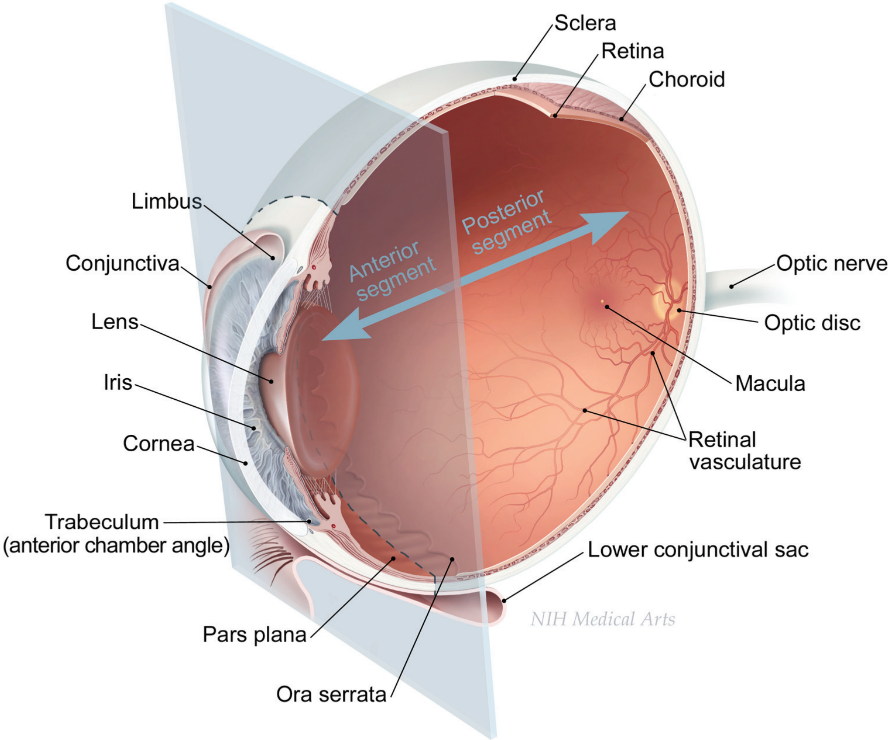

Figure 1-1. Anatomy of the human eye. Figure courtesy of NIH Medical Arts.

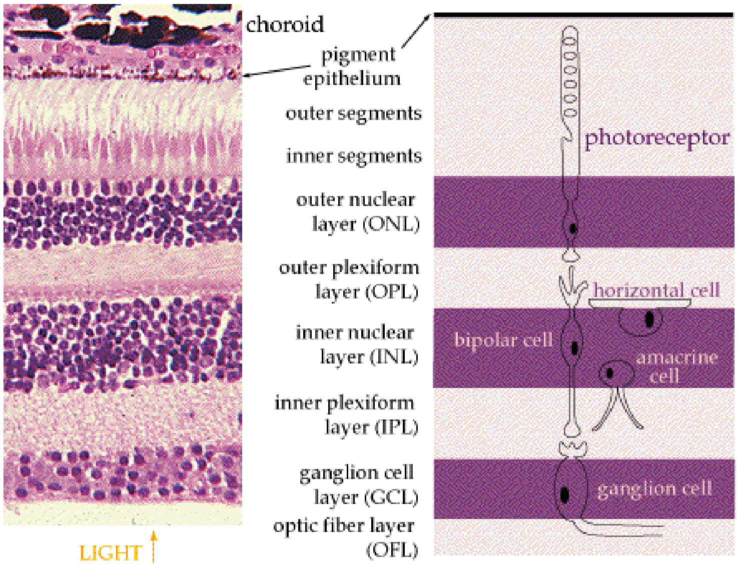

Figure 1-2. Structure of vertebrate retina. (left) Histology and (right) graphical depiction. From [1].

Due to its inherent complexity, there are many opportunities for this pathway of information to be interrupted, often resulting in blindness (the loss of light perception). According to the World Health Organization, the leading causes of blindness (defined as a visual acuity of less than 3/60, or corresponding visual field loss to less than 10 degrees, in the better eye with best possible correction) are cataracts (47.8%), glaucoma (12.3%), uveitis (10.2%), age-related macular degeneration (AMD) (8.7%), trachoma (3.6%), corneal opacity (5.1%), and diabetic retinopathy (4.8%) [2]. Indeed, some of this blindness, such as that due to cataract, results from an interruption of passage of light as it enters the eye. A cataract is an opacification of the lens, often due to long-term ultraviolet exposure, systemic disease, or simply due to age. Some blindness, on the other hand, is from disease processes that primarily affect structures at the back of the eye (e.g., glaucoma, diabetic retinopathy, AMD). In such diseases, the passage of light or action potentials through the retina is blocked, or there is a problem that affects the transduction of light into an electrical signal, or some other barrier to the transmission of the electrical signal to the visual cortex, such as optic nerve damage from glaucoma. Some blindness is easily preventable or treatable, for example by administration of antibiotic medication or antiparasitic medication in the cases of trachoma and onchocerciasis, respectively, or by removal of the block in the light passageway, for example by phacoemulsification and removal during cataract surgery. Other causes of blindness, however, are refractory to treatment.

Blindness due to such outer retinal diseases as retinitis pigmentosa (RP) and AMD affect hundreds of thousands of people worldwide. In fact, it has been estimated by The Eye Diseases Prevalence Research Group and the National Eye Institute that AMD alone will affect three million people in the United States by the year 2020 [3]. In addition, the prevalence of RP has been estimated to be approximately 1 in 4000 [4]. Although the pathogeneses of these retinal photoreceptor diseases are, to date, not entirely understood, it is known that they are largely restricted to the outer retina, and that downstream circuitry, although it undergoes significant remodeling, is relatively spared [5-7]. There exist several possible approaches to thwarting the devastating effects of these diseases. Of these, the surgical, pharmacological, stem cell, and dietary approaches are promising. Laser ablation of leaky blood vessels and diets rich in antioxidants, for example, have been shown to slow the progress of AMD, but not to have any effect on its incidence. Effective pharmacologic agents, likewise, have long been elusive. Recent evidence has shown that stem cell therapy could also be a possibility for the treatment of such diseases, by possibly replacing the lost photoreceptors with stem cells capable of maturing into photoreceptors that then make connections with the rest of the retina [8].

However, such treatments, in reality, are still very far away from being used in clinical practice, and have a number of ethical and political barriers to their implementation.

In need of another possible treatment for these profound retinal diseases, in 1994 Humayun et al. reported the results of a pioneering study to electrically stimulate vertebrate retinas [9], a bioengineering approach that would possibly bypass the diseased photoreceptors in the visual pathway. In this study, bullfrog eyecups, as well as rabbit eyes (the rabbits were injected intravenously with sodium iodate, a chemical toxic to the retinal pigment epithelium and with other effects on photoreceptors), were stimulated with platinum electrodes. In their report, the following conclusion was made: “Surface electrical stimulation of the inner retina in normal eyes and in eyes with outer retinal degeneration can elicit a localized retinal response.” This has since had a profound impact on the field of ophthalmology, by dramatically throwing an engineering solution into the mix of possible treatments for patients with devastating blindness due to outer retinal disease.

As a follow-up to this study, it was shown in 1996 by Humayun et al. that this seemingly simple approach of passing a carefully controlled electrical current through an electrode placed directly on the retinal surface to activate the still functional electrically excitable cells of the retina can also elicit visual percepts in humans with otherwise bare or no light-perception vision [10]. Perhaps even more important than the perception itself was the nature of the perception. Subjects did not report seeing streaks or multiple percepts of light simultaneously when stimulating from one electrode, as might be expected if the axons of the ganglion cells, as they made their way to the optic nerve in the nerve fiber layer, were being stimulated. Instead, they reported seeing discrete, highly localized percepts that seemed to correlate very well with the location of stimulation. This suggested that it was not the axons that were the most electrically excitable, but instead the cell bodies of the several retinal ganglion cells (RGCs) or the bipolar, or even possibly amacrine or horizontal cells underlying the electrode. Indeed, it has since been conjectured that it could even be the characteristic right-angle bend in the axon of the RGCs that has maximal electrical excitability [11]. No matter the case, this was the confirmation of the feasibility of an engineering approach to treat human blindness with a "retinal prosthesis."

There are now a large variety of approaches to artificial vision, each with their own advantages and disadvantages. There is this epiretinal approach (Figure 1-3), in which an electrode array is placed directly on the retina from its anterior aspect. There is the subretinal approach, in which an electrode or photodiode array is placed within the layers of the retina [12], as is also shown in Figure 1-3 (this can be further subdivided to the *ab interno* and *ab externo* approaches, in which an incision is made within the retina or within the sclera, choriocapillaris, or RPE to insert the device, respectively). There is also the optic nerve approach, in which electrodes are placed around the optic nerve in an attempt to coarsely stimulate the afferent ganglion cell axons [13]. Finally, there are also the cortical approaches, whether they be to the visual cortex [14] or to the lateral geniculate nucleus (LGN) of the thalamus [15, 16], the first stop for information from the retina as it enters the cortex. Some mention should also be made of the microfluidic approaches to retinal stimulation, where targeted neurotransmitter delivery to the neurons downstream from the nonfunctional photoreceptors is the end goal [17]. Such a

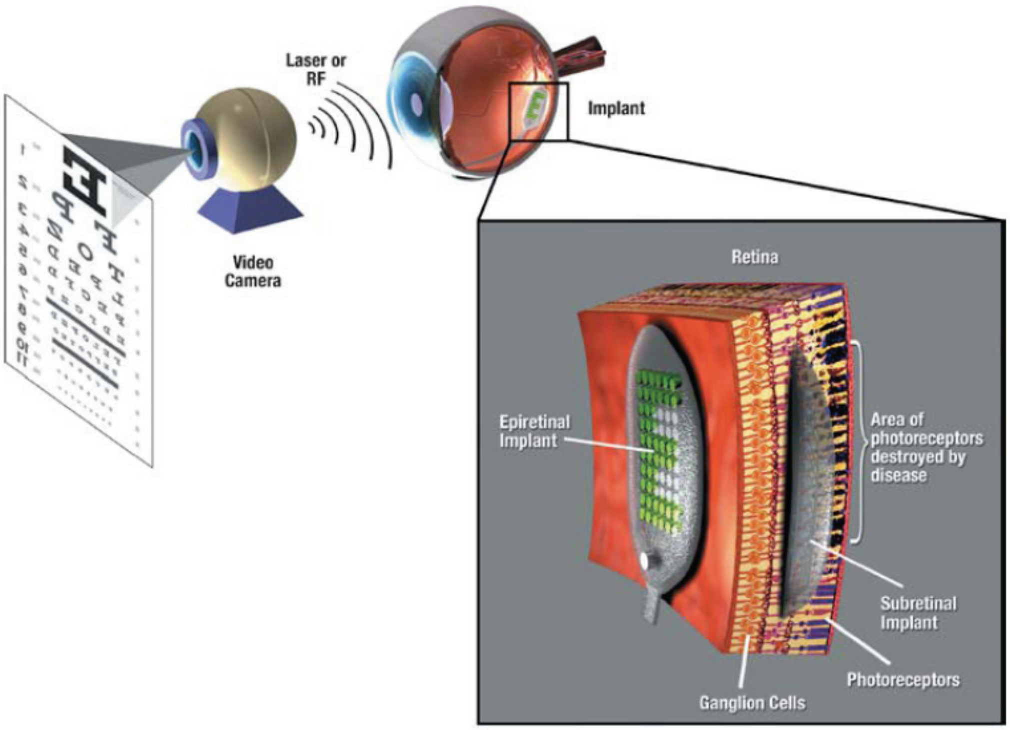

Figure 1-3. System overview and relative locations of epiretinal and subretinal implants [18].

microfluidic approach benefits from avoiding the use of a potentially harmful electrical damage the delicate retinal tissue, and it presents the possibility of enabling selective activation at target synapses through controlled release of different neurotransmitters. There are several drawbacks to such neurotransmitter-based prosthetics, however. Perhaps the most obvious drawback is the difficulty of renewing the neurotransmitter supply in a fully implanted system. Furthermore, the glutamate proposed as a likely neurotransmitter in these prostheses is both acutely and chronically neurotoxic [19], requiring a very tightly controlled delivery system. A complete discussion of the advantages and disadvantages of each of the different approaches is beyond the scope of this text, but can be found in several good review articles on visual and retinal prostheses [15, 18, 20], many of the main points of which are summarized in Table 1-1.

We believe that the most promising of these technologies, when examined in light of these advantages and disadvantages, is the epiretinal approach. This is due to the existence of well-documented techniques for gaining epiretinal access, the relatively little trauma associated with the epiretinal surgery when compared with the blebbing necessary to insert a subretinal array and the associated disruption of remaining functional interconnections within the retina, and the ability to assess device placement and functionality visually using standard ophthalmologic examination equipment (e.g., ophthalmoscope, optical coherence tomography (OCT)), when compared with the optic nerve and cortical approaches. What is perhaps most important is that, because such degenerative diseases occur over time, the visual cortex of these patients understands the retinotopic spatial map of the outside world, a map which is largely preserved throughout the progression of these diseases. As such, access to this map, which we believe to be crucially important to create functional vision, is preserved in retinal versus optic nerve and cortical approaches (with the likely exception of approaches to the LGN and to V1 [21]). It is thus important to recognize that such electrical stimulation approaches largely rely on a relatively intact electrical pathway from the retina to the brain. In many congenital diseases or in cases of trauma affecting the optic nerve, this pathway does not exist, and such an approach is thus unlikely to have any major benefit.

The state of the art for an epiretinal prosthesis has been the successful demonstration of a prototype 16-electrode device, fabricated by Second Sight Medical Products, Inc. (Sylmar, CA, USA) in six patients [22]. While clearly not enabling such activities of daily living as newspaper reading and facial recognition, previously completely blind subjects can, for instance, differentiate between a plate, a cup, and a knife, in a high-contrast environment free from background distracters, an undeniably incredible feat of engineering and medicine. Furthermore, subjects have been shown to be able to discriminate direction of movement of parallel white bars on a black background, and can locate white squares within a quadrant of otherwise black space [23]. This implant has demonstrated the technology as well as the remarkable ability for the human brain to compensate for low-resolution input. Although this had previously been demonstrated by cochlear prostheses for patients with severe hearing impediments [24], it was unclear whether this plasticity would translate well to visual prostheses. In fact, patients have demonstrated their ability to discriminate large letters simply by *instinctively* scanning the camera mounted on their head back and forth over the image displayed in front of them, a sort of innate edge-detection mechanism, dramatically increasing the capability of the 16-electrode device on their retina. Few scientists disagree, however, that increasing the number of electrodes on the implanted array will dramatically add to the capabilities of the prosthesis as a whole in enabling the patient to better carry out activities of daily living. The prototype device is hand assembled, a fact that limits the resolution possibilities of the device. Indeed, were it still necessary to interconnect integrated circuits by hand, computers would be far less useful to us as they are today. The need exists, then, to bring microelectronics and microfabrication technology to bear on the problem of retinal prosthetic devices. The race is on to build high-density multielectrode arrays in such a way and with such materials that the method is scalable to the needs of long term, high-density retinal stimulation.

Table 1-1. Advantages and disadvantages of different artificial vision approaches

Approach	✓ Advantages	× Disadvantages
Epiretinal	• Well-established surgical techniques • Long-term efficacy shown in patients • Post-operative device observation possible • Objective studies easy • Spatial map preserved • Retinal, thalamic, and cortical processing maintained • High-density electrode array possible • Privileged immune environment • Complete intraocular system possible	• Likely not useful for non-retinal degenerative blindness • Heat dissipation concerns • Mechanical instability?
Subretinal	• Device more secure? • Heat dissipation from choroid • High-density electrode array possible • Retinal, thalamic, and cortical processing maintained • Objective studies are possible	• Likely not useful for non-retinal degenerative blindness • Long-term efficacy not shown to date • Objective studies difficult with always-on photodiode implants • Disruption of remaining retinal connections during implantation • Nutritional deprivation of RGCs • Complete intraocular system not possible in most cases(potential route for infection)
Optic nerve	• Potentially useful for non-retinal degenerative blindness	• Complicated surgery • Spatial map not preserved • High-density stimulation difficult • Complete intraocular system not possible
Visual cortex	• Potentially useful for non-retinal degenerative blindness • High-density electrode array possible	• Complicated surgery • Social phobia about brain implantation • Spatial map preservation questionable • Surgical and post-implantation complications • Retinal, thalamic, and some cortical processing not maintained

1.2 Spinal Cord Injury

Spinal cord injury (SCI) can occur through a variety of mechanisms. The primary reasons for this myelopathy fall into two major categories: trauma (e.g., automobile/motorcycle accident, sports injury such as from diving or horse riding, violence, fall), or disease (e.g., spina bifida or tumor). Spinal cord injuries can affect motor function, sensation, and autonomic functions (e.g., bladder control, breathing). Approximately 50% of SCIs in the United States are classified as complete [25]. This means that the spinal cord has lost the ability to transmit information across a segment within it, cutting off all functional communication from the brain to the nerves below the injury site and resulting in no sensation or voluntary control of motor function below the injury site due to lost input from the brain. This usually results in para- or quadriplegia, depending on the site of injury. The full American Spinal Cord Injury (ASIA) classification system for such injuries is given in Table 1-2, with muscle functionality defined according to Table 1-3. Although in most cases the cord is not completely transected or even cut, it is significantly damaged by interruption of blood flow supplying one of its segments or through spinal contusion. Even though the vertebral column protects the cord, when trauma is sufficient to compromise this protective cage, the broken vertebrae can impinge on the cord and crush or destroy the axons within it very quickly, with continued loss of axons over time [26]. Some estimates pin the prevalence of spinal cord injury in the United States at approximately 250,000 [27], with an incidence of approximately 10,000 to 12,000 per year [28], while others state the prevalence is significantly higher, at around 450,000 [25]. Approximately 55% of spinal cord injuries occur in young victims between 16 and 30 years of age, making it a disease to bear usually for the rest of their lifetime, and more than 80% of victims are males [28]. In some cases of incomplete injury, function can be recovered over time [29]. However, in most cases, some level of impairment is permanent. It is interesting to note that even if a patient has a degree of impairment, such as spasticity or pain, they could still be classified as ASIA E (normal).

Table 1-2. ASIA Impairment Scale, with muscle strength graded according to Table 1-3 and sacral motor and sensory function assessed via rectal examination for motor function or sensation at the anal mucocutaneous junction

ASIA Category	Impairment Level
A	Complete: No sensory or motor function is preserved in sacral segments S4-S5.
B	Incomplete: Sensory, but not motor, function is preserved below the neurologic level and extends through sacral segments S4-S5.
C	Incomplete: Motor function is preserved below the neurologic level, and most key muscles below the neurologic level have muscle grade less than 3.
D	Incomplete: Motor function is preserved below the neurologic level, and most key muscles below the neurologic level have muscle grade greater than or equal to 3.
E	Normal: Sensory and motor functions are normal.

Table 1-3. Medical Research Council (MRC) scale of 0-5 for muscle function

Muscle Strength	Definition
5	Normal power.
4+	Submaximal movement against resistance.
4	Moderate movement against resistance.
4-	Slight movement against resistance.
3	Movement against gravity but not against resistance.
2	Movement with gravity eliminated.
1	Flicker of movement.
0	No movement.

The complexity of the spinal cord is undeniable. In fact, despite the popular misconception that the spinal cord serves only as a communication conduit between the brain to the muscles and organs and from the skin back to the brain, it is much more accurate to view the spinal cord as an outcropping of the brain. While the spinal cord below a complete injury does indeed lose input from the motor cortex, and its ability to send sensations of touch to the brain is completely compromised, the spinal cord is not rendered useless. Even an intact cord does a lot of the primary processing and reflex control without any input to or from the brain.

The spinal cord (medulla spinalis) is an organized, jellylike bundle of nervous tissue, with supporting blood vessels and outer protective layers called meninges. A section of the spinal cord (Figure 1-4) reveals a characteristic inner H-shaped region, called the grey matter, which contains the soma of neurons, supportive cells known as glial cells, as well as small unmyelinated interneurons responsible (usually) for lateral connections. The outside white matter, which is organized into functional tracts, contains axons of neurons which ascend to and descend from the brain, as well as axons

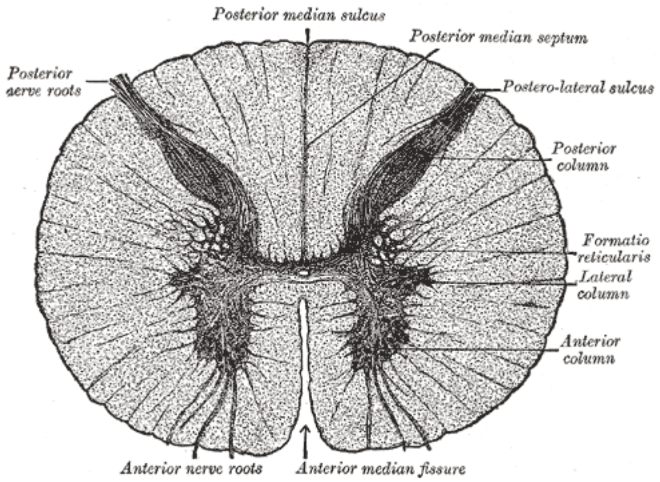

Figure 1-4. Cross-section of the spinal cord [30].

traversing laterally through their respective roots to the musculature of the limbs and incoming from the sensory neurons (whose cell bodies, intriguingly, are located in dorsal root ganglia outside of the spinal cord proper). The characteristic white color derives from the fatty myelin coating of the axons, which increases action potential signal transmission speed through the axons. Grossly, the spinal cord is housed in the protective vertebral canal at the dorsal aspect of the vertebral column, Figure 1-5 (adapted from [30]), and is located posteriorly in the human body. The spinal cord has discrete levels at which the dorsal and ventral roots exit and enter, called spinal levels. Embryologically, the spinal levels are adjacent to corresponding vertebrae, between which the axons contained in the dorsal and ventral roots, after joining to form spinal nerves, exit through intervertebral foramina. During growth, however, the vertebral column extends relative to the spinal cord. As such, the vertebral levels and the spinal levels begin to separate. In human adults, the conus medullaris,

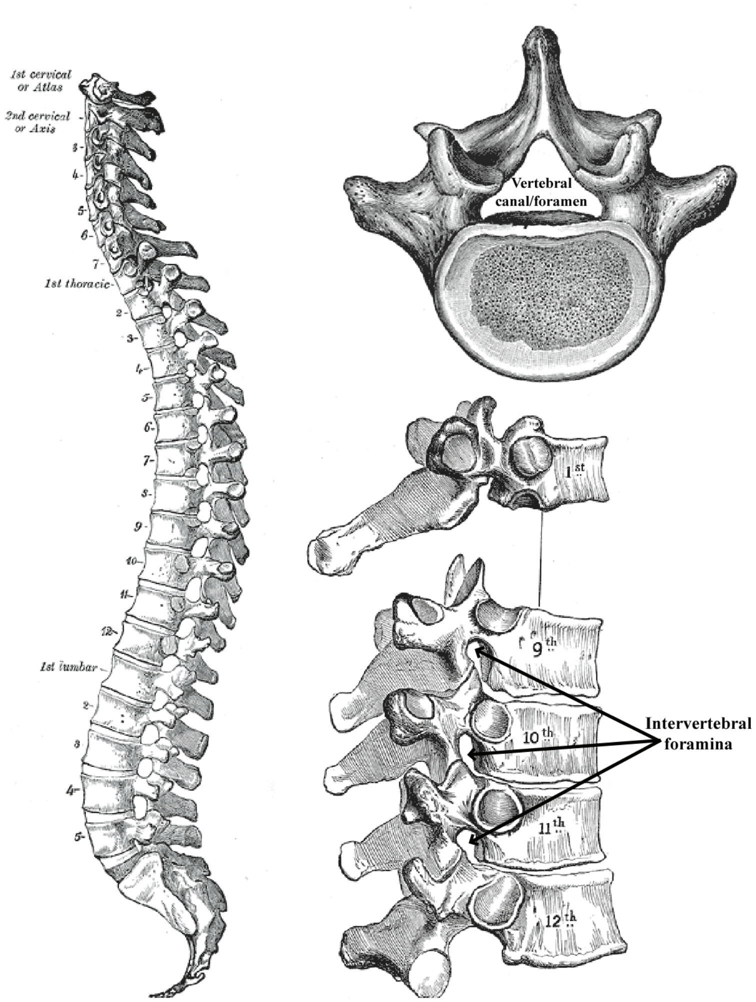

Figure 1-5. (left) Vertebral canal. (right top) Typical lumbar vertebra. (right bottom) Intervertebral foramina providing passage for spinal nerves.

corresponding to the end of the spinal cord, terminates at lumbar vertebrae L1 or L2. The lumbar and sacral roots continue as the cauda equina. In different mammalian species, this relative correspondence changes however, a similar discrepancy between spinal and vertebral levels exists.

In patients with spinal cord injury, there are several approaches to rehabilitation. The foot-drop stimulator, wherein stimulation of the peroneal nerve affects localized contraction of ankle dorsiflexors to counteract the problem of foot drag, has been widely studied [31] with mixed results [32-34]. Other functional movements requiring much more coordinated musculature responses are far more difficult with implantable peripheral nerve or muscle stimulators because of the need to control timing as well as pulse amplitudes of likely a large number of electrodes in rapid succession. Skin surface electrodes such as those in the ParaStep system [35, 36] suffer from these problems as well as the problem that many muscle groups are difficult to target from this more remote location. In addition, because in complete SCIs the voluntary input from the motor cortex to initiate such movements is lost, an accessory mechanism for determining the desired motion is warranted. This may require recording electrode arrays in the motor cortex as another component of this system, as well as possible electrical stimulatory feedback (in addition to the visual feedback already present). Any such system, then, is likely to be quite complex and difficult to implement in practice.

The need exists, then, for another approach to elicit such coordinated activity. It has been shown that stepping [37] and full weight-bearing standing [38] can be improved even in complete spinal felines through treadmill training, and de Leon et al. have shown that this locomotion improvement is retained for a period of months [39]. Recently it has been demonstrated that the same applies to SCI in humans [40]. This is not altogether surprising, given that the spinal cord has been shown to have a great deal of plasticity in infants as well as adults [41, 42]. Much recent attention has been focused on the concept of motor primitives [43-46] as at least a partial basis for this ability to stand and locomote in such cases. In theory, proprioceptive feedback from the limbs (which is still intact), such as a treadmill pulling the limbs and feet backwards, can generate a reflex arc, in most cases mediated by interneurons in the grey matter of the spinal cord [47], that, despite lack of cortical control, can activate coordinated bilateral and rhythmic motion in the limbs by the resultant activation of motor primitives (groups of associated neurons in the cord) and motor output from the ventral horns. This feedback activation and resultant rhythmic output has been show to improve with such training as well as with pharmacology [48]. Some have explored intraspinal stimulation as a mechanism for activating such “movement synergy” circuits, with evidence showing that as few as four microelectrodes implanted intraspinally, two on each side of the cord [49], can generate locomotor-like stepping despite an initial supposition that far more would be required [50]. However, these studies have been largely hindered by problems of short durability. Usually, within three or four weeks of implantation, signal-to-noise ratios in such penetrating microwire arrays when used for recording fall to limits where they are no longer useful. “Countermeasures” are taken to prevent such problems, such as using dabs of glue, microsuturing, and cling-film [34] to hold arrays in place. Up to seven weeks of data were taken by Utah multielectrode arrays [34], but electrodes tended to record from different units over time and there was fallout, indicating possible movement of the array as well as such problems as tissue encapsulation and gliosis. However, it has been shown that epidural or subdural (meningial layers are diagrammed in Figure 1-6 [30]) stimulation of the spinal cord can also provide useful benefits in both felines [51] as well as humans [52] with complete lesions, especially when used in combination with pharmacological intervention and/or locomotor training [53]. This approach potentially avoids the many problems associated with penetrating electrode arrays such as encapsulation as well as tissue damage that may abolish useful connections upon implantation. In such a paradigm, it is likely possible to modulate the neurosensory or descending voluntary input to the spinal cord by tonic, subthreshold stimulation, as has also been shown in incomplete injuries with intraspinal electrodes [54]. Arguments to the contrary are that spatial resolution may be limited in such an approach [49, 55] and that it is difficult to replicate placement of electrodes from trial to trial. However, this typically assumes the use of more traditional fine-wire microelectrodes rather than a flexible, conformal multielectrode

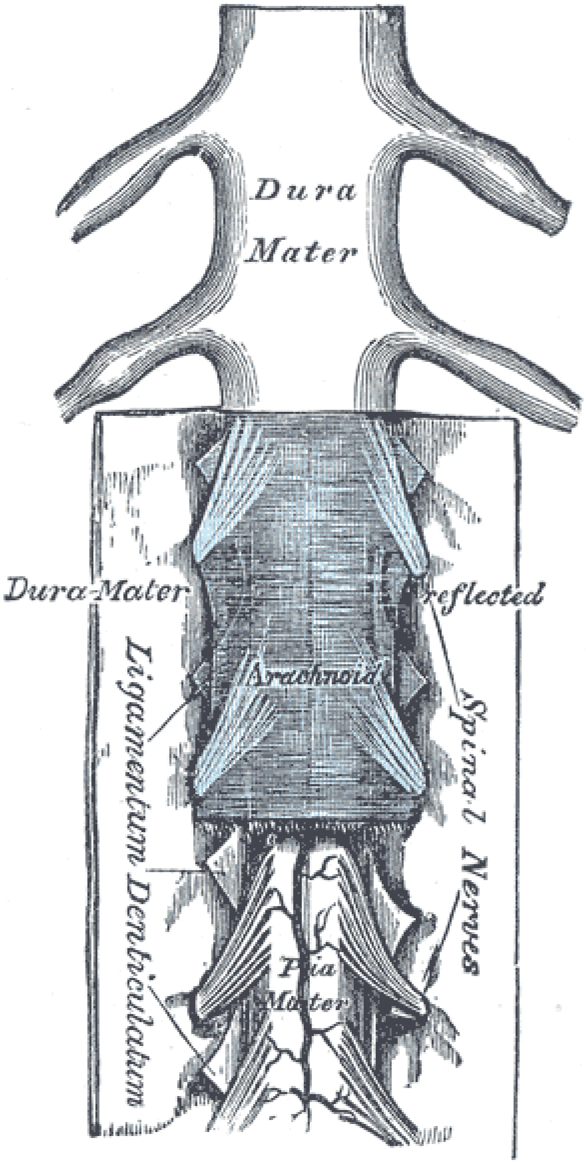

Figure 1-6. Meninges of the spinal cord.

array with extremely precise placement and relationship of the electrodes on the array to one another and ultimately to the spinal cord due to the microfabrication technology utilized in their production. Such an array technology is the focus of this dissertation. We propose a system, which eventually will be completely implantable, that is capable of stimulating the dorsum of the spinal cord in such a manner that modulation of the sensory input to the cord, interneruonal activity within, and even motor output from the cord, is possible. Tonic, subthreshold stimulation, applied at precise times and precise locations along the spinal cord, would likely help sustain or stop locomotor activity with the kind of coordination and rhythmicity already discussed. Perhaps in combination with both locomotor and standing training as well as appropriate pharmacological administration (e.g., quipazine), it is possible that such an array would give those with both complete and incomplete spinal injury the ability to stand and walk once again. In order to provide appropriate proprioceptive input in the case of complete SCI, it would likely be possible to provide an accessory device or muscle stimulator to initiate this type of activity. However, this approach leverages the innate activity and processing power present in the spinal cord to its greatest extent and likely obviates the need for a stimulation control system of great complexity in order to bring about coordinated muscle activity, as is necessary for a peripheral muscle or motor neuron control system. Such electrical stimulation may also, as has been hypothesized in the case of subthreshold retinal stimulation systems as well, have the capability of promoting axon regrowth [56, 57] and facilitating plastic changes in the cord. Such an array would likely need to be conformable to the cord, and would need to be implanted in relatively close apposition to it, either epidurally (from which location the electrical field would need to penetrate several meningeal layers) or subdurally, such that it is closer to the surface of the cord. In the ideal case, the array would be flexible enough to move with the cord during motion and bending such that functional targets are the same in any position. In addition, it should be the case that such an array can also record from the cord so as to recognize returning action potentials from the dorsal root and modulate this input accordingly. This approach, then, requires a high-density array with many electrode sites from which to choose during training and daily activity, as well as the ability to both record from and stimulate the cord, something which current arrays, such as those for pain management, simply can not do because they are too bulky, inflexible, and of too low a density (up to 16 electrodes).

1.3 Conclusions

The problems of outer retinal degeneration and spinal cord injury have been discussed, with a focus on the target populations for electrical intervention. It is clear that technologies prototyping such electrical stimulation and recording strategies are still in their infancy, largely because of questions surrounding material choice and the lack of fabrication know-how. This dissertation centers on parylene-based technologies as a promising approach to fabrication of multielectrode arrays and systems capable of such stimulation. Before delving into the crux of the fabrication discussion, it is important to discuss microelectromechanical systems technology, with a focus on parylene, as well as the guiding principles behind microelectrodes, topics that the next chapter is devoted to.

2 MICROELECTROMECHANICAL SYSTEMS, PARYLENE, AND MICROELECTRODES

2.1 Introduction to Microelectromechanical Systems

The field of microelectromechanical systems, or MEMS, had its real beginnings at the same time that the first point-contact transistor was demonstrated, in December of 1947, by the harbingers of the information age, William Shockley, John Bardeen and Walter Brattain. Kilby’s demonstration of an integrated circuit (IC) for Texas Instruments’ head brass on September 12, 1958 was the birth of semiconductor ICs. Their combined efforts began a race that continues today, to make transistors smaller, faster, better, and cheaper than those before them.

At the same time that this investigation of such circuits began, people started asking why other technologies were not being miniaturized as well. Indeed, Richard Feynman, in his seminal talk on December 29, 1959, stated “There’s plenty of room at the bottom.” His charge to the audience was to think about how to scale down cars, motors, and encyclopedias to sizes never previously conceived of. MEMS, as a field, was born.

MEMS technology has been lucky to benefit from the significant and dramatic advances in the semiconductor industry, in which chip complexity is growing according to Moore's law [58]. In many cases, processing equipment and techniques for MEMS are largely borrowed and adapted from the IC world. But the fields are in fact quite disparate. As the name implies, MEMS is devoted the fabrication of small systems capable of mechanically and electrically interacting with the analog, physical world, as opposed to the digital world mastered by the traditional semiconductor industry. Incredible ingenuity has gone into making such devices as the micromotor [59] and the accelerometer [60], as well into developing new processing technologies, such as deep reactive-ion etching [61], and materials unique to this field. Perhaps most importantly, because of the analog nature of these systems and their extremely small size, MEMS are capable of interfacing at the cellular level both *in vitro* [62] and in the human body, in the specialized field known as bioMEMS.

On a very basic level, MEMS devices are fabricated, usually many simultaneously, according to two major paradigms [63, 64], as shown in Figure 2-1. The first is bulk micromachining, in which materials are removed from a substrate, such as a silicon wafer, to define structures of interest (top-down processing). Classic examples of such devices are those fabricated according to the single-crystal reactive etching and metallization (SCREAM) process (Figure 2-2), a single-mask fabrication process capable of fabrication of devices from accelerometers [60] to transmission lines and phase shifters [65] (Figure 2-3) in bulk silicon. General bulk micromachining techniques include isotropic wet etching of silicon dioxide with hydrofluoric acid, anisotropic deep reactive-

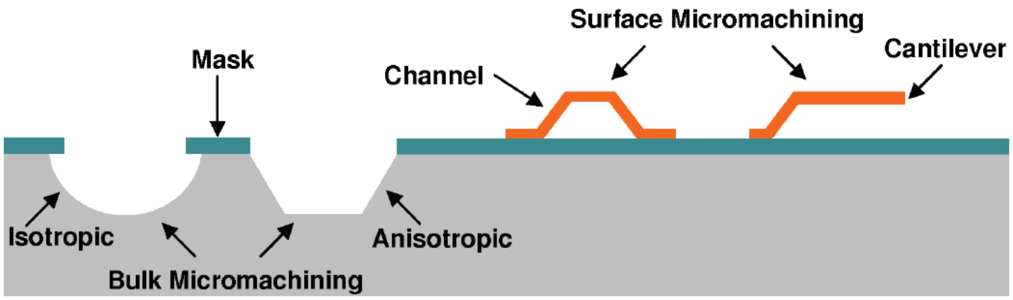

Figure 2-1. Typical cross-sectional views of bulk-micromachined and surface-micromachined devices.

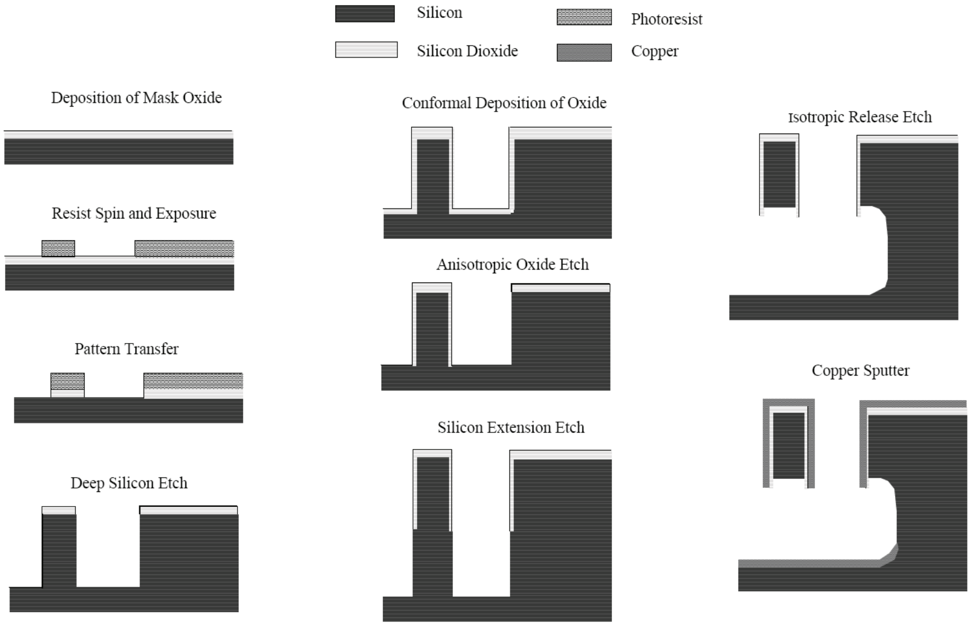

Figure 2-2. Single-mask SCREAM process for bulk micromachining.

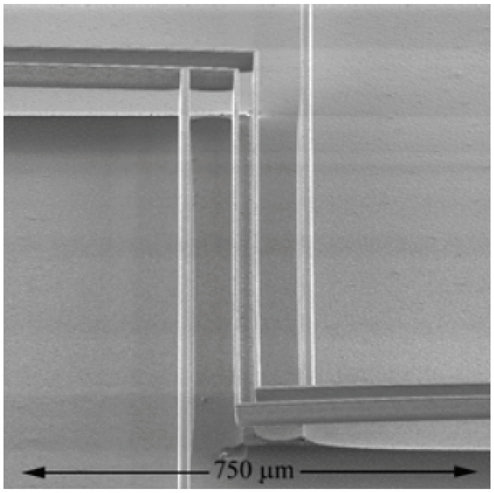

Figure 2-3. Microfabricated SCREAM millimeter wave phase shifter [65].

ion etching of silicon, and associated masking processes with wet oxidation or photoresist.

Surface micromachining, in general, is where materials are added to the top surface of the substrate (bottom-up processing). Such processes include sacrificial layers to help define the shape of structures, and the substrate mainly serves as a carrier only, and hence can usually be of any material (silicon wafers usually used, however, due to compatibility with alignment and processing equipment, cleanliness, and cost considerations). Surface-micromachining processes lend themselves to the fabrication of microfluidic devices, such as that shown in Figure 2-4 [66]. Materials commonly used in surface micromachining include plasma-enhanced chemical vapor deposition (PECVD) oxide or nitride, polysilicon, and polymers. Polymers typically used in such devices include polyimide, silicone, and parylene. While seemingly the two paradigms are dichotomous, in many cases, a combination of bulk and surface micromachining is used.

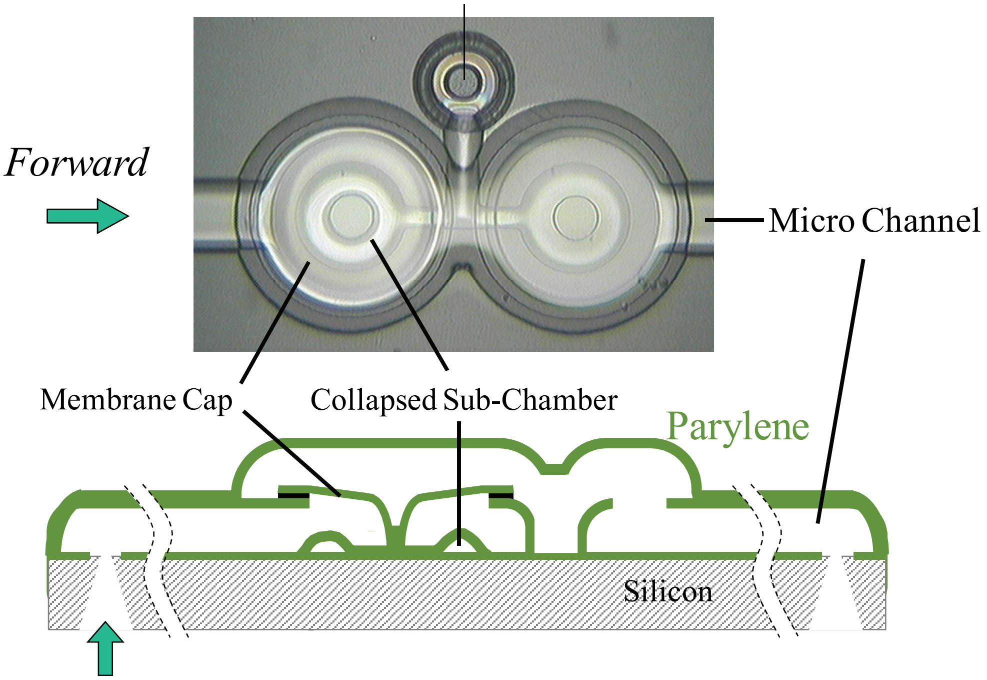

Figure 2-4. In-line micro checkvalve fabricated by surface micromachining.

The most crucial step in both of these paradigms to achieve resolutions high enough for device miniaturization is photolithography. The devices are patterned using photodefinable compounds, known as photoresists, and an ultraviolet light source with high-precision optics, as shown in Figure 2-5, allowing for high throughput. Indeed, such devices are typically fabricated in a cleanroom to ensure dust does not affect the photolithography process, first and foremost. By combining steps of material deposition, photolithography, material etching/removal, and any necessary cleaning steps, two-dimensional masks can be used to extrude and fabricate complex devices in three dimensions.

Most of the devices presented in this dissertation are fabricated according to the surface-micromachining paradigm, in that the silicon wafer is used mainly to hold the devices and move devices from one machine to another. However, our devices are typically completely removed from this substrate, and none of the silicon is used as part of the final device. Silicon, although an excellent material from a mechanical and electrical point of view, is generally not accepted as a biocompatible material (this,

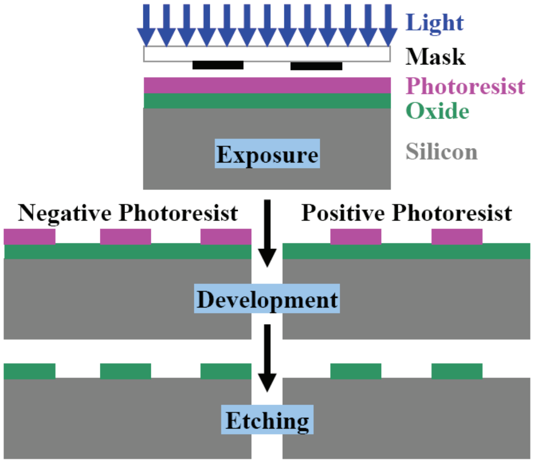

Figure 2-5. Steps involved in photolithography. Figure courtesy of Dr. Angela Tooker.

however, is a constant subject of debate and contention in the bioMEMS community), and is not flexible enough for our arrays. Any silicon components, such as microchips, would likely be covered with parylene prior to incorporation in our biodevices.

2.2 Introduction to Parylene

Parylene is the trade name for a family of semicrystalline thermoplastic polymers known as the poly(para-xylylenes) (PPX). These were discovered in 1947 by Michael Szwarc in Manchester, England [67]. It was originally deposited in an investigation of aliphatic carbon-hydrogen bonds where the carbon was attached directly to a benzene ring, by heating toluenes and ortho-, meta- and para-xylenes to very high temperatures and looking for degradation products [68]. The very first parylene film deposited, then, was parylene N (with no substitutions on the benzene ring), and was temporarily known as a Szwarcite snakeskin. This deposition process, however, had the disadvantage that gaseous by-products were an inherent part of the method. William Gorham, an employee at Union Carbide, soon thereafter devised an alternate method of parylene deposition that involved the pyrolysis of a dimerized form of the material, di-para-xylylene, or [2.2] paracyclophane. It was largely unknown at the time how to make this dimer in large amounts as it had only been isolated as an impurity in Szwarc's method. However, in 1951 Donald Cram reported a method for making this material in bulk. On February 17, 1965, Union Carbide announced the availability of parylene films and the new vacuum deposition method, known as the Gorham process. There were over 20 types of parylene actually developed, but only three were considered commercially viable: these were

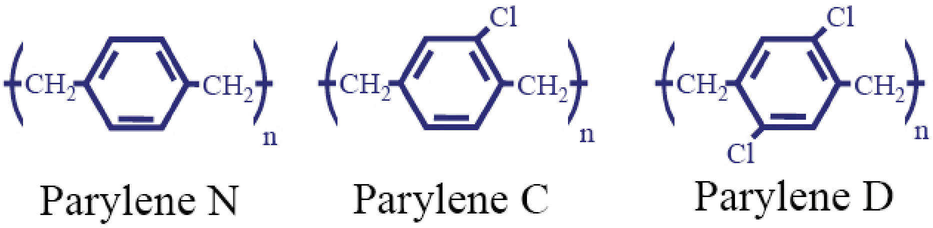

Figure 2-6. The three originally commercialized parylene variants.

parylene N (no chlorines on the benzene ring), parylene C (one chlorine on the benzene ring), and parylene D (with two chlorines on the benzene ring) (Figure 2-6). However, a new fluorinated version of parylene, parylene HT, has recently become commercially available, and can be deposited in a new system available in our cleanroom.

In the Gorham vapor-deposition process [69] (diagrammed in Figure 2-7), which takes place at vacuum (~25-35 mT, to increase mean free path to the substrate), a charge of parylene dimer is placed in a vaporizer furnace. The dimer evaporates at approximately 130 to 150 °C, and then passes through a very high temperature pyrolysis (~650 to 750 °C) furnace, where the molecule is split into monomers. The

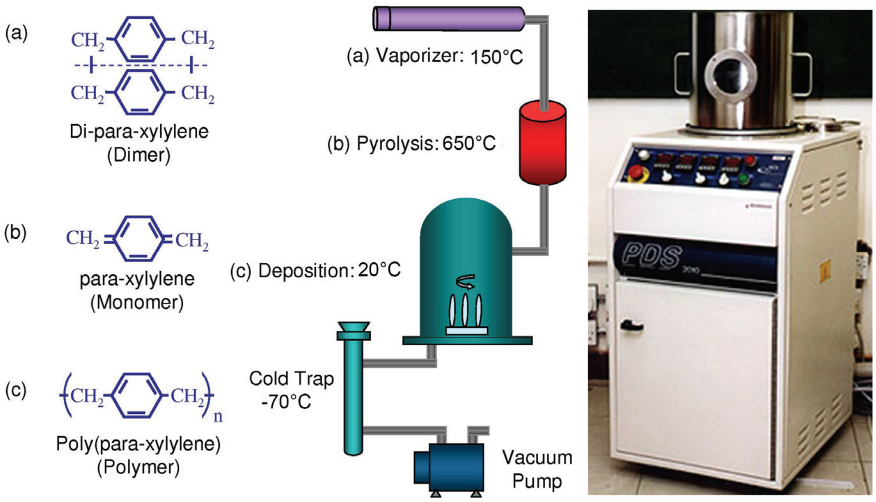

Figure 2-7. (center) Gorham process for parylene deposition. (left) Chemical structures at corresponding points. (right) PDS 2010 Labcoater System.

monomers enter a chamber that is held at room temperature, and polymerize on all exposed surfaces in the chamber conformally and without pinholes. Residual monomer is collected on a cold trap. Different variants of parylene require varying process conditions, but the method remains essentially the same. The existing variants of parylene have varying properties as well as uses. These are summarized in Table 2-1 (where these are compared with poly(dimethylsiloxane) (PDMS), a commonly used spin-on silicone with similar applications as parylene) and Table 2-2. To summarize, parylene N is primarily used as a dielectric and when lubricity and crevice penetration is important. Parylene C is an ISO 10993, United States Pharmacopeia (USP) Class VI material (the highest biocompatibility rating for plastics in the United States) and has excellent water barrier properties. In addition, it has a very large elongation to break. Parylene D has now been largely replaced by parylene HT [70], but is used when mechanical strength is of primary concern. Parylene HT has extremely low coefficients of static and kinetic friction, excellent thermal stability and good water barrier properties, high ultraviolet stability, and is also ISO 10993 biocompatible [70-72]. The possible uses of the main parylene variants for biological applications are summarized in Table 2-3. Finally, very recently, Kishimoto Sangyo Co., Ltd. in Japan has devised additional parylenes in which amino groups have been added to the benzene rings (Figure 2-8). The amino group may add even more improved biostability, but could also generate bioactivity that may or may not be beneficial to device functionality. We have preliminarily tested these amino parylenes have found them to be compatible with standard parylene processing technology, such as oxygen plasma reactive-ion etching (RIE), in our cleanroom, but they will not be explored further in this thesis.

Table 2-1. Properties of parylene N, C, D, HT and PDMS [73, 74] (courtesy of Dr. Siyang Zheng)

Property	Parylene N	Parylene C	Parylene D	Parylene HT	PDMS [74]
Dielectric Strength (V/mil), 1 mil film	7,000	5,600	5,500	5,400	610 [75] (1 mm film)
Dielectric Constant					
60 Hz	2.65	3.15	2.84	2.21	2.3-2.8
1 kHz	2.65	3.10	2.82	2.20	
1 MHz	2.65	2.95	2.80	2.17	
Young's Modulus (psi)	350,000	400,000	380,000	--	52 – 126
Index of Refraction	1.661	1.639	1.669	--	1.4
Yield Strength (psi)	6,100	8,000	9,000	--	325
Elongation to Break (%)	20-250	200	10	--	210 – 310 [75]
Coefficient of Friction					
Static	0.25	0.29	0.33	0.145	--
Dynamic	0.25	0.29	0.31	0.130	0.43-0.51 [76]
Density (g/cm^3)	1.10-1.12	1.289	1.418	--	$9.7*10^{-4}$
Melting Point (°C)	420	290	380	>450	-49.9 – 40
Thermal Conductivity at 25 °C (10^{-4} cal/(cm*s*°C))	3.0	2.0	--	--	3.6
Water Absorption (% after 24 hours)	< 0.1	< 0.06	< 0.1	< 0.01	-- (depends on cure conditions)
Specific Heat at 20 °C (cal/g*°C)	0.20	0.17	--	--	0.35

The advantages of using parylene, and, more specifically, parylene C, as the structural material for neuroprostheses, when compared with technologies based on the use of other materials such as PDMS, polyimide [77] and silicon [78], include parylene's pinhole-free conformality due to its unique room-temperature chemical vapor deposition process, its low water permeability, its chronic implantability and its high flexibility and

Table 2-2. Relative properties of different parylene variants (adapted from [70])

Property	Parylene N	Parylene C	Parylene HT
Crevice Penetration	Better	Good	Best
Hardness	Better	Good	Best
Coefficients of Friction	Better	Good	Best
Elongation to Break	Middle	Best	Least
Moisture Resistance	Better	Best	Good
Dielectric Strength	Best	Better	Good
Dielectric Constant	Lower	Low	Lowest
Dissipation Factor	Lower	Low	Lowest
Thermal Stability	Moderate	Moderate	Excellent
Gas Permeability	Better	Best	Good
Chemical Resistance	Excellent	Excellent	Excellent
Thickness Control	Excellent	Excellent	Excellent
Coating Speed	Medium	High	Low

mechanical strength (Young's modulus ~4 GPa). The Young's moduli of two other commonly used materials for neuroprostheses, PDMS and polyimide 2611, are graphed alongside that of parylene C in Figure 2-9. PDMS arrays have been handled by surgeons in our vivarium, and these are often as reported as too floppy and difficult to handle due in part to the low Young's modulus, hence requiring very large thicknesses to handle appropriately. In addition, polyimide 2611 (often chosen because its water permeability is lower than that of other polyimides) has a Young's modulus larger than that of parylene C. It has been suggested that polyimide arrays often are too rigid and can damage the retina. In addition, they tear quite easily. Parylene C handles very well under surgical manipulation, and, as we will show, behaves very well when implanted. In addition, the thickness of parylene films is determined by the mass of dimer placed in the vaporizer. As such, thicknesses can be very thin or very thick, and thicknesses are very repeatable and well controlled, more so than spin-on coatings, especially when deposited over step junctions. Parylene thickness can be controlled so as to match the rigidity to the application of interest, more easily than most other materials. Since parylene is deposited at room temperature (we have verified this using Temp-Plate irreversible temperature recorders traceable to NIST (Wahl Instruments, Inc., Asheville, NC, USA)), the coating process is post-IC compatible. Parylene C is also optically transparent, enabling the anatomy to be seen through the cable and the array during ophthalmic surgery, post-implantation examination, and follow-up. While many groups use parylene C as a coating

Table 2-3. Parylene coating functions for selected medical applications (adapted from [70])

Property	Parylene N	Parylene C	Parylene HT
Catheter mandrels	Lubricity	--	High temperature stability
Endoscopic devices	Dielectric, lubricity	--	--
Animal RFID	--	Water barrier	--
Pulse generators/ Electronic circuits	--	Water barrier, dielectric, biocompatibility	--
Pressure sensors	--	Water barrier, dielectric, biocompatibility	--
Stents	--	Biocompatibility, water barrier, primer	--
Cochlear implants	--	Water barrier, dielectric, biocompatibility	--
Blood-handling components	--	Chemical resistance, biostability	--
Needles/syringes	Lubricity	--	Lubricity, water barrier
Cannulae	Lubricity	--	--
Analytical lab components	--	Chemical resistance, biostability	--
Ocular implants	--	Biocompatibility, water barrier, dielectric, mechanical strength	Biocompatibility, water barrier, dielectric, UV stability, process temperature stability

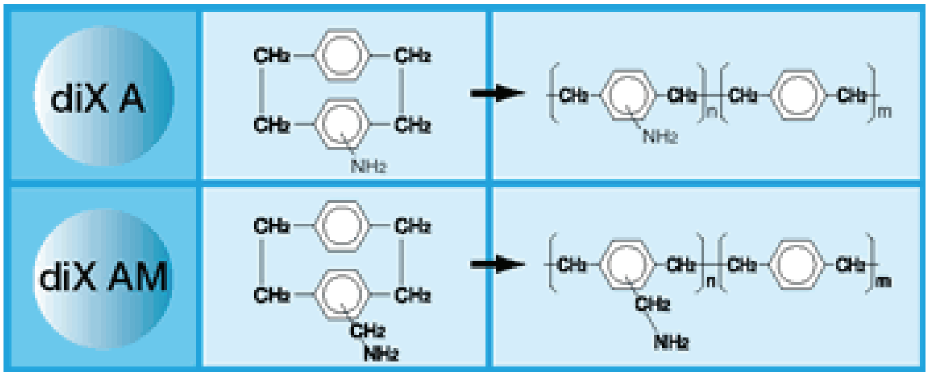

Figure 2-8. Chemical structures of Kisco amino parylenes [79].

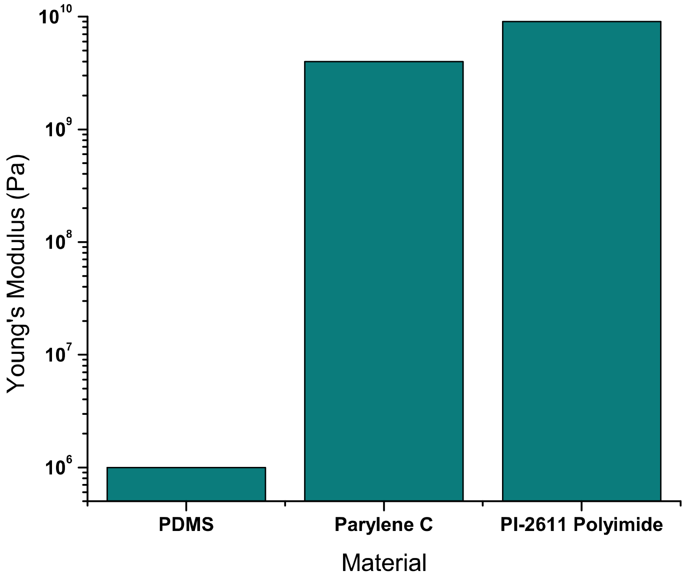

Figure 2-9. Comparison of Young's moduli of various materials. Ordinate is logarithmic.

on their arrays for many of these reasons, we have chosen to use it as the main substrate for our devices [80, 81], a paradigm that leverages these advantages to the greatest extent. The new high-temperature stable [82] variant of parylene, parylene HT, has also been used to fabricate iridium electrode arrays. We will show that while evaporation and patterning of iridium is unsuccessful on parylene C due to the high melting temperature of iridium, parylene HT lends itself to such a process, and we present this as another possible technology for ensuring good charge delivery to neural tissue.

Although parylene is known to be biocompatible in many sites of implantation, in order to initially assess the intraocular biocompatibility of the material in the unique immune environment of the eye, an approximately 2 cm × 0.5 cm piece of unmodified 20 μm thick parylene C was implanted in the vitreous cavity of the right eyes of two rabbits for six months (Figure 2-10). The retinas of the right eyes of both rabbits were compared post-mortem with those of their left eyes that served as controls. Histological evaluation (all histological sections are shown in Figure 2-11 and a detailed comparison of two sections is given in Figure 2-12 with layers identified) reveals no discernable difference between right and left eyes, indicating that there was no detectable adverse immune response affecting the retina due to parylene implantation in the vitreous cavity. These results supported the tenet that parylene C is a biocompatible bulk material for an intraocular retinal prosthesis and other ocular implants, and paved the way for the design and fabrication of a flexible electrode arrays and a packaging system using parylene C as the primary substrate. Given these biocompatibility results, we have also been investigating parylene in several other ocular implants, with excellent results to date [83-85]. Similar experiments were performed with parylene C implanted on the spinal cord of mice. The arrays were well tolerated, with no obvious immune reaction or gliosis.

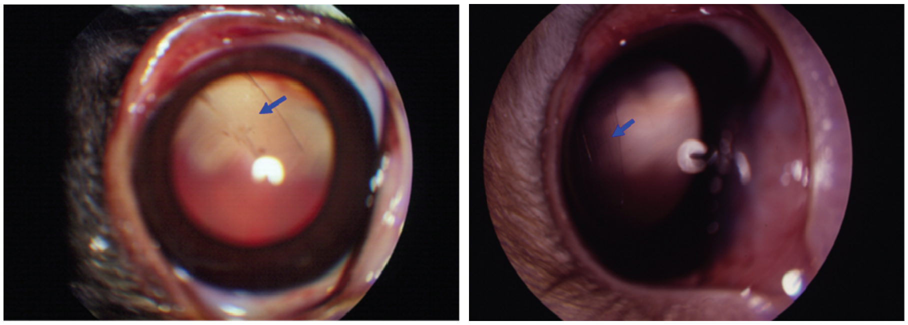

Figure 2-10. Parylene C implanted in the vitreous cavity of the rabbit eyes for six months.

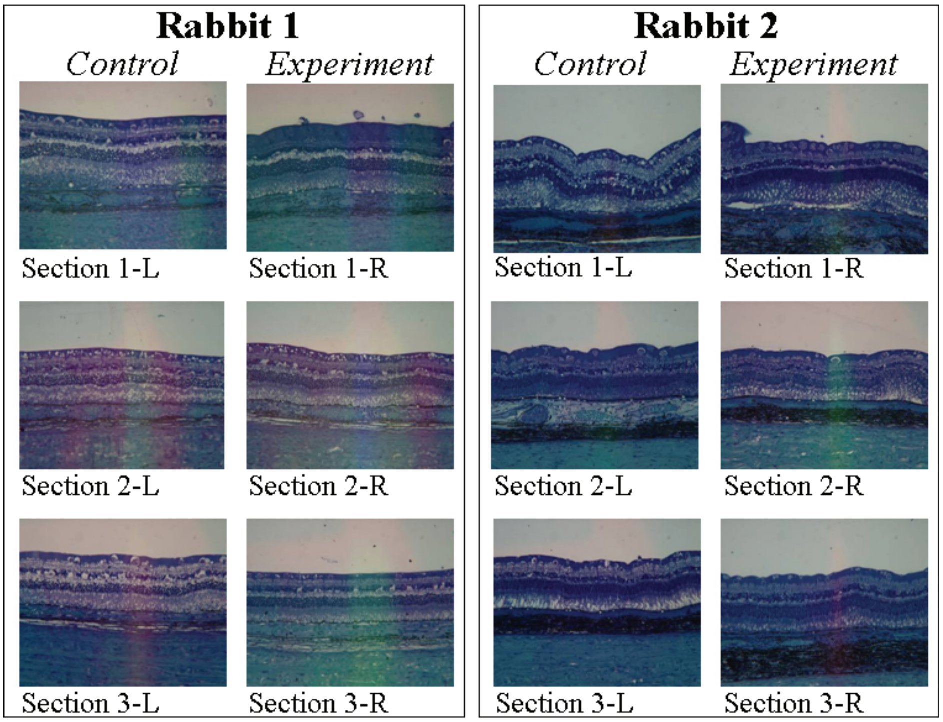

Figure 2-11. Histological sections of the retinas of the left and right eyes of two rabbits after parylene C implantation in their right vitreous cavities for six months. Courtesy of Dr. Dilek Guven.

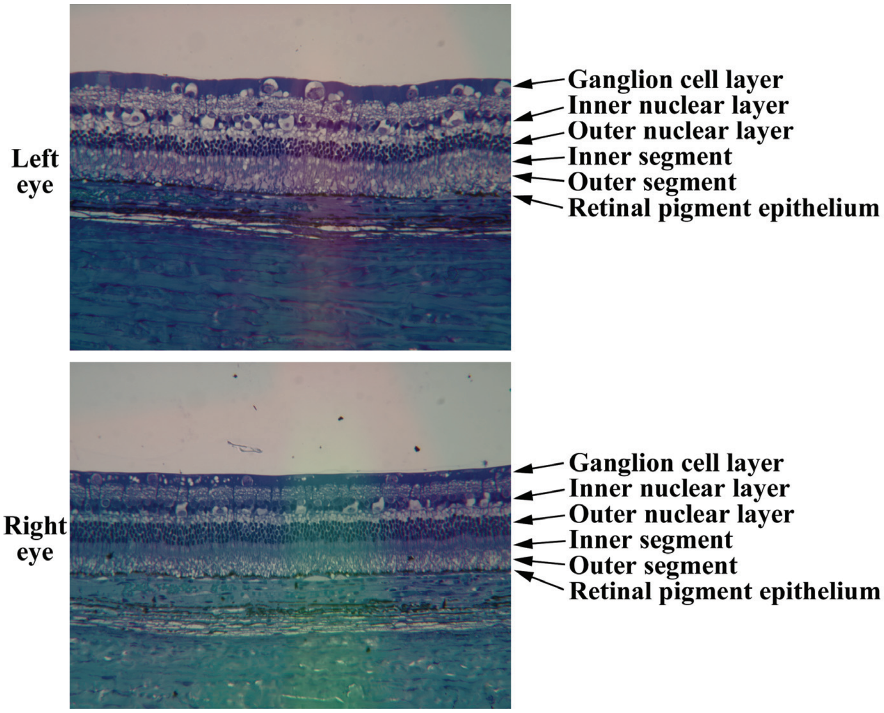

Figure 2-12. Typical morphology of rabbit retinas after parylene C implantation in the right eye for six months (Left eye: control, Right eye: experiment).

2.3 Introduction to Microelectrodes

The term “multielectrode array” historically refers to a rigid substrate on which electrodes are fabricated for *in vitro* studies. However, gradually this term is being used to describe any device, flexible or rigid, on which multiple electrodes have been fabricated, for *in vitro* or *in vivo* applications. Thus, our arrays will be referred to as multielectrode arrays, or MEAs.

It is critical to understand what happens when an electrode is placed in solution, as well as some of the important methods of studying electrodes, the essential aspects of which will be briefly covered here, but the details of which are beyond the scope of this dissertation. Interested readers can consult many excellent references for further in depth analyses of the subject [34, 86-88].

2.3.1 Charge-Transfer Mechanisms and Cellular Excitation

There are several possible mechanisms by which charge can be transferred from an electrode to tissue. When an electrode is placed in an electrolyte, such as the saline containing many chlorine ions present in the human body, and a voltage is applied to it, the electrode can capacitively affect the electrolyte, generating ionic flow that can stimulate tissue, by the so-called non-Faradaic mechanism. Electrons at the electrode surface attract positive ions in the solution to the electrode surface, but no charge is transferred. The positive ions are hydrated such that a dielectric layer of water separates them from the electrode surface. The overall consequence is that a capacitance between the electrode and the ions in solution, known as the Helmholtz double layer, is created. A line drawn through the electrical centers of these ions defines what is known as the Outer

Helmholtz Plane (OHP). Past this, there is a diffuse arrangement of charge in the diffuse layer that ends at a distance known as the Debye length, at which point bulk solution is now present. In concentrated solutions, the Debye length can be neglected, and charge transfer occurs as by charging of a parallel-plate capacitor [34]. By this mechanism, no real charge is passed from the electrode to the solution, and damage to tissue and electrodes are limited. However, this mechanism is limited to 20 $\mu C/cm^2$ of charge transfer of real electrode surface area [89]. Beyond this level, real charge transfer begins to take place in the so-called Faradaic reactions.

In Faradaic reactions, ionic flow is induced by oxidation-reduction (redox) reactions. These reactions can be reversible, which is the case when the chemistry is confined to the electrode surface, and can be negated by running an identical current in the opposite direction for the same amount of time (addition and removal of the same quantity of charge). In these reactions, no new chemicals are generated in the bulk solution that are capable of diffusing away. Examples of reversible Faradaic reactions are oxide formation at platinum and iridium surfaces (equations (1) and (2)), and hydrogen atom plating at platinum surfaces [34] (equations (3) and (4)).

$$\mathrm{Pt} + \mathrm{H_2O} \Leftrightarrow \mathrm{PtO} + 2\mathrm{H^+} + 2\mathrm{e^-} \tag{1}$$

$$\mathrm{Ir} + 2\mathrm{H_2O} \Leftrightarrow \mathrm{Ir(OH)_2} + 2\mathrm{H^+} + 2\mathrm{e^-} \tag{2}$$

$$\mathrm{Pt} + \mathrm{H^+} \Leftrightarrow \mathrm{Pt\text{-}H} \tag{3}$$

$$\mathrm{Pt} + \mathrm{H_2O} + \mathrm{e^-} \Leftrightarrow \mathrm{Pt\text{-}H} + \mathrm{OH^-} \tag{4}$$

If charge delivery exceeds this reversible limit, then irreversible Faradaic reactions occur. These generate new chemical species in the bulk solution that are capable of diffusing away from the reaction site, or of bubbling out as a gas. Such reactions include the electrolysis of water when outside the "water window" (equations (5) and (6)), or platinum corrosion (equation (7)) and chlorine ion oxidation (equations (8) and (9)). It is important to note that Faradaic reactions typically will not affect other organic materials in the biofluid for a number of reasons, most notably because noble metals in the presence of chlorine serve as poor catalysts for such reactions [89].

$$2H_2O + 2e^- \Rightarrow H_2\uparrow + 2OH^- \tag{5}$$

$$2H_2O \Rightarrow O_2\uparrow + 4H^+ + 4e^- \tag{6}$$

$$Pt + 4Cl^- \Rightarrow [PtCl_4]^{2-} + 2e^- \tag{7}$$

$$2Cl^- \Rightarrow Cl_2\uparrow + 2e^- \tag{8}$$

$$Cl^- + H_2O \Rightarrow ClO^- + 2H^+ + 2e^- \tag{9}$$

Cells at rest have a negative resting membrane potential (the inside of the cell is negative with respect to the outside). In order to bring an electrically excitable cell to threshold, a negative, cathodic (electron-mediated) current is usually injected from a stimulating electrode. This causes a rise in the voltage across the cell membrane (depolarization) above threshold and ionic movement then propagates an action potential. The minimum current needed to bring a cell to threshold with an infinitely large pulse duration is called the rheobase (b) (shown in Figure 2-13, an example strength-duration curve for a cell), a property which is affected by the distance between the cell and the electrode as well as cell size and membrane properties. The chronaxie time of the cell (c), which is determined by its time constant of depolarization, is the value of the pulse duration (d) at twice the rheobase current, and is the duration with the lowest energy requirement for stimulation (d = c) (Figure 2-13). As will be discussed, in order to negate the effects of cathodic stimulation and its associated reduction reactions, application of an

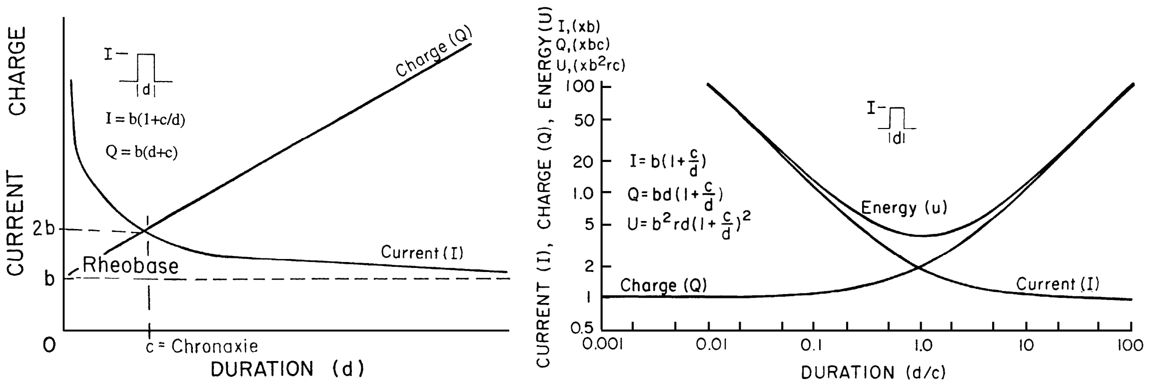

Figure 2-13. Normalized strength-duration curves and expressions for current and charge defining chronaxie and rheobase. b: rheobase; c: chronaxie; d: pulse duration; I: current; Q: charge (=I×d). Energy required for stimulation is lowest when duration is set at the chronaxie time. Adapted from [90].

anodic pulse of the same charge magnitude, but opposite in sign, is usually used to affect the reverse, oxidation reactions.

In most cases of electrical stimulation, the non-Faradaic charge injection limit of 20 $\mu C/cm^2$ is unreasonably low because of diffusion and charge spreading in the tissue, such that the voltage gradient across the cellular membrane is not altered sufficiently to bring the cell to threshold. It is thus important to choose materials whose reversible limits are high enough to transfer sufficient charge for electrical stimulation of the tissue of interest, a topic which will be discussed after a look at the Randles circuit model of the electrode-electrolyte interface.

2.3.2 Randles Equivalent Circuit

John E. B. Randles, one of the most important theorists in the field of electrochemistry, devised a circuit model (Figure 2-14) in 1947 to describe the electrode-electrolyte junction [91]. He described the interface as a capacitor, the Helmholtz double-

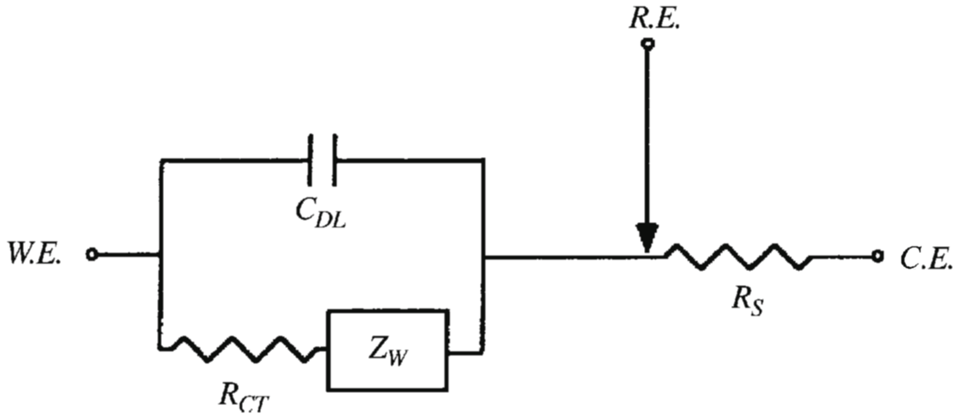

Figure 2-14. Randles equivalent circuit for electrode-electrolyte interface. W.E.: working electrode; R.E.: reference electrode; C.E.: counterelectrode. Adapted from [92].

layer capacitance, in parallel with an impedance to charge transfer, all in series with a solution, or tissue, resistance. The charge transfer impedance is made up of a resistance and the Warburg impedance, a term that is mostly negligible at the frequencies used in electrical stimulation. As a result, the junction circuit model can be simplified to a resistor, R_{CT}, in parallel with a capacitor, C_{DL}, all in series with a solution resistance, R_S. C_{DL} is approximated by the expression

$$C_{DL} = \varepsilon_0 \varepsilon_r \frac{A}{d_{OHP}} \tag{10}$$

where d_{OHP} is the distance between the two “plates” of charge, A is the electrode area, and ε_0 and ε_r are the permittivities of free space and the dielectric constant of the solution, respectively. The impedance at the phase boundary can then be simplistically modeled as:

$$Z = \frac{1}{\frac{1}{R_{CT}} + j\omega C_{DL}} + R_S \, . \tag{11}$$

At low frequencies, the parallel circuit has a profound effect on the total impedance. At high frequencies, the impedance is dominated by the tissue (and cabling) resistance, because the capacitor acts as a short. It is clear, then, that frequency plays a major role in electrode behavior, but it is only one of the many factors determining stimulation and recording efficacy. The main methods used to characterize electrodes will now be discussed.

2.3.3 Evaluation of Electrodes and Electrode Materials

2.3.3.1 Electrochemical Impedance Spectroscopy

The first method of electrode analysis is electrochemical impedance spectroscopy (EIS). In this setup, three electrodes are used. One is the electrode under study, the working electrode. The counter electrode (also called the secondary or auxiliary electrode) corresponds to the other end of the circuit, closing the circuit, and is usually a high surface-area platinum electrode. The third electrode is the reference electrode, which is usually a silver/silver chloride (Ag/AgCl) electrode. This electrode sets the zero potential of the cell because its relative potential varies insignificantly during the experiment. A sinusoidal alternating current is applied, and phases and impedance magnitudes are graphed as a function of frequency. Depending on the type of electrode, the typically chosen 1 kHz frequency can be located in various regimes of the magnitude plot. It is often important to show complete magnitude and phase data for electrode behavior, but 1 kHz impedance data is that most often presented [34].

2.3.3.2 Cyclic Voltammetry

Cyclic voltammetry (CV) is the method of choice of electrochemists for determining charge delivery capacity, and for investigating the behavior of an unknown analyte or to compare electrode materials using a common electrolyte. In this technique, also done using three electrodes, a potential is applied between the working and the reference electrodes and the current to the counter electrode is measured. The potential is swept at a constant slew rate, also known as the scan rate, from a starting potential to a reverse potential and then back to the starting potential, usually at 50 mV/s or 100 mV/s. The starting and reverse potentials are chosen so that they usually fall just within the limits of the water window, or the voltages at which water hydrolysis occurs, so that the electrode is cycled to its fullest extent. These data are then graphed on a current-voltage plot. Characteristic peaks of Faradaic charge transfer will be seen (Figure 2-15), corresponding to the presence of an electrochemical reaction occurring at that potential. In a fully reversible reaction, peaks on the reverse sweep will serve to negate the effects of reactions occurring in the peaks of the forward sweep. If forward and reverse peaks do not correspond, it is likely that an irreversible reaction has taken place during the sweep. By integrating the area under the curve for the forward sweep, or the area over the curve for the reverse sweep in fully reversible reactions, charge delivery capacity, or Q_{CDC} can be determined. Table 2-4 lists the maximal Q_{CDC} values reported for various thin-film materials at low sweep rates. It is important to note, however, that under faster pulsing, as

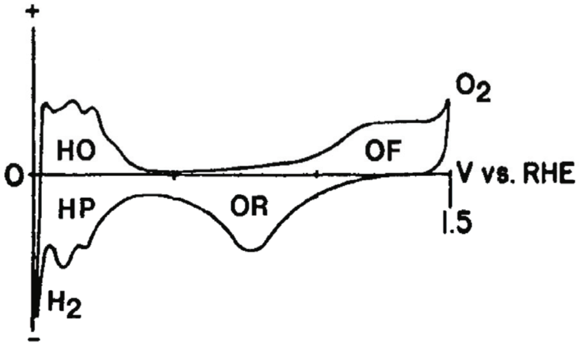

Figure 2-15. Typical CV for a platinum electrode. HO: hydride oxidation; OF: monolayer oxide formation; O_2: oxygen gas evolution; OR: monolayer oxide reduction, HP: Hydrogen atom plating; H_2: hydrogen gas evolution. Scan Rate: 100 mV/s. Electrolyte: 0.1 M phosphate-buffered saline. Adapted from [89].

in the case of neuronal stimulation, only a fraction of this capacity is available for charge injection [93, 94]. Gold likely does not demonstrate sufficient charge delivery capacity for neural stimulation from electrodes of realistic size (the neural damage limits are currently accepted as 1 mC/cm^2, but pulsing near this value may be necessary for percepts or functional neuromodulation to be elicited). Titanium nitride electrodes are non-Faradaic, with a flat CV [95], and are sputter deposited in a microcolumnar structure. However, they have not yet demonstrated charge injection capacities high enough for high current-density stimulation [95]. In addition, the biocompatibility of the material is unknown [95], and, in fact, the presence of TiN has been shown to increase cell death of retinal glial cells and neurons [96]. Other noble metals, platinum and iridium, are highly resistant to corrosion, but can do so under high current-density stimulation. However, the surface area of as-deposited platinum tends to be quite flat (especially when evaporated). As will be seen, electroplating of platinum enables a dramatic surface area increase for charge transfer. Iridium is an intriguing material because its charge delivery capacity is much higher and, as will be discussed later, can be oxidized and activated to achieve even higher Q_{CDC} values. The biocompatibility of iridium and iridium oxide, especially for use in the eye, is still a subject of debate.

Table 2-4. Reported maximal charge delivery capacities of various thin-film metals, adapted from [97] (note that only a fraction of total Q_{CDC} is available under more rapid pulsing, but relative placement is realistic)

Material	**Q_{CDC} (mC/cm^2)**
Au	0.490
TiN	0.687
Pt	4.134
Ir	17.078
IrO_x	28.450
IrO_x (after activation)	95.100

Metals are usually deposited via three major mechanisms. In thermal evaporation, quantity of metal is heated either by resistive heating of a boat holding the material, or by magnetically steered electron beam (e-beam) bombardment of the surface of a material held in a crucible. The samples to be coated are placed on a holder above the vaporizing material, and are often rotated to enhance uniformity or step coverage. Because deposition occurs in a vacuum, the mean free-path of the material is such that it strikes the sample without deflection. Resistive thermal evaporation is generally confined to materials that have relatively low melting temperatures (e.g., gold, aluminum), whereas high melting-temperature materials such as platinum and iridium must be e-beam deposited. Oxidation of the material is also minimized during deposition. Metals can also be sputtered via impingement with positive ions of argon or xenon or other inert gases, which causes metal to be released from a target and to land on the substrate. As opposed to thermal evaporation, sputtering is a relatively dirty process because a target is reused many times and the deposition pressure is generally higher. Sputtering, however, can generate higher surface-area materials and can be used to deposit certain materials that are not trivial to melt. Finally, metal can be deposited via wet deposition, either electroless/autocatalytic (especially nickel) or electoplating. These processes have the advantage that material can be deposited as very high surface-area coatings as well as on materials of complex geometry, but often add complexity to the fabrication process.

2.3.3.3 Current Pulse Testing

In current pulse testing, a current is applied to an electrode and the resulting voltage fluctuation is measured. A typical biphasic cathodic-first current waveform is graphed in Figure 2-16. In implantable electronics, the pulse is usually biphasic to minimize tissue and electrode damage by enabling both the forward and reverse processes in the reversible Faradaic redox reactions to occur. This test mimics the activity of the electrode when used in practice, with the exception that the pulse parameters can be changed to accelerate the test, by changing the pulse period T (inverse frequency) or test multiple phase width (t_{pw}), pulse width, and intra- and inter-pulse intervals (d and t_{ip} respectively). The recording of the voltage response gives insight into the impedance of the electrode-tissue circuit, as well as the presence of afterpotentials which can mask recordings taken just after stimulation such as in cardiac-pacing applications [34]. It is important to realize that it is significantly easier, and thus safer, to provide charge-balanced current pulses than it is to provide charge-balanced voltage pulses because of the complexity of the RC network in the Randles circuit. Hence, it is unusual to provide voltage-controlled pulses [34]. In addition, when a metal of a higher surface area is compared with an identical metal with a flat surface, the voltage excursion when injecting

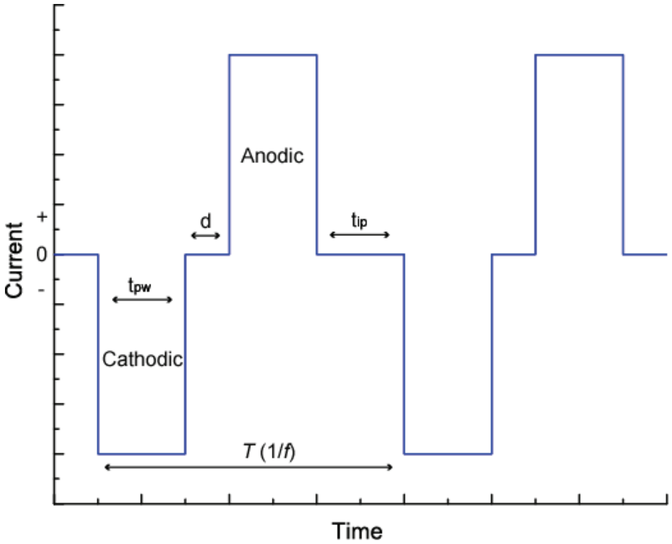

Figure 2-16. Common cathodic-first biphasic pulse and associated defining parameters. T_{pw}: phase width; d: intra-pulse delay; t_{ip}: inter-pulse interval; T: period (inverse frequency).

the same amount of charge over a given geometric area is significantly lower, a property that can minimize corrosive effects on the electrode, and thus enhance electrode longevity. Typical currents used for stimulation of the human retina vary from 50 μA to 500 μA for 1 ms per phase across 520 μm diameter platinum electrodes (0.024 to 0.24 mC/cm^2 of geometric area, below the 0.35 mC/cm^2 safe limit generally accepted for platinum). In general, as electrodes get smaller, the amount of current it is possible to inject without going over the electrochemical safety limit is also decreased. At some point, a smaller electrode will not be able to inject enough current to bring cells to threshold and generate action potentials without exceeding this limit, and at that size should not be used for stimulation. However, even very small electrodes can record cell activity. Some frequencies of stimulation can select certain cell types over others (e.g., ganglion cells over presynaptic bipolar or amacrine cells [98, 99]).

2.4 Conclusions

The basics of microelectromechanical systems and the processes behind their fabrication have been discussed, with a focus on photolithography as an enabling technology for MEMS, as well as on the differences between bulk and surface micromachining. Parylene, a unique polymer for a plethora of reasons, has been introduced, with a discussion of its advantages over other commonly used materials for microelectrode arrays. Finally, an introduction to microelectrodes and methods of studying the electrode-electrolyte/tissue interface were presented, with a particular emphasis on several of the different metals from which it is possible to choose for charge injection.

3 MULTIELECTRODE ARRAYS FOR RETINAL STIMULATION AND RECORDING

3.1 Introduction

As discussed in Chapter 1, one of the main goals of this work is to design and fabricate multielectrode arrays for retinal stimulation. From Chapter 2, we know that such multielectrode arrays would also be capable of retinal recording action potentials as well. In this chapter, we discuss our goal of a chronically implantable parylene-based retinal stimulation system capable of high-resolution stimulation of the retina in patients with outer retinal diseases such as AMD and RP. We begin with an overview of such a system, followed by a discussion of the fabrication methodologies for single-metal layer and multi-metal-layer parylene-based MEAs. A discussion of a novel heat-molding and annealing process we have developed follows, a technology that promises to increase the mean time to failure (MTTF) of such devices, as well as discussion of an electroplating methodology that theoretically would also enable increased electrode longevity and efficacy under chronic stimulation. The results of a stimulation and recording study on vertebrate retina using parylene-based electrode arrays are presented, showing the ability of our arrays to elicit retinal responses in a manner similar to phototransduction, as well as a discussion of chronic six-month implantation tests of parylene-based arrays in canine eyes. The results of electroplating tests are also presented, showing preliminary evidence that this technology does indeed increase the longevity of electrodes under chronic pulsing at near threshold limits for the geometric area of our platinum electrodes. The novel material, parylene HT, will be presented as part of a method for fabricating iridium electrode arrays. Some concluding remarks and future work follows.

3.2 System Overview

As previously introduced, a chronically implantable retinal prosthesis requires, at a minimum, a power source and an electrode array for stimulating the electrically excitable cells retina. This power source can be light itself (in the case of photodiode electrode arrays), an implanted battery, or a wireless transmission system. Because of the high power requirements for such a device, implantable batteries are an inelegant solution, because, unless technology improves dramatically over the next few years, the battery would need to be replaced constantly. Photodiodes have not been shown to be able to provide sufficient charge to stimulate the neurons of interest. In addition, photodiode electrode arrays are hard to assess objectively in a clinical setting for the simple reason that they are always “on,” so studies evaluating their efficacy are at best extremely difficult, in comparison to those powered by wireless telemetry. In fact, a wireless system provides an added advantage that the external components of the system (such as the camera, the data processors, and the battery) can be upgraded over time. It is possible to place a camera inside the eye as well [100, 101], so that vision would be more natural (foveation instead of turning of the head to centralize a scene or object of interest would be possible).

In a typical implementation, then, external to the eye would be a camera, responsible for picking up the visual signal, circuitry for converting this image into a data stream that can be sent wirelessly into the eye, radiofrequency (RF) coils for data and power transmission, and an external battery. For an all-intraocular system, which we believe to be optimal because there are no open potential routes for infection or fluid loss, the intraocular components, as shown in Figure 3-1, would be one or two RF coils for receiving the wireless power and data signal, circuitry (application-specific integrated circuits (ASICs) and discrete components such capacitors, diodes, and oscillators) for converting this into simulation pulses [102-104], a flexible cable, and a high-density multielectrode array. The component of primary importance that serves at the interface between the tissue and the engineered device is the multielectrode array, on which this chapter focuses.

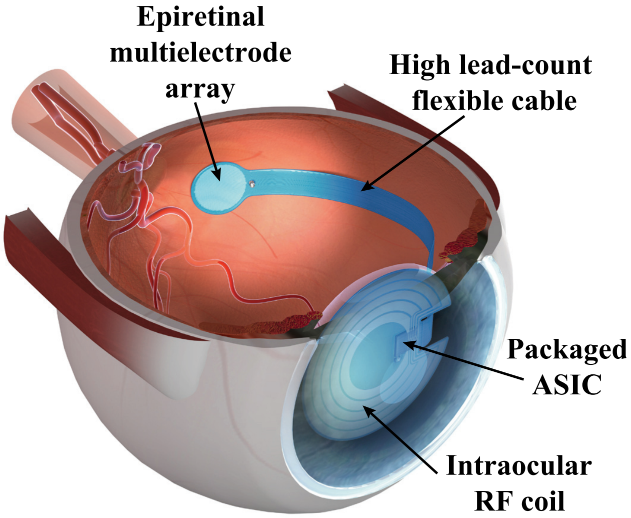

Figure 3-1. Components and proposed placement of next-generation intraocular retinal prosthesis.

3.3 Fabrication

3.3.1 Process Development

In order to fabricate high-density multielectrode arrays and cabling in parylene that are capable of providing adequate charge delivery to the tissue, a novel method for depositing and patterning a high charge delivery capacity material such as platinum on parylene had to be developed. Platinum is a notoriously hard material to work with on polymers. This is largely due to a lack of a well-defined yet controllable platinum wet etch, and because its adhesion to many materials is bad. Aqua regia, whose contents are concentrated nitric acid and concentrated hydrochloric acid typically mixed in a 1:3 ratio, is capable of etching platinum through a complex chemical reaction. The etch, however, is difficult to control, and for application to microdevices and especially multielectrode arrays, the difficulty lies in the fact that any overetching can quickly remove small features. In our first multielectrode array fabricated of platinum, our goal was a technology capable of defining traces of 6 μm width. Aqua regia was not well controlled enough to accomplish this.

A technique for fine features that is well known in the IC industry is metal liftoff. With this technique, a negative image of a design is used. Instead of retaining a photoresist mask where we want the features to be (a positive image), we keep the photoresist mask over areas in the design where we do not want the features to be (and remove the photoresist where the features are designed to be, a negative image) (Figure 3-2). Then, under metal deposition, the metal only lands on the surfaces where we want the features. The remaining mask photoresist is then removed, leaving only the design of interest on the device.

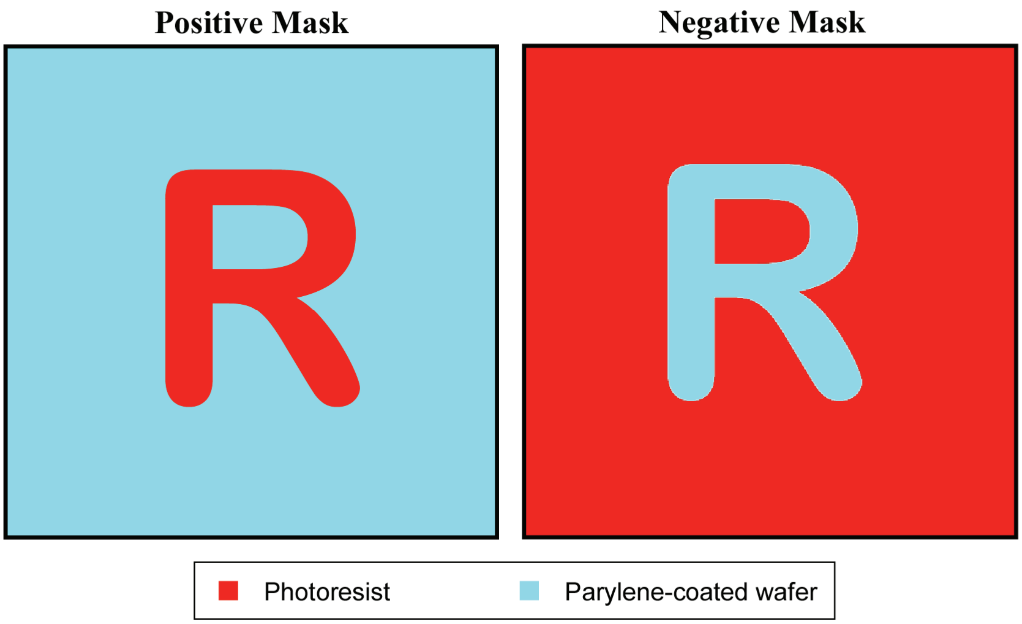

Figure 3-2. Positive and negative photoresist masks. For liftoff, a negative mask is chosen, so that the metal lands directly on the parylene surface to form the feature of interest.

Perhaps most important in this technique is the ability to create, ideally, photoresist sidewalls of a reentrant profile. As depicted in Figure 3-3, when metal is deposited on sidewalls that are of a non-reentrant profile (positive slope), there is usually continuity, or step coverage, of the film over the photoresist sidewall. When an attempt is made to subsequently remove this photoresist, the solvent does not have direct access to the photoresist, as it is covered completely with metal. In addition, any breaking of the metal continuity results in tearing of the film at uncontrollable points. These metal “tags” result in a very “dirty” appearance, can short adjacent features together if they are very closely spaced, and are very difficult to remove, even using such techniques as ultrasonication. In contrast, when a metal film is deposited across a reentrant (negatively sloped) sidewall, step coverage is extremely difficult to achieve. Thus, no tearing of the film occurs when the photoresist is removed, and the resulting liftoff is “clean.”

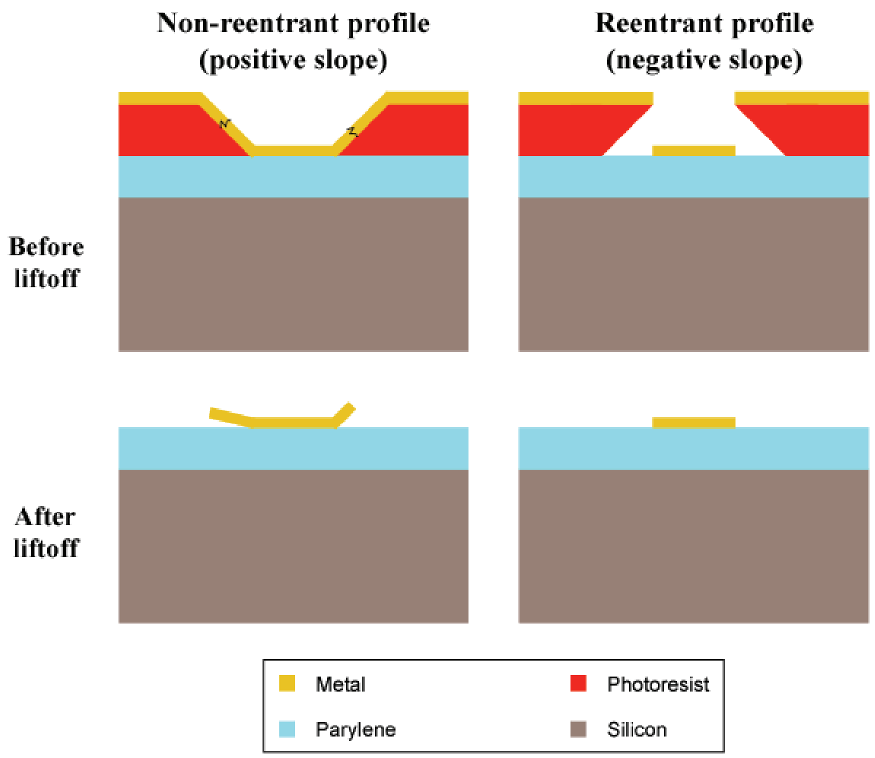

Figure 3-3. Different possible liftoff resist profiles. Reentrant profiles help achieve "clean" liftoff.

The easiest way to achieve a reentrant profile is to use a negative photoresist. Because the incident light is gradually absorbed as it traverses through the photoresist (known as the bulk effect), the cross-linking of the photoactive compound with a cross-linking agent is uneven. The top of the photoresist is cross-linked more than the bottom [105]. This gradual transition, upon development, results in the underside of a sidewall developing slightly faster than that photoresist on top, and a sidewall of negative slope. The inherent problem with negative photoresists, however, is that the cross-linking agent also serves to make the resist very difficult to remove. For applications where biocompatibility is a foremost concern, it is important that any organic residues are removed from the device.

Positive photoresists, for the very same reason of bulk effect, typically have positive sidewall slopes. The exposed regions develop faster on the top because the photoactive compound helps catalyze the material's removal in solvent. The bottom of a trench is exposed less, and hence develops slower. This typically results in a positive slope of approximately 75° to 85° [105], tending to prevent the use of positive photoresist for liftoff applications. In addition, most photoresists, both positive and negative, are not thermally stable. Due to the high thermal deposition temperature of platinum, both types of photoresist often crack, generating stray lines of metal in areas where there should be none. Important characteristics of positive and negative photoresists are summarized in Table 3-1. For these reasons, a novel liftoff technique for parylene-based processes needed exploration.

Table 3-1. Characteristics of positive vs. negative resists (adapted from [106])

Characteristic	Positive Resist	Negative Resist
Exposure	No chemical change takes place in resist that forms the image	Rely upon cross-linking for image formation
Molecular Weight	No molecular weight changes chemical reaction in non-image areas	High molecular weight products formed during exposure
Oxygen Sensitivity	No oxygen sensitivity	Have oxygen sensitivity, causing exposure problems
Removal	Easy removal, has no high molecular weight products present	Are difficult to remove, due to high molecular weight
Developing	The image is unaffected by the aqueous developer. Disposal is relatively simple	Solvent developing results in image swelling. Disposal is more difficult
Coating Thickness and Resolution	Coating thickness can be equal to or greater than minimum image size	Coating thickness must be 1/3 the minimum image size
Resist Step Coverage	Excellent, since thick coatings (2-3 μm) can be used	Marginal due to thin coating limitations
Useful for Liftoff?	Usually not	Usually

A photoresist specially developed for liftoff purposes, Lift-Off Resist (LOR), has been developed by Microchem Corp. (Newton, MA, USA). This resist is used in combination with a normal positive photoresist to define an optimal liftoff structure, as illustrated in Figure 3-4. LOR has the unique characteristic that it develops in standard developer without needing to be exposed, with a precisely controlled undercut rate that is determined by soft bake temperature and time. The LOR is spun on the wafer and soft baked at this optimized high temperature. Then, a second positive photoresist layer is spun on the LOR and soft baked and exposed as normal. The subsequent developing step is crucial for feature definition. In developer, the overlying photoresist is dissolved, and the underlying LOR begins to be removed as well in a characteristic isotropic profile. With too short a developing time (or too high a soft bake temperature), the LOR does not undercut the overlying photoresist adequately (resulting in no step discontinuity under metal evaporation). Likewise, if the developing time is too long (or the soft bake at too

1. Coat and Soft-bake PMGI or LOR.

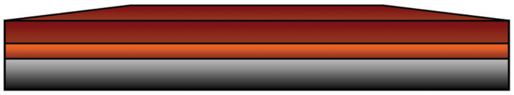

2. Coat and Soft-bake Imaging Resist.

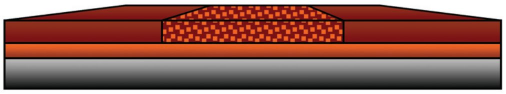

3. Expose Imaging Resist.

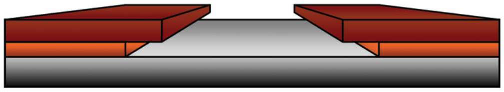

4. Develop resist and PMGI/LOR.

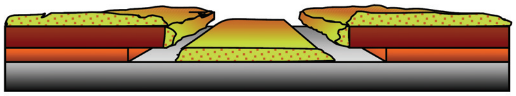

5. Deposit film.

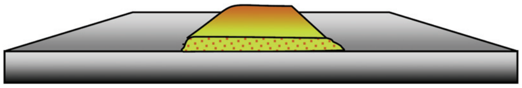

6. Lift-off Bi-layer stack and residual deposition.

Figure 3-4. Process flow of Microchem Corp. (LOR). Modified from [107].

low a temperature), the LOR is removed very quickly and narrow overlying photoresist features (such as those that define gaps between adjacent traces) are completely removed. If done just right, features such as those shown in the scanning electron microscope (SEM) image provided by Microchem Corp. (Figure 3-5) are defined. This profile facilitates the photoresist removal after subsequent metal evaporation, and assuages the metal tagging problem discussed above. One significant advantage of the use of LOR is that it is stable up to very high temperatures. Even if the imaging resist is post-baked significantly, the profile of the underlying resist does not change. In addition, even if the overlying photoresist cracks during high-temperature metallization, the underlying LOR does not. LOR is also easily removed in most N-Methylpyrrolidone (NMP)-based photoresist strippers, and comes off without residue. LOR processes are also possible for many different metal thicknesses, because the spin speed and the type of LOR chosen can be varied to accommodate liftoff of very thin to very thick films (Figure 3-6). What is more, because a competing requirement was anticipated for later versions of our electrode arrays, in which platinum depositions needed to be performed with very good sidewall coverage, we had the need for a very precisely controlled undercut. For these reasons, a process revolving around the use of LOR for these parylene-based arrays was devised.

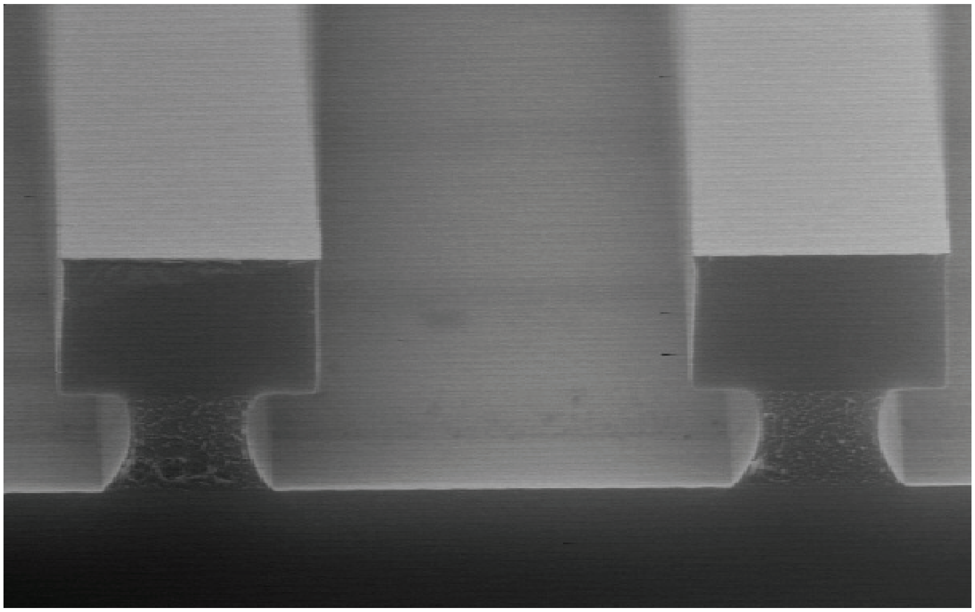

Figure 3-5. SEM of dual LOR/positive photoresist layer profile after developing. Modified from [107].

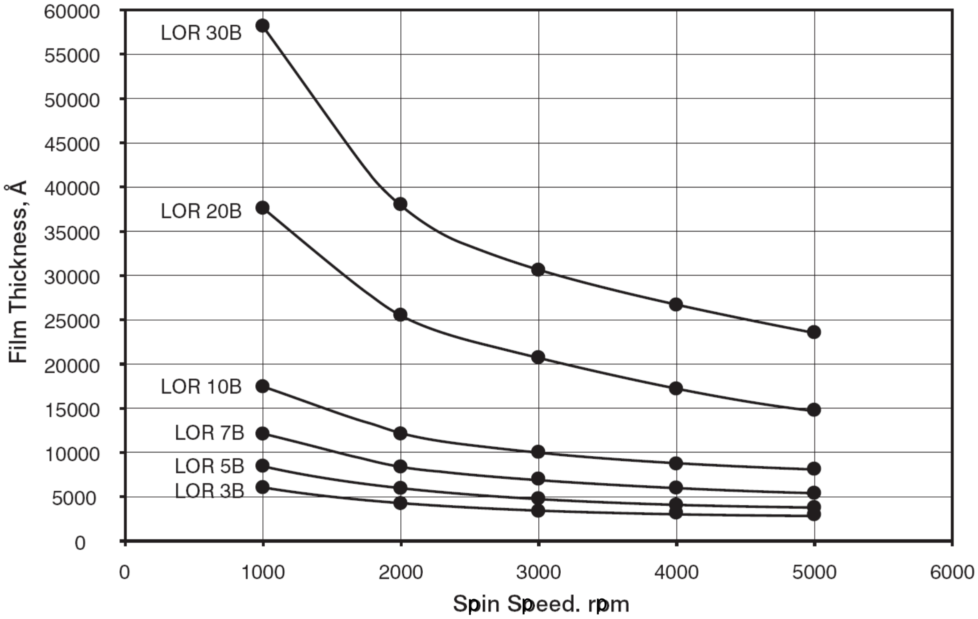

Figure 3-6. Spin speed curves for different LOR resists (from Microchem Corp. LOR Data Sheet).

We began testing photoresist films of varied types and LOR/positive photoresist films to compare liftoff processes. Gold and platinum films were also compared. Figure 3-7 depicts the problem with traditional positive photoresists when used for gold liftoff on a pattern comprising 6 µm lines with 6 µm spaces as well as electrodes and contact pads. As is clear from this image, after removal of the photoresist, many metal tags were present. In addition, many were completely broken off and lying across the traces, with the capacity of shorting adjacent lines together. Examples of similarly fabricated platinum lines on parylene are shown in Figure 3-8. Again, metal tags were present.

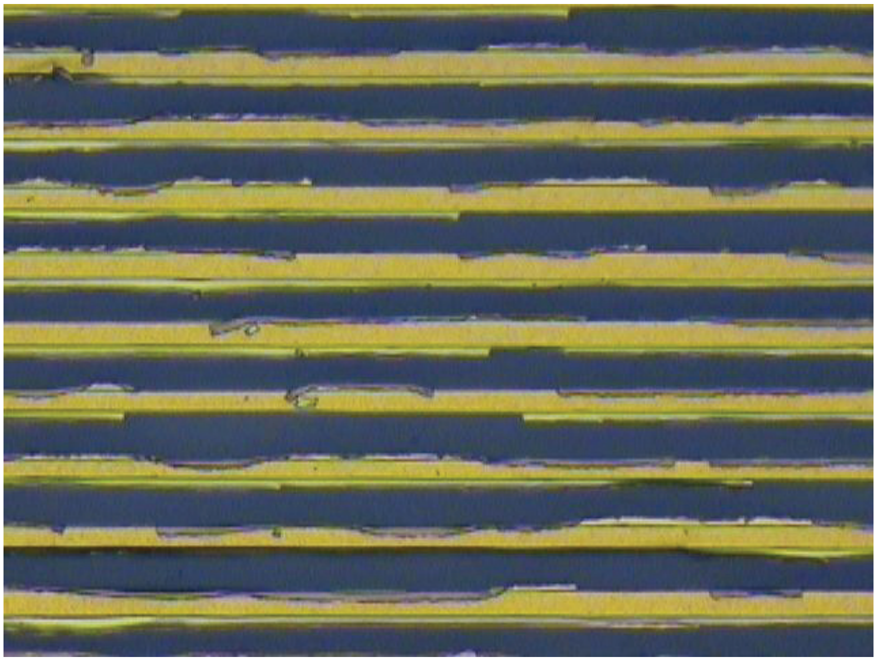

Figure 3-7. Gold liftoff process on parylene with incomplete liftoff.

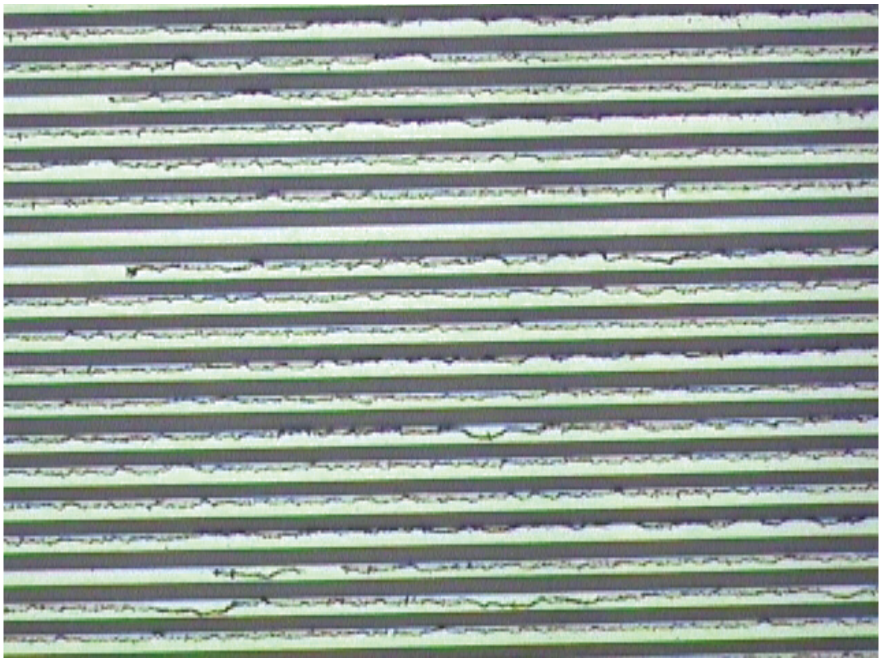

Figure 3-8. Platinum liftoff on parylene with poor results.

To obviate these and other problems, then, an investigation of LOR and compatibility with parylene C substrates was performed. As shown in Figure 3-9, before optimization, the development of the LOR/positive resist combined film was problematic. If the LOR were not baked at a high enough temperature, for the right length of time, or if the top resist were developed too quickly and the underlying resist exposed too long to the developer, the 6 μm features would be undercut. On the left, we see that the overlying resist was completely released from the substrate and was displaced from its desired position. On the right, we see the results near the electrode portion of the array. Here, the resist has been entirely washed away by the post-development rinse. Figure 3-10, on the other hand, shows the results after optimizing the process (see complete process parameters in the appendices). The features are all in their desired locations, and lines are well defined.

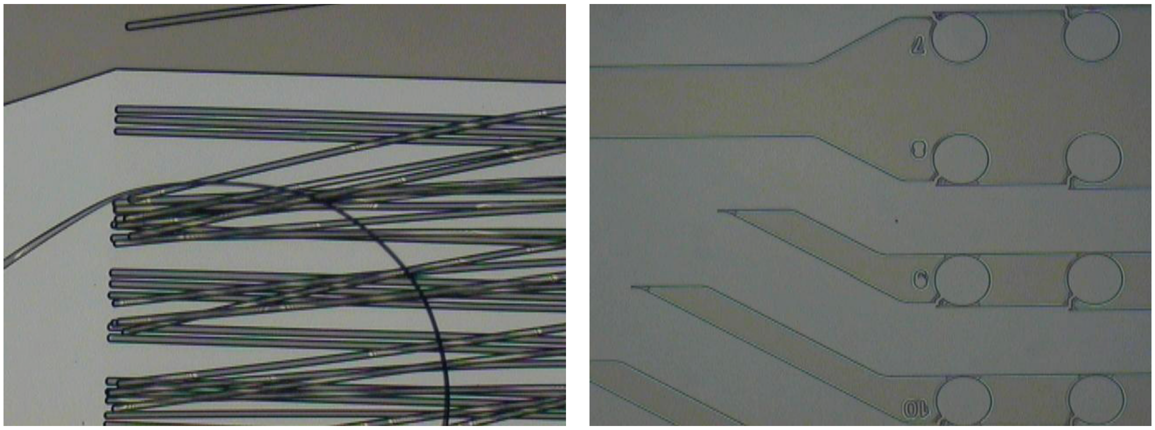

Figure 3-9. Photomicrographs showing LOR and photoresist features using non-optimal bake, exposure, and developing parameters.

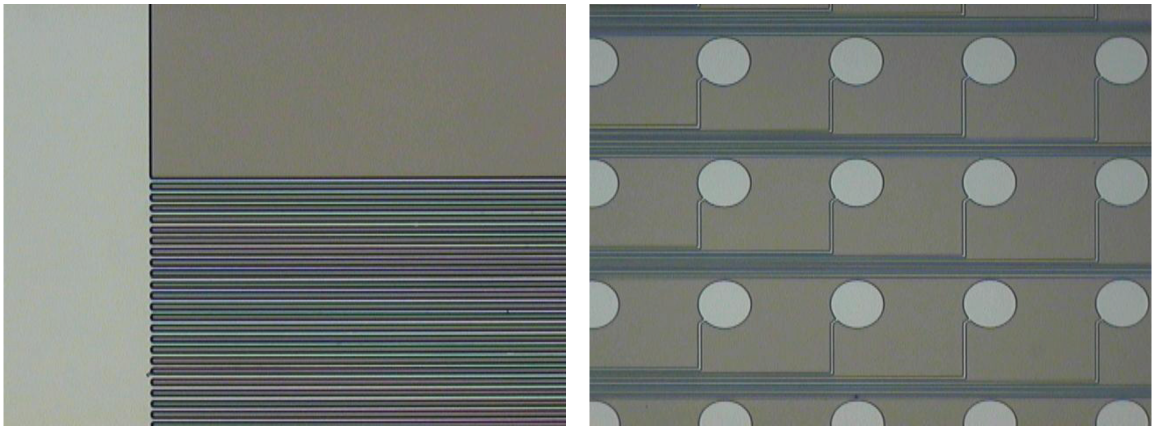

Figure 3-10. Photomicrographs showing LOR and photoresist features using optimal bake, exposure, and developing parameters.

With this technique now in hand, the complete liftoff process was attempted. One wafer was put through a titanium/gold deposition (200 Å/2000 Å) in the e-beam evaporator, and another through a titanium/platinum deposition (200 Å/2000 Å). In both cases, after liftoff, the lines and electrodes were clearly defined with no metal tags on the edges of the lines.

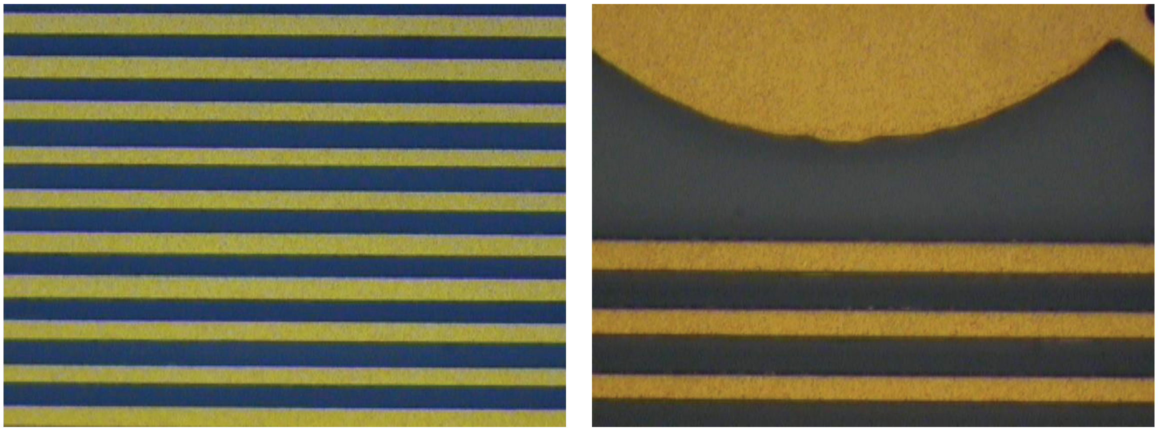

Figure 3-11. Results of titanium/gold liftoff process. All lines and electrodes are clearly defined.

Figure 3-12. Results of titanium/platinum liftoff process. Liftoff of titanium and platinum from parylene is possible with at least 6 μm resolution.

The fabrication of the electrode arrays discussed below made use of this optimized process. Small variations in exposure time and developing time had to be allowed for as the humidity and ambient temperature in the cleanroom changed, however, for the most part, there was minimal deviation from this process. This liftoff process has now become the mainstay for any metallization step involving platinum for these and other devices fabricated in our laboratory [108].

Because of the unique requirements of such implantable devices, the flexible cables typically must be far longer than the multielectrode array region of the device. On the other hand, the multielectrode array must be of very high resolution. While photolithography using contact aligners is typically done to define structures spanning a large portion of a wafer, photolithography using 5X or 10X reduction steppers is usually done to achieve very high-resolution devices with micron-scale features. Usually, such steppers are used in the IC industry to repeat a single pattern many times over the same wafer. However, in order to accommodate high-density electrode arrays with high-lead-count cables, for which a contact aligner would not achieve resolutions high enough and where the structure is not the same on neighboring die, the stepper was chosen. In this case, the program on the stepper and the design was modified to allow die "stitching," where one pattern was exposed and a neighboring pattern was overlapped slightly with the first and exposed in succession. This process was repeated until all structures in the device were defined. As an example, in Figure 3-13 we see a desired layer of photolithography for an electrode array of an approximate length of 50 mm. However, this array is clearly too large to fabricate on a stepper whose maximal exposure size is 10 mm per die. In order to accommodate this, then, the pattern was divided into three sections, as shown in Figure 3-14, where the electrode array region was one "die," the cable region was another "die," and the contact region was another "die." The cable region, shown on the bottom, could be repeated as many times as necessary to generate the final desired trace length.

Figure 3-13. Approximately 50 mm long electrode array design.

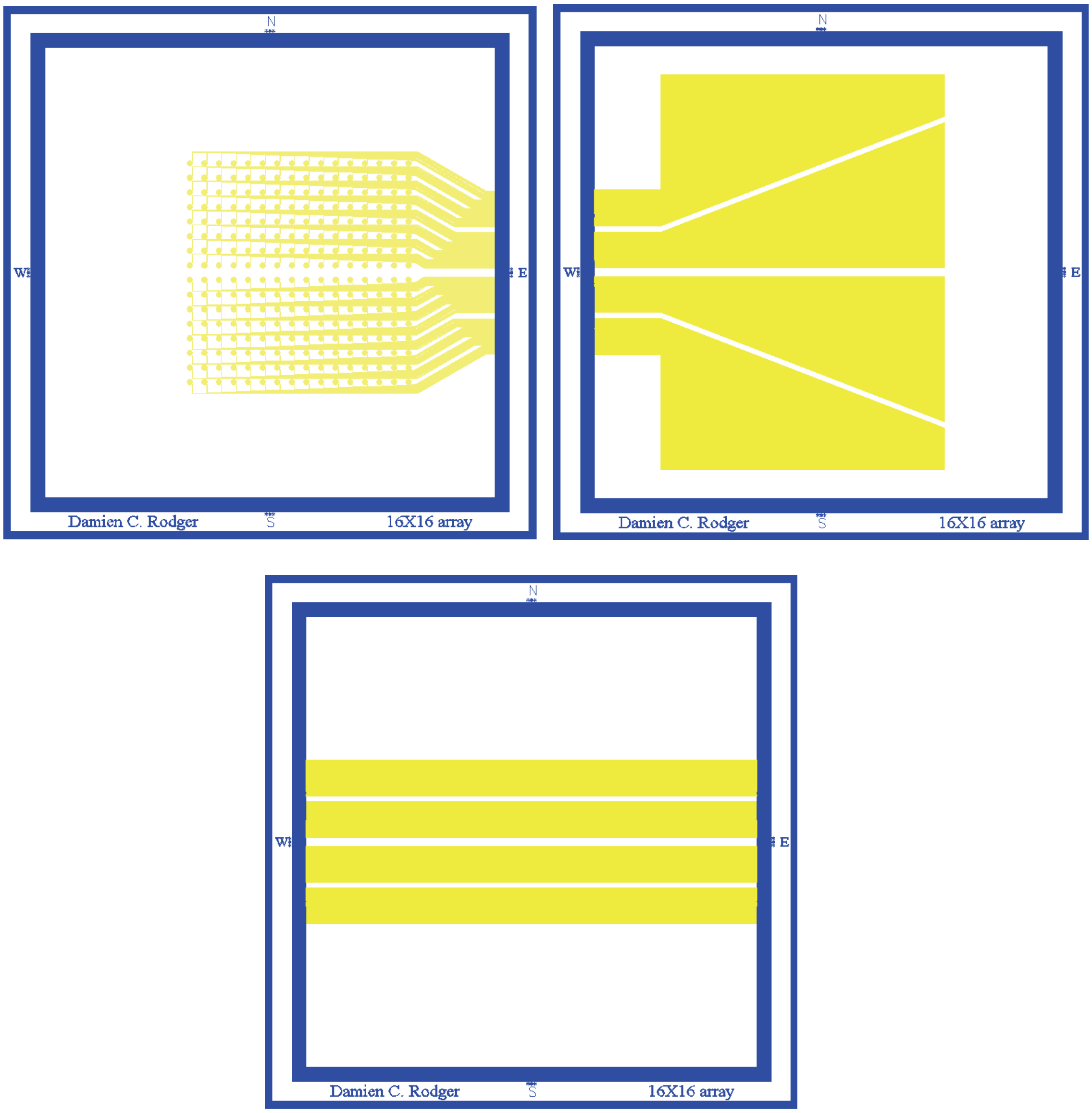

Figure 3-14. Final masks for “die” that were stitched to fabricate device in Figure 3-13. (top left) electrode array; (top right) contacts; (bottom) repeatable cable region.

3.3.2 Single-Metal-Layer Flexible MEAs

Single-metal-layer parylene C-based electrode arrays are fabricated as shown in Figure 3-15 (see details in Appendix A). A photoresist sacrificial layer is optionally spun on a standard silicon wafer. Approximately 8 μm of parylene C is then vapor deposited in a PDS2010 system (Specialty Coating Systems, Indianapolis, IN, USA) on the entire wafer. An LOR3B photoresist layer (Microchem Corp., Newton, MA, USA) and an AZ1518 layer (AZ Electronic Materials, Branchburg, NJ, USA) are spun on top of the parylene, exposed in a 10X reduction GCA Mann 4800 DSW wafer stepper (General Signal Corporation, Stamford, CT, USA) or a Kasper 2001 contact aligner (Kasper Instruments, Inc., Sunnyvale, CA, USA) depending on the required resolution of the electrode array, and developed to achieve a liftoff pattern comprising contacts, conductive traces, and electrodes. After hard bake, approximately 2000 Å to 5000 Å of platinum, with or without a 200 Å titanium layer, is then e-beam evaporated (SE600 RAP, CHA Industries, Fremont, CA, USA) on the wafer. The subsequent photoresist strip generates the desired single-layer metallization pattern. An approximately 7 μm thick coating of parylene C is then deposited, followed by a spin coating of photoresist. This photoresist etch mask is exposed over the areas of the electrodes and contact pads and to pattern the overall array geometry, and the entire wafer is then subjected to an RIE in oxygen plasma, removing the parylene insulation over the electrodes and the parylene surrounding the array. The photoresist mask is then removed with solvent. Finally, if a sacrificial photoresist layer was used, the array is released from the substrate in an acetone bath. If no sacrificial layer was used, it is peeled from the silicon in a water bath. Ultimately, for most cases, the sacrificial photoresist layer is unnecessary, and can often complicate array fabrication due to cracking while under process. The arrays can be easily released from a natively oxidized silicon surface by placing them in a deionized water bath and peeling them from their edge. The water will then release the rest of the structure due to the hydrophobicity of the underlying parylene surface.

An inherent problem with single-metal-layer arrays is that electrodes and traces are necessarily fabricated alongside each other. For high-lead-count devices, this limits the size of electrodes and tends to crowd electrodes and traces into artificial groups. To allay these problems, a dual-metal-layer approach was devised that enables traces to pass underneath overlying electrodes. The fabrication process for these dual-layer arrays is discussed next.

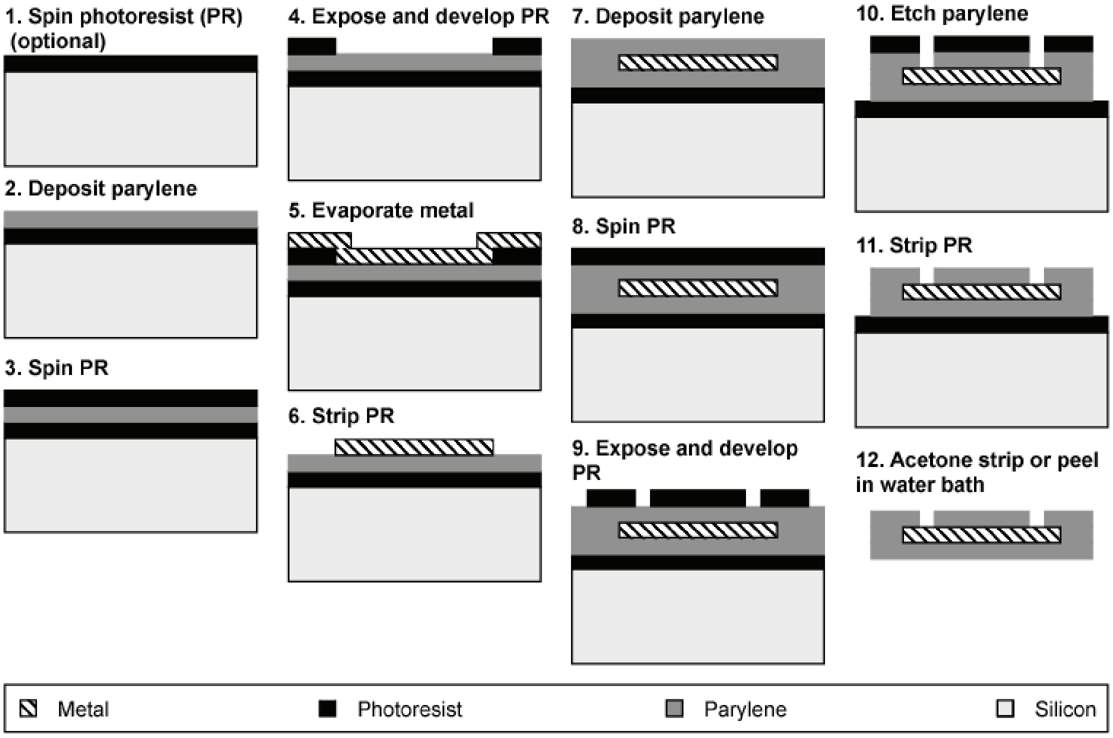

Figure 3-15. Fabrication process for parylene-based single-metal-layer flexible MEAs.

3.3.3 Dual-Metal-Layer Flexible MEAs

Dual-metal-layer electrode arrays are fabricated as shown in Figure 3-16 (see Appendix B for complete process). Approximately 8 μm of parylene C is first deposited on a silicon wafer with the optional photoresist sacrificial layer, forming the underside of the electrode array. A platinum or titanium-platinum metal liftoff process is used to define traces with 16 μm pitch and 2000 Å to 3000 Å thickness. A second parylene deposition (~1 μm) forms the insulation between the two metal layers. At this point, 6 μm × 6 μm vias are patterned in the insulation layer over the ends of the traces using an O_2 plasma RIE. A second step-coverage optimized liftoff process is used to define a second metal layer comprising electrodes and traces, while at the same time achieving electrical continuity between the underlying traces and the overlying electrodes. A final parylene coating approximately 7 μm thick forms the top insulation. The electrodes are exposed and the overall geometry of the implant is defined in a final set of O_2 reactive-ion etches using a thick photoresist etch mask. Finally, the arrays are peeled from the wafer in a water bath or released through removal of the sacrificial photoresist in acetone.

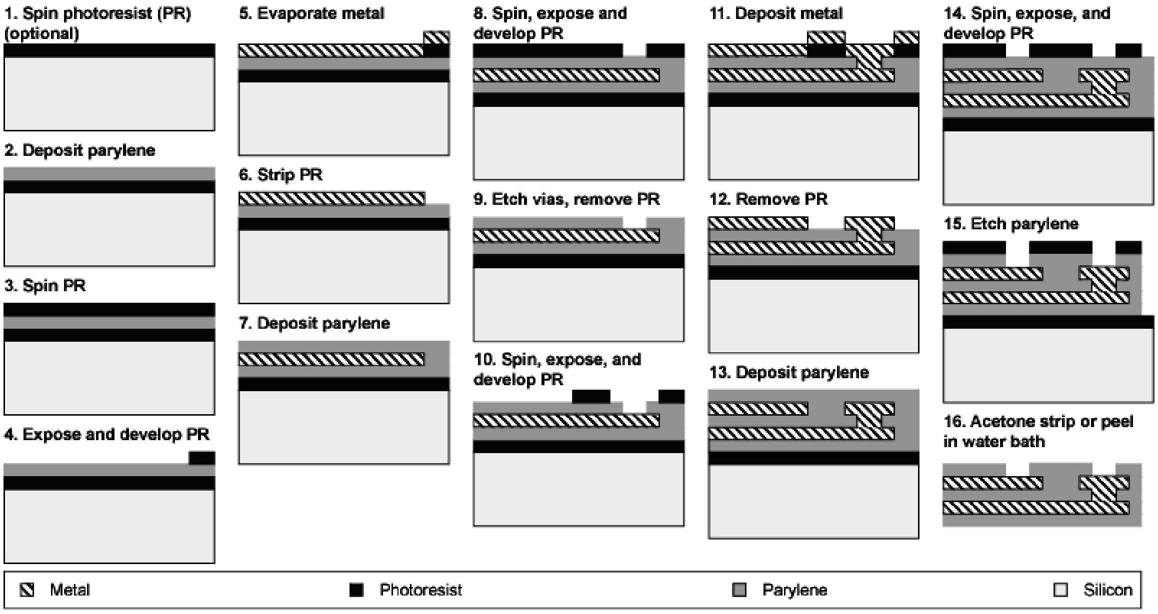

Figure 3-16. Fabrication process for parylene-based dual-metal-layer flexible MEAs.

The process depends on optimal step coverage of the parylene sidewall during evaporation, which is aided, in part, by the slightly isotropic nature of the O_2 plasma etch of parylene [109] as well as by the special design of the rotating wafer domes inside the e-beam evaporator, for which the angle of attack of the metal evaporant is adjusted for best coverage. This requirement conflicts marginally with those for successful metal liftoff, however, in this case, the liftoff technique is robust even under these step-coverage optimized conditions due to the choice of an LOR/positive photoresist compound layer.

3.3.4 Annealing and Heat Molding

Initial testing of such parylene-metal-parylene structures under accelerated-lifetime conditions in hot saline solution revealed a significant problem. Upon soaking, samples tended to develop interfacial delamination that was visible even under light microscopy. A matrix of different processes was done on wafers coated with parylene, followed by a subsequent parylene coating. Figure 3-17 shows such a parylene-parylene sandwich structure, where oxygen plasma roughening was performed on the surface of the first layer of parylene before the second parylene coating, after soaking for one day in 77 °C saline solution. As can be clearly seen, a significant amount of delamination at the interface has already occurred. We conjectured that if we placed a piece of the exact same sample into a vacuum oven and brought it to a high temperature, past the glass-transition temperature of parylene C (150 °C [110]) but below its melting point (290 °C) prior to soaking, that this problem would be obviated. One such sample, then, was “annealed” for two days at 200 °C in a vacuum oven with nitrogen backfill, at a total pressure of approximately 10 Torr. As shown in Figure 3-18, this was indeed a good hypothesis. No interfacial delamination could be detected, even after months of soaking at this high temperature. In fact, under these accelerated-lifetime passive soak test conditions, this annealing process has been shown to increase the extrapolated MTTF of devices to 20 years or more [81]. The configuration of the annealing chamber is diagrammed in Figure 3-19.

Figure 3-17. Unannealed parylene C sandwich structure after short accelerated-lifetime saline soak test. Interfacial delamination is clearly discernable.

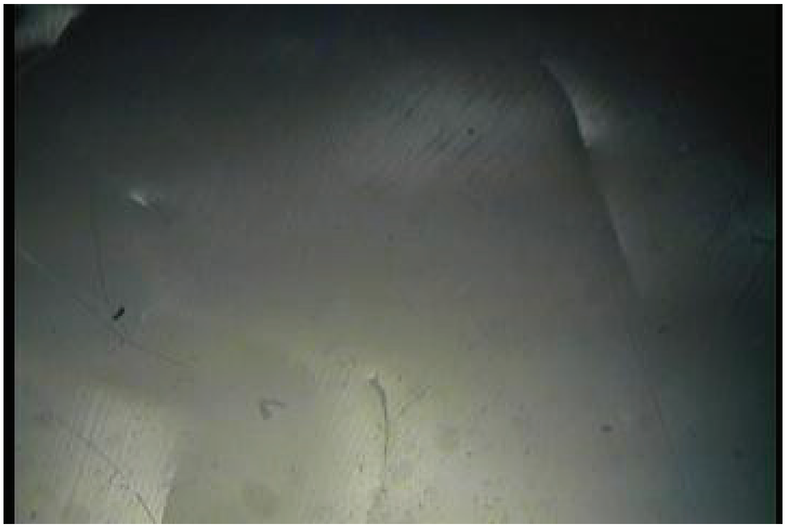

Figure 3-18. Annealed parylene C sandwich structure after long accelerated-lifetime saline soak test. No interfacial delamination can be seen.

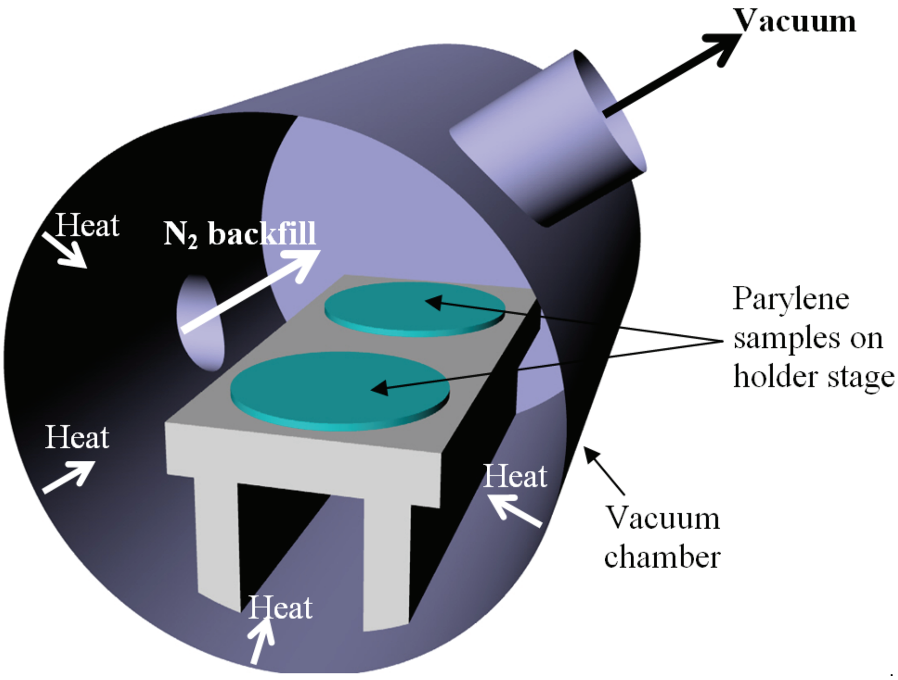

Figure 3-19. Annealing chamber for achieving strong parylene-parylene adhesion.

The mechanism by which this process strengthens parylene-parylene adhesion is not entirely known. First, it is believed that, when parylene is deposited and the vacuum is broken to remove the sample, some important things happen. This exposure to atmosphere inhibits all possibilities for polymerization to continue on the strands of parylene molecules already deposited on the sample. The sample has, in essence, a discrete parylene layer that will not chemically react with additional parylene that is subsequently deposited on the surface, so the interface between layers is not homogenous with the material in the two layers individually. In addition, it is possible that any unpyrolyzed parylene or contaminants in the parylene are now stuck in the sample, or on the surface of the sample, and cannot be removed. The annealing process, then, can work in a number of ways. Because it is at a temperature beyond the glass-transition temperature, it can serve to reflow the material at this interface, so that polymers of parylene from one layer can interweave with parylene polymers from the other layer (not cross-linking, per se, as no chemical reaction is taking place). Is it is possible, but unlikely, that any activated ends of the polymers may have also gain sufficient activation energy in the form of thermal energy to join with others from the other layer (a true chemical reaction). Finally, this annealing process might serve to move any contaminants out of this interfacial region. All of these possibilities serve to make this interface much more homogeneous with the bulk material in the two layers individually. Any water or chemicals passing through the parylene (parylene is not truly hermetic, despite its strong water-barrier properties) will no longer get trapped at this interface, but pass through it similarly to the rest of the material. Thus, chemical trapping at this interface is reduced. One final possibility, for which we now have some preliminary evidence, is that the parylene layers themselves become slightly modified. It is well known that polymers tend to increase their density when heated and then recooled, especially if the excursion is beyond any glass transition temperature of the material. We have done experiments that suggest that the density of parylene increases similarly. The layers themselves, then, may serve as stronger barriers to chemical and water flow because of the closer spacing of the polymer strands. Thus, it is likely that this increase in density of the parylene layers may serve as another reason, likely in combination with the others, that interfacial delamination is not observed after annealing. Remarkably, as we have shown, even if processes are performed that tend to increase this delamination problem, such as O_2 plasma roughening (which makes surfaces more hydrophilic), photoresist spinning and processing, and various chemical treatments, when compared with depositing two parylene layers in quick succession, this process can convert these poorly behaving samples into well-behaving ones in a very short time. Although a full matrix of tests has been run, it seems that this initial guess of two days at 200 °C may actually be optimal. Our implants, then, are routinely annealed for two days at 200 °C in the annealing chamber depicted in Figure 3-19 to optimize parylene-parylene adhesion.

An important aspect of these parylene arrays is that they are heat moldable due to this glass transition. If the arrays are contoured and confined to a geometry of interest for the target application during the annealing process, we have discovered that this conformation will be maintained throughout sterilization, implantation, and follow-up. The retinal arrays are shaped using a custom 6061 aluminum mold comprising a recessed concave region and a mating stainless steel sphere that approximates the curvature of the canine retina (diameter ~22 mm). During annealing, the array region is sandwiched between the sphere and the mating surface, while the cable is pressed flat against the aluminum plateau. We initially began with a structure where the concave region was exactly half the diameter of the sphere (Figure 3-20). Unfortunately, during heating and associated thermal expansion, the sphere would become cemented in place, and the cable region would be cut by the lip of the cavity. To solve this, we cut the curved molding region in half so that the majority of the expansion of the ball would occur above the mold, and smoothed the edge of the lip. All following molding attempts were successful in molding the array without cutting the cable or cementing the sphere in place. It is important to note that, during annealing, parylene will get stuck to oxide surfaces, such as those of glass slides. It is important to use a material such as metal or Teflon® to enable array release after the annealing process. A photograph of the final mold used is shown in Figure 3-21.

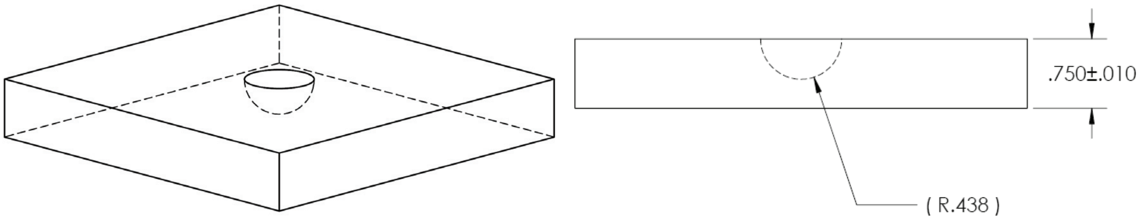

Figure 3-20. Initial design of heat-forming mold for chronic canine parylene retinal implants. Units are in inches.

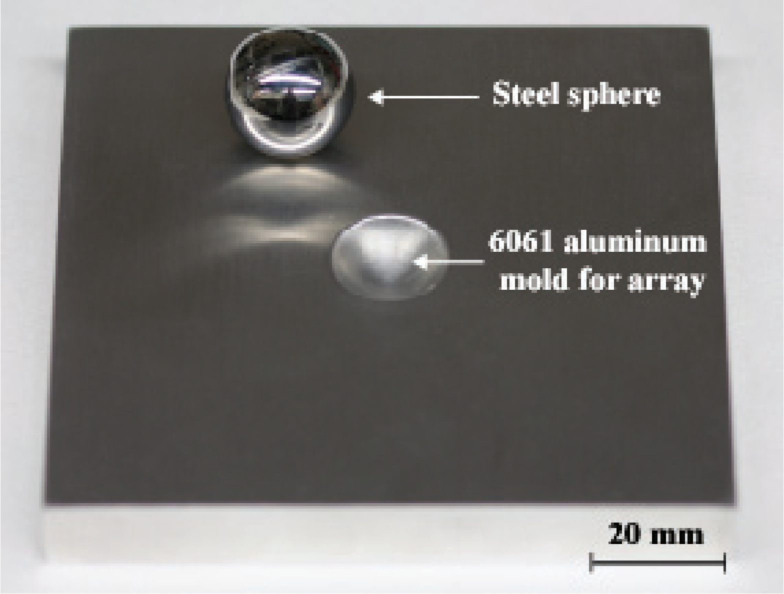

Figure 3-21. Custom heat-forming mold for chronic canine retinal implants.

3.3.5 Electroplating

As a possible mechanism for extending the longevity of chronically pulsed electrodes, we have chosen to investigate electroplated films of high surface-area platinum. Specially designed thin-film platinum electrode arrays, consisting of sixteen 75 μm and 150 μm diameter electrodes of 3000 μm center-to-center spacing, were fabricated according to the single-layer process. Initial experiments were performed on these arrays to determine material morphologies after plating at different potentials in an aqueous ammonium hexachloroplatinate solution according to Whalen et al. [111]. Subsequently, arrays were immersed in the solution in a specialized jig and six were plated at a plating potential of -0.6 V (vs. an Ag/AgCl reference electrode) for 1.5 hours. The others remained unplated. Electrochemical tests were performed to evaluate the efficacy of this plating step in extending electrode longevity under chronic pulsing.

3.4 Results and Discussion

3.4.1 16 × 16 Electrode Array

A single-layer square-grid electrode array, consisting of 256 Ti/Pt thin-film electrodes 125 μm in diameter in a 16 × 16 grid with connecting lines of 12 μm pitch fabricated in the manner of Figure 3-15 is shown in Figure 3-22. An SEM highlighting the typical electrode morphology in such structures is shown in Figure 3-23, with magnified views of a typical thin-film platinum surface given in Figure 3-24. As can be seen, the parylene covering the electrode has been completely removed, whereas the incoming trace remains conformally coated with the material.

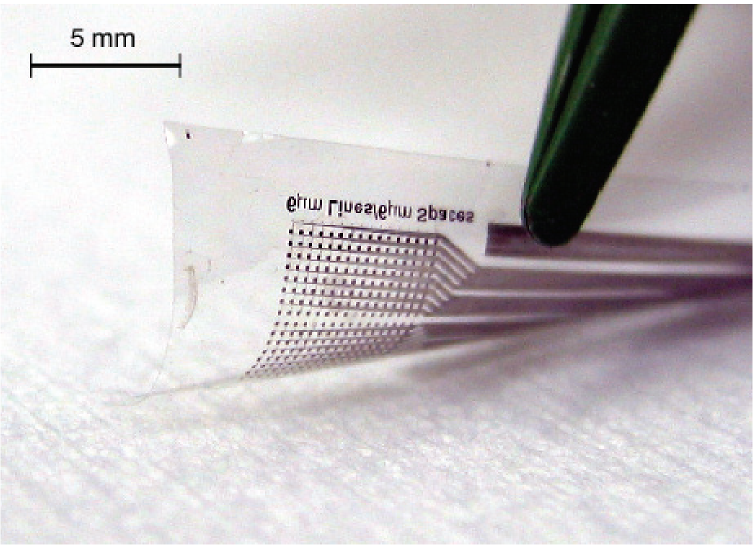

Figure 3-22. Photograph of Ti/Pt electrode array of 256 electrodes and lines of 12 μm pitch.

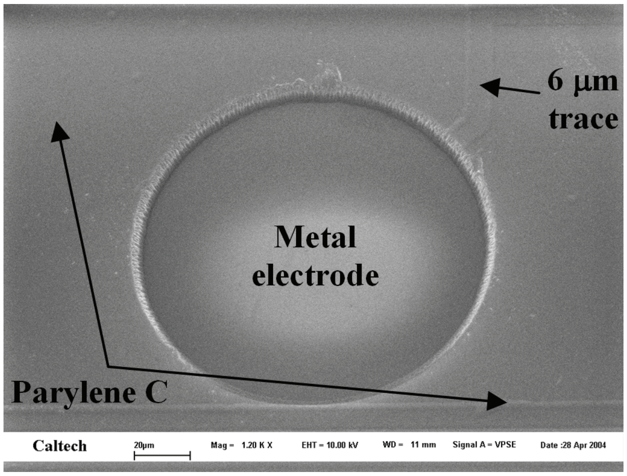

Figure 3-23. SEM of electrode morphology showing parylene C insulation surrounding exposed metal electrode.

Also fabricated in this manner were various electrodes for performing standard electrochemical measurements, such as CV and EIS (Figure 3-25). In Figure 3-26, we see a CV of one such 50 µm diameter electrode in 0.1 M PBS electrolyte, the first ever for one of these parylene-based electrodes. The jumps in the current are anomalous and correspond to an amplifier switching in the electronics. This CV shows the peaks expected for a platinum stimulating electrode when compared with those found in the literature [89].

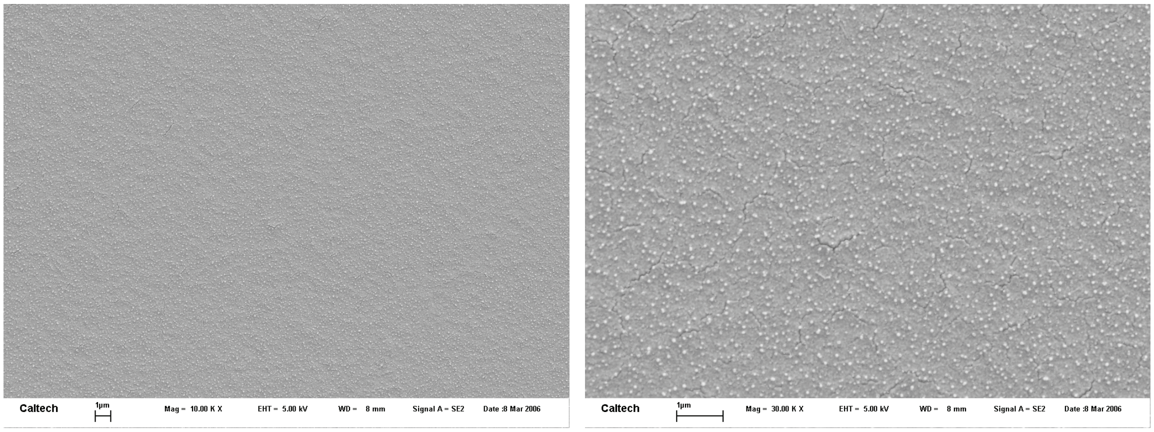

Figure 3-24. Magnified SEMs of thin-film platinum electrode.

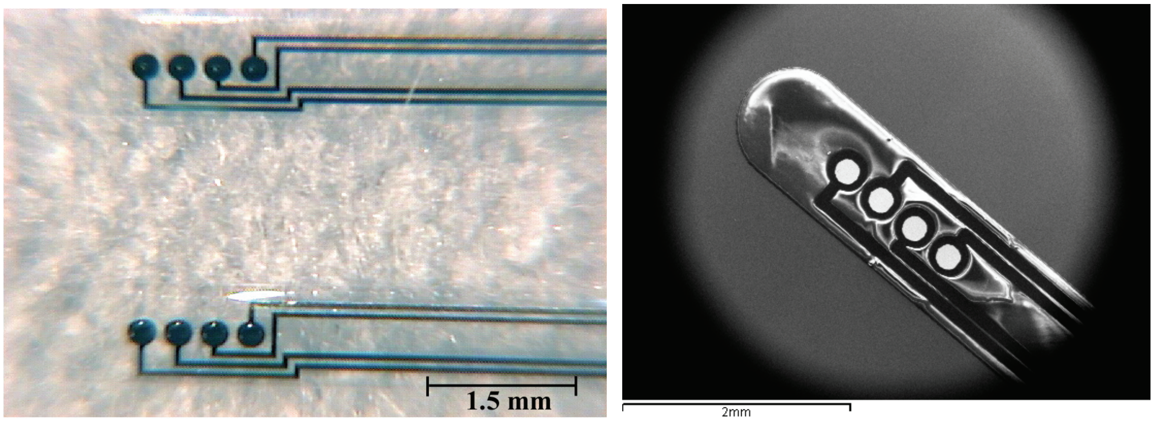

Figure 3-25. (left) 50 and 200 µm diameter test electrodes for electrochemical measurements and (right) SEM of electrode array depicting 200 µm diameter 5000 Å thick Pt electrodes.

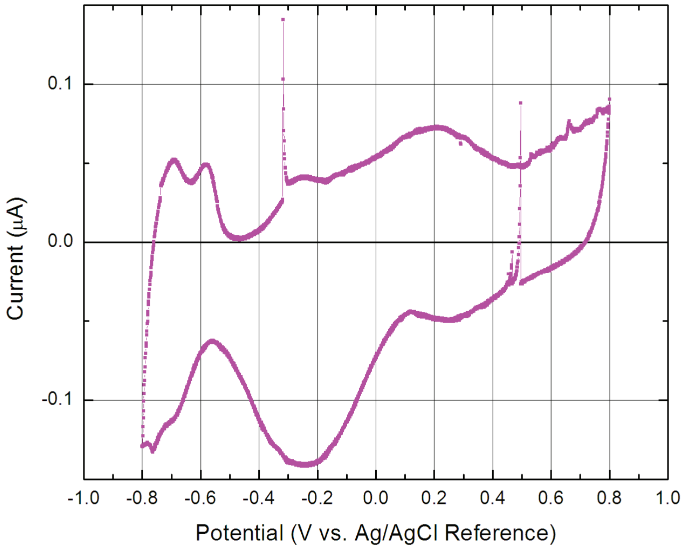

Figure 3-26. CV of 50 µm diameter test electrode (200 Å Ti / 2000 Å Pt) in 0.1 M PBS (50 mV/s sweep rate).

3.4.2 *In Vitro* Retinal Recording and Stimulation

Parylene C-based arrays of thin-film platinum electrodes, comprising four 200 µm diameter stimulating electrodes and 56 recording electrodes of 10 µm diameter were fabricated according to the single-metal-layer process on a glass substrate, as shown in Figure 3-27.

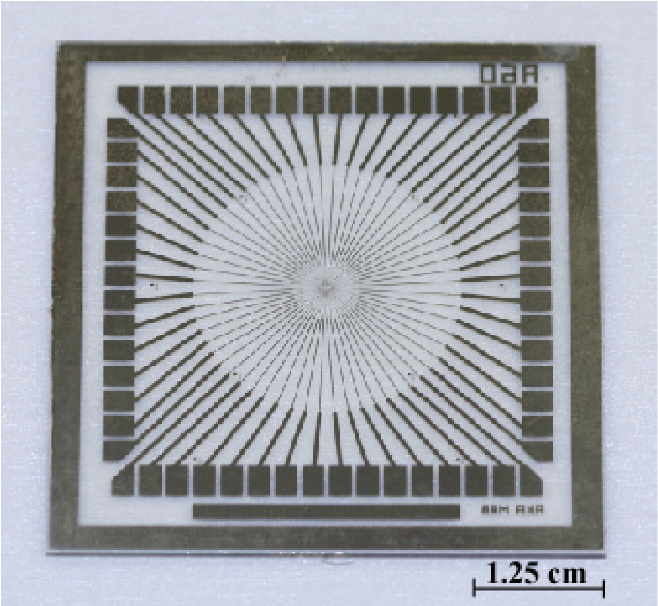

Figure 3-27. Fabricated *in vitro* parylene-based retinal stimulation array.

These were placed in a bicarbonate perfusate under a microscope and connected to a stimulus generator and preamplification board (Multi Channel Systems MCS GmbH, Reutlingen, Germany) [99]. As shown in Figure 3-28, a retina isolated from larval tiger salamander (*Ambystoma tigrinum*) was placed RGC side down on the array (to simulate epiretinal stimulation), and a remote platinum ground electrode was introduced to the bath.

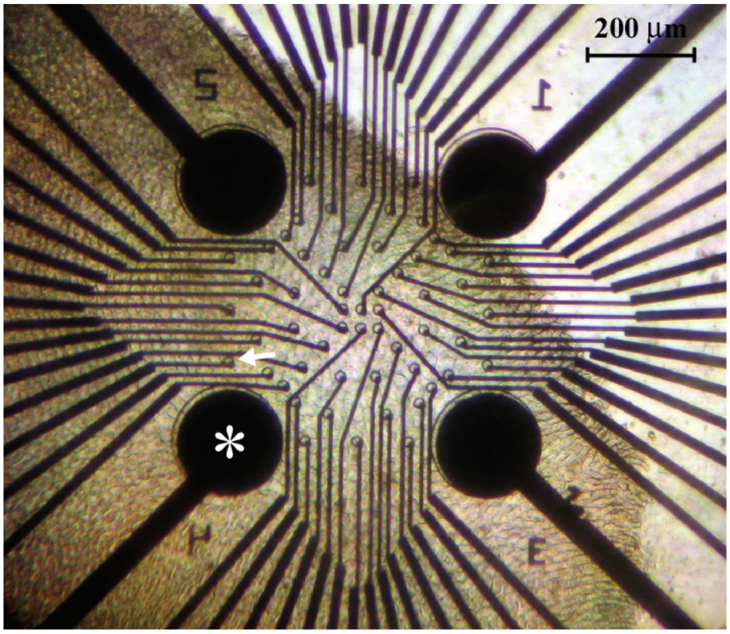

Figure 3-28. Isolated larval tiger salamander retina (darker region at left) overlying parylene-based platinum electrode array. Arrow indicates 10 μm diameter electrode used for recording traces in Figure 3-29 and Figure 3-30. Asterisk identifies 200 μm diameter stimulating electrode used to generate action potentials seen in Figure 3-30.

In order to assess retinal health, and for comparison with electrical stimulation results, a white light pulse 40 ms in duration was applied to the tissue. As shown in Figure 3-29, a voltage trace of the activity of the cells overlying one of the recording electrodes (electrode indicated with an arrow in Figure 3-28), a robust ON response was detected after the phototransduction delay, followed by the expected OFF response approximately 50 ms later. Subsequently, with the lights off, a 20 μA, 400 μs/phase, cathodic-first biphasic electrical pulse was applied between the stimulating electrode indicated with an asterisk in Figure 3-28 and the ground electrode. The voltage trace from the same recording electrode as above is shown in Figure 3-30. This stimulation was consistently repeatable over a 50 pulse train with a 400 ms inter-pulse interval, and other stimulating electrodes were also capable of "epiretinally" stimulating other cells in the retinal slice. As is clear from these results, the parylene-based platinum electrode was able to stimulate the tissue and elicit a response similar to the response generated from a light pulse in this intact retina. Given these results and the knowledge garnered from clinical trials with prototype arrays fabricated of other materials, it is not unreasonable to presume that our arrays will most likely be able to stimulate retinal tissue in other species, including human. To this end, the chronic biostability of implanted parylene-based arrays was also evaluated.

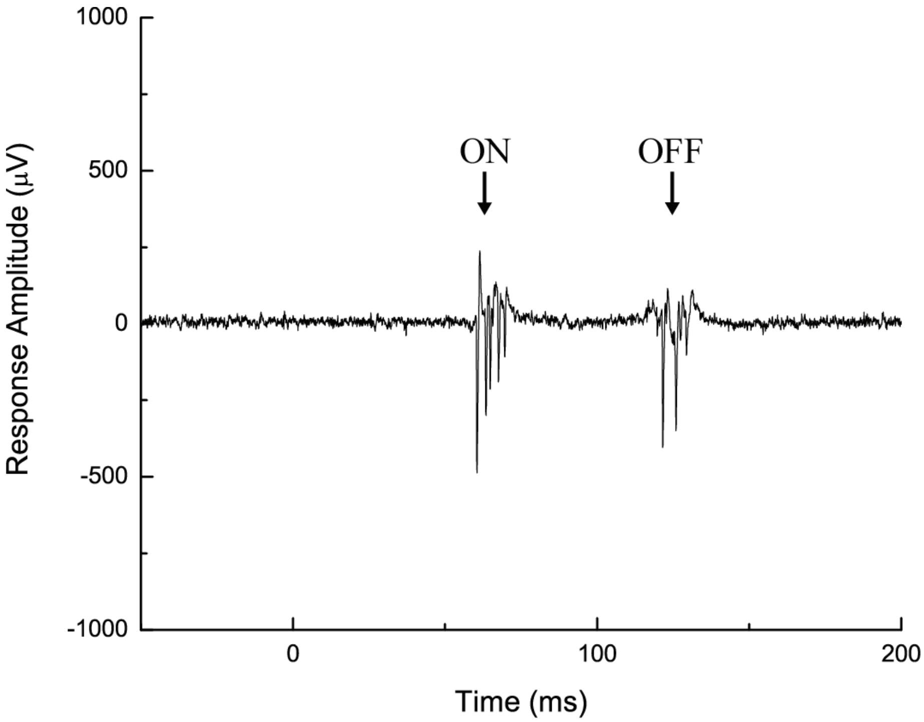

Figure 3-29. Recording of ON response followed by OFF response of cells overlying electrode denoted with an arrow in Figure 3-28 to a full-field white light stimulus of 40 ms duration. Pulse began at 0 ms on the abscissa, with delay until ON response due to phototransduction.

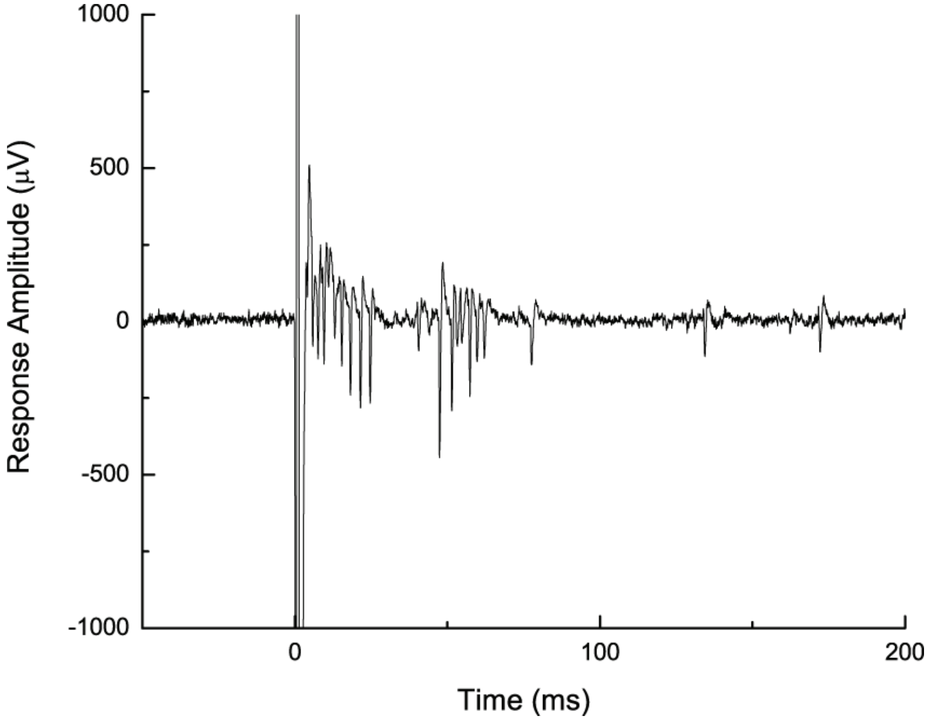

Figure 3-30. Typical recording of response of cells overlying same recording electrode as in Figure 3-29 to a 20 μA, 400 μs/phase, cathodic-first biphasic electrical pulse from "epiretinal" stimulating parylene-based platinum electrode denoted with an asterisk in Figure 3-28.

3.4.3 Chronic Retinal Implantation

Chronically implantable retinal electrode arrays comprising 1024 75 μm diameter electrodes arranged in a complex biomimetic pattern that closely mimics the density of ganglion cells in the human retina [112] were designed (the electrode density varied radially in a ratio matched to that of the RGCs), as shown at the left in Figure 3-31. These arrays (shown at right in Figure 3-31) were fabricated according to the dual-layer process, with 60 of the electrodes connected via two traces each to facilitate electrical conductivity verification. The strength of metal adhesion was verified using a Scotch tape test, which demonstrated that direct platinum evaporation is feasible without the

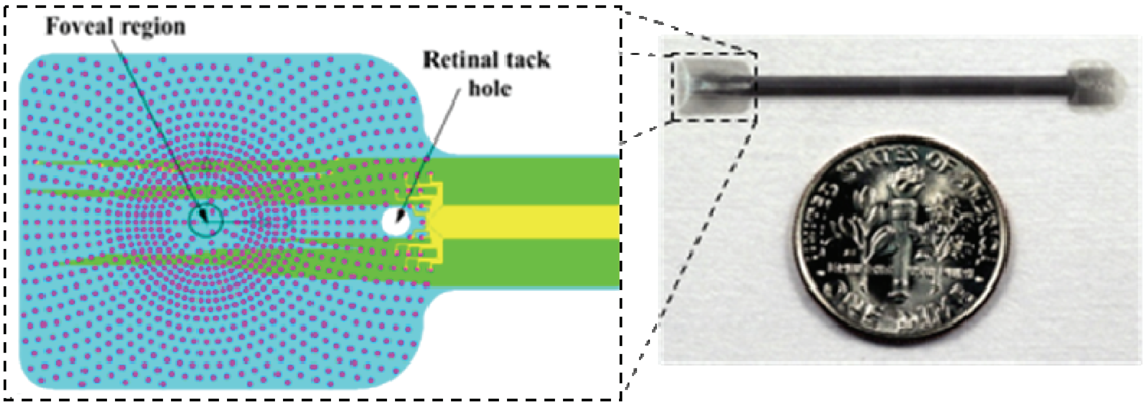

Figure 3-31. (left) Design of biomimetic dual-metal-layer retinal electrode array showing biomimetic arrangement of electrodes. (right) Fabricated biomimetic chronically implantable arrays with 60 of 1024 75 μm diameter electrodes connected through dual-layer process with U.S. dime for size comparison.

need for a titanium adhesion layer. Electrical testing demonstrated a typical line impedance of a contact-electrode-contact circuit to be approximately 5 kΩ, which included two 8 μm wide traces of 20 mm length, as well as two via step junctions connecting underlying traces to the overlying electrode. Two types of via and electrode configurations were tested. Some electrodes (electrode SEM given in Figure 3-32 (left)) had vias connecting to the underlying trace near the center of the electrode, hence enabling charge spreading from the center of the electrode. One possible drawback to this configuration is that the contact from trace to electrode over the sidewall is a potentially vulnerable point of the circuit during processing (e.g., subsequent RIE processes) and during pulsing in electrolyte because the metal may be thinner there. The other electrode configuration had vias located adjacent to the electrode (electrode SEM given in Figure 3-32 (right)), with the possible advantage that it would be protected during RIE and subsequent pulsing by the overlying conformal parylene layer. An SEM showing the morphology of a single central via is given in Figure 3-33. This clearly depicts the sidewall coverage responsible for the electrical contact between the first and the second metal layers. Profiles of each of these electrode configurations are shown in Figure 3-34 and Figure 3-35, with Figure 3-34 clearly depicting that the traces connected with central vias are recessed approximately 1 μm from the surface of the electrode. In both configurations, each via had an impedance of less than 12.5 Ω. The best final configuration has not yet been determined.

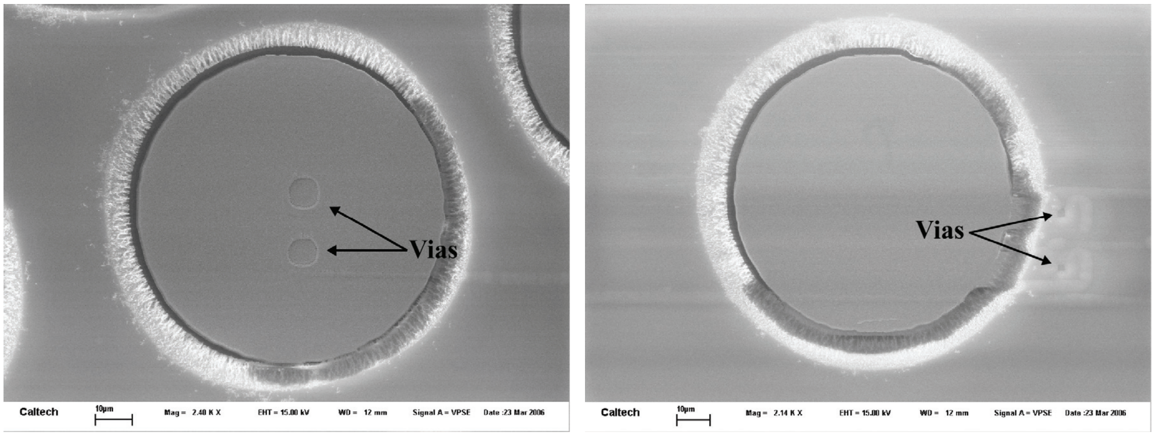

Figure 3-32. Two possible dual-layer electrode configurations. Electrode with central vias (left), and electrode with abutting vias (right).

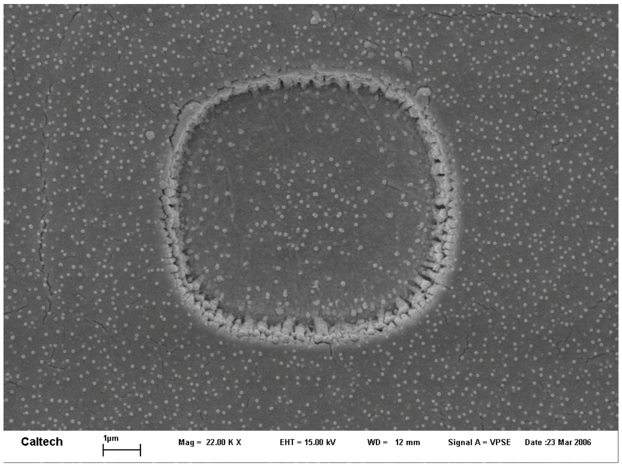

Figure 3-33. Magnified view of trace to electrode via showing sidewall coverage.

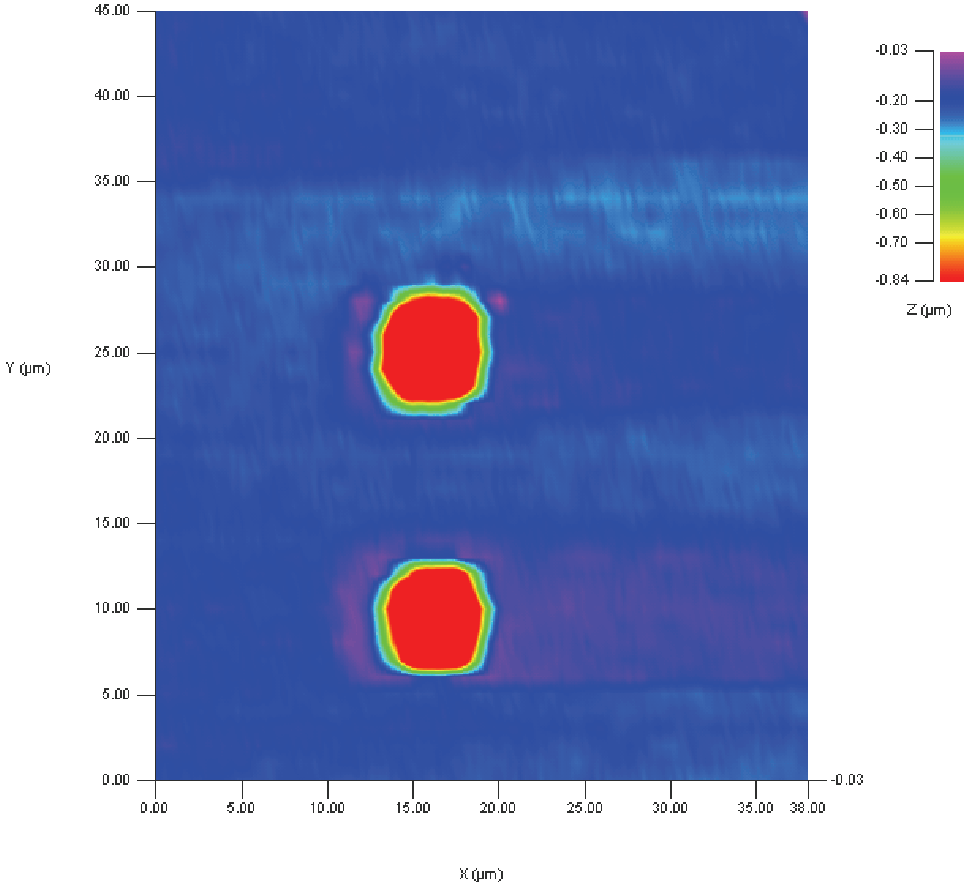

Figure 3-34. 3D profile of central vias showing traces are recessed ~1 µm from surface.

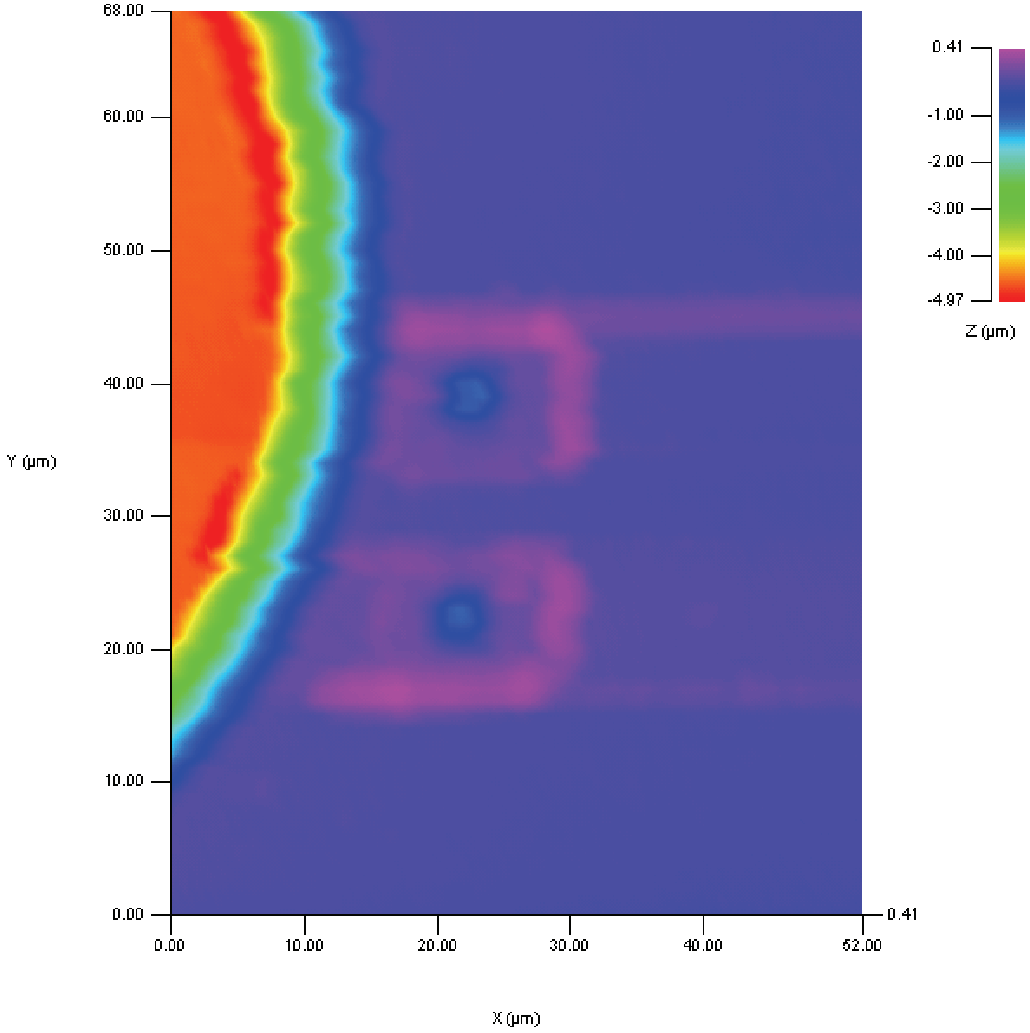

Figure 3-35. 3D profile of conformally coated abutting vias.

The arrays were successfully molded to the approximate curvature of the canine retina (Figure 3-36 (top)) using the custom mold, and sterilized using ethylene oxide gas. Two biomimetic arrays were implanted in the right eye of two canines through a 5 mm pars plana incision after vitrectomy, and were affixed to the retina (Figure 3-36 (bottom)) using a retinal tack modified by the addition of a PDMS washer (to account for the thin nature of the parylene arrays).

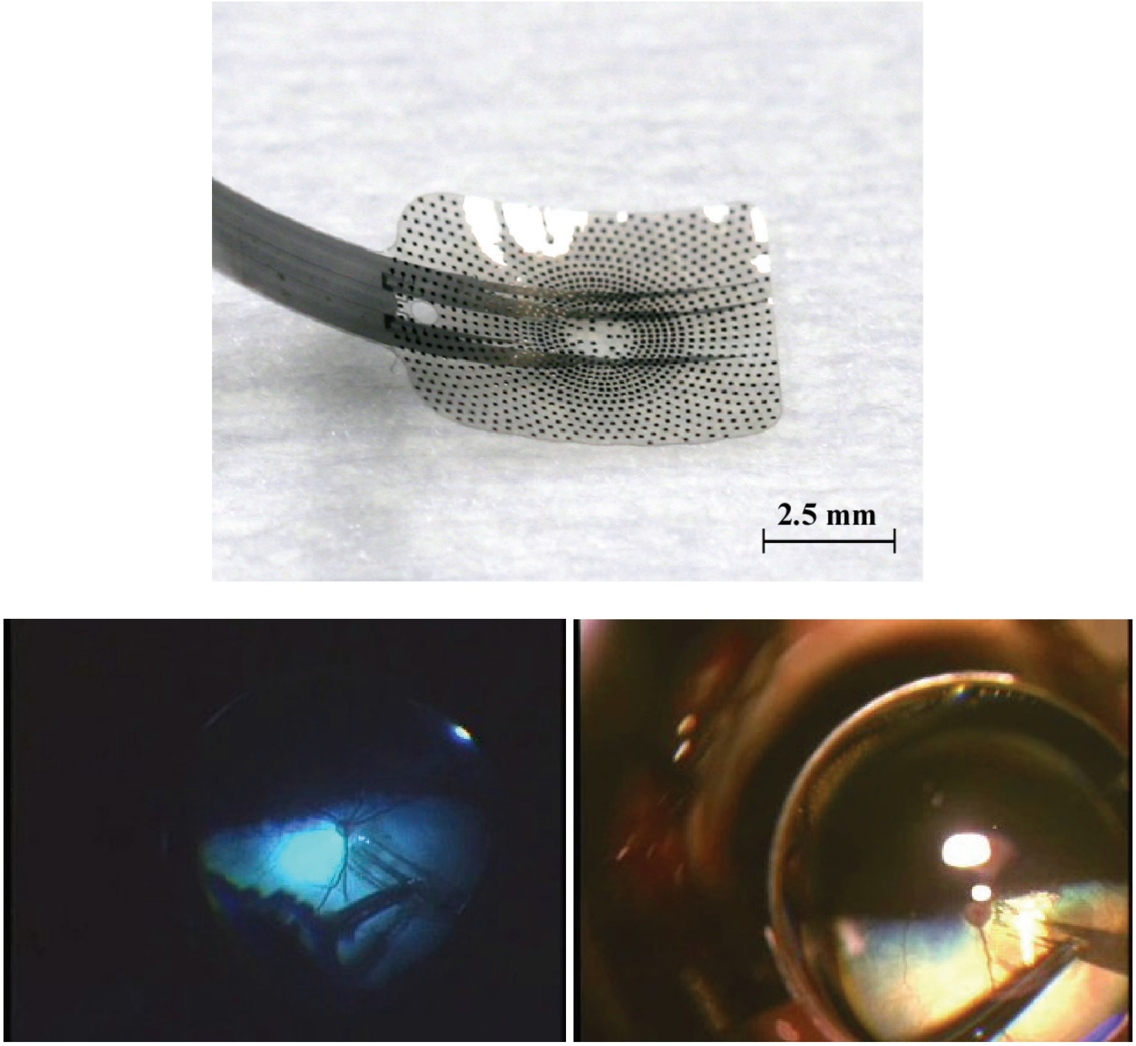

Figure 3-36. Heat-molded and annealed retinal electrode array with retained spherical curvature (top), and intraoperative photographs of tacking in each canine (bottom).

Follow-up in both animals was conducted for six months using fundus photography, fluorescein angiography (FA), in which blood is fluorescently stained to assess vessel perfusion in the retina, and optical coherence tomography (OCT), an interferometric technique that enables cross-sectional imaging of the retina. Fundus photography and FAs of both animals, examples of which are shown in Figure 3-37, consistently demonstrated that vessel filling underneath the array was normal. Obstruction and vessel leakage would have been visualized if the array were placing excessive pressure on the retina. In addition, OCT demonstrated that the electrodes were consistently less than 50 μm away from the ganglion cell layer in both animals (typical OCTs of both animals are shown in Figure 3-38), an outcome that theoretically would afford excellent electrical coupling between the electrodes and the electrically excitable cells of the retina. It is important to note that in the OCT of the second canine, the scan

Canine 1

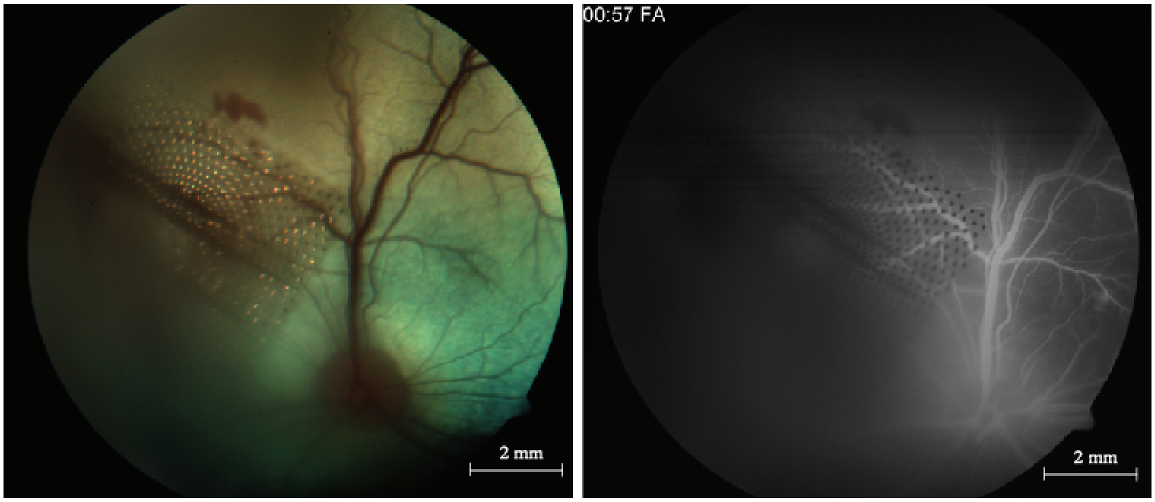

Canine 2

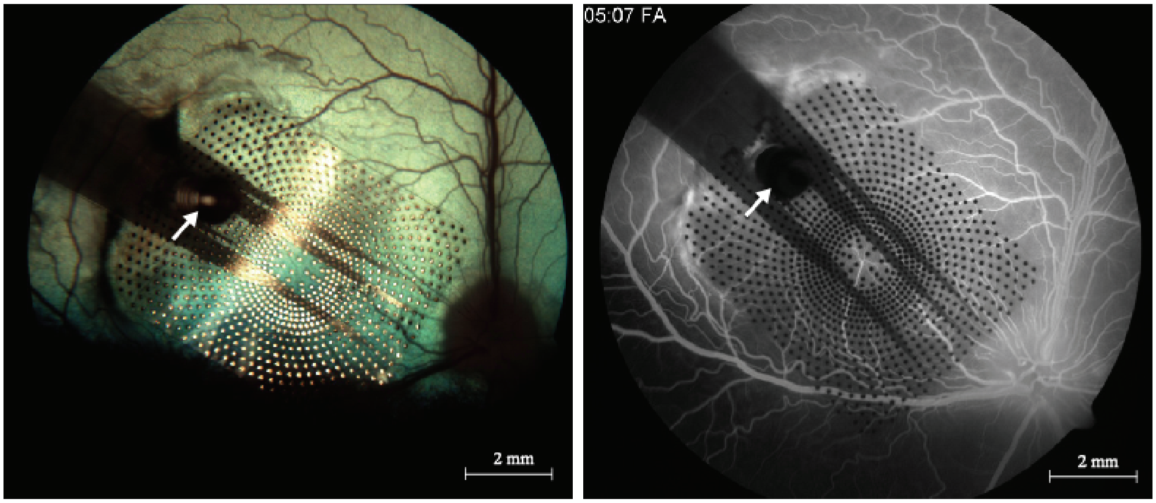

Figure 3-37. Fundus photographs (left) showing parylene MEAs tacked to the right retina of both animals and FAs (right) showing normal vessel perfusion under the arrays. Arrows point to retinal tacks.

was taken along a segment furthest from the tack site, where one might expect the least proximity. Even at this location, this array remained in very close apposition throughout the six-month implantation. Post-enucleation histology has since confirmed the excellent biostability seen during follow-up.

The dual-metal-layer process is wholly enabled by the use of parylene as an insulating layer. The low dielectric constant of parylene (~3.1 at 1 kHz [72]) enables this layer to be very thin while still minimizing capacitive crosstalk between overlapping and adjacent metal lines. The vapor-deposition process for parylene ensures that this layer can

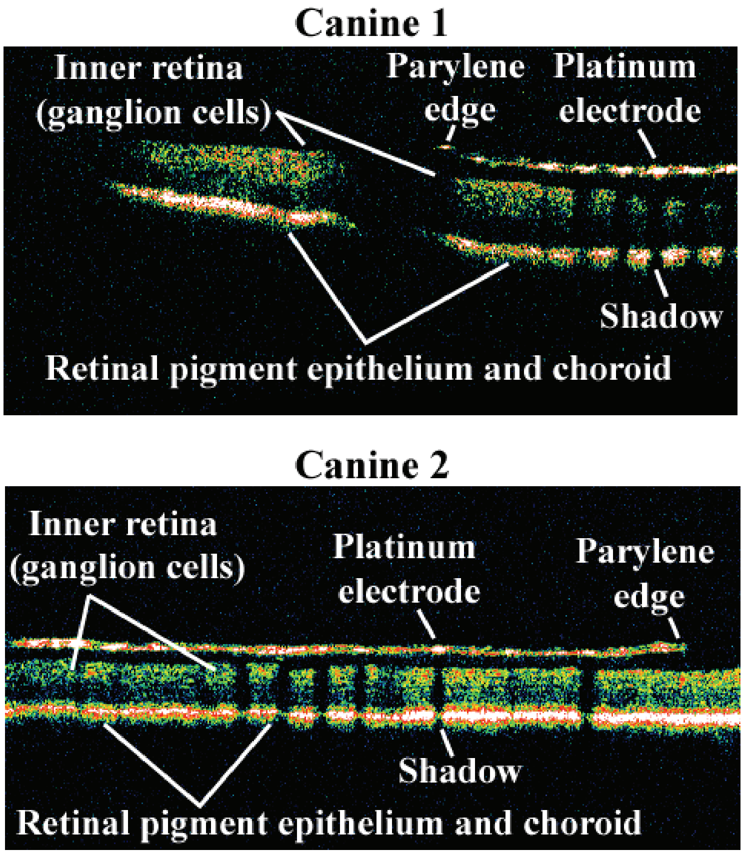

Figure 3-38. OCTs of both animals showing very close apposition (<50 μm) of the arrays to the RGC layer.

be very thin while still being pinhole free, where a spin-on coating, on the other hand, would prove problematic. As was briefly mentioned previously, the dual-layer process proffers considerable advantages over the more traditional single-layer approach. Design of single-layer electrode arrays is usually hindered by the need to route traces amongst the electrodes. This tends to cause crowding of traces and electrodes into groups, an organization that may not be optimal for stimulating the tissue of interest. In addition, this has a propensity to constrain the geometric area of the electrodes in the MEAs to smaller sizes, and thus reduces the number of electrodes possible in a given area. The dual-layer process obviates these problems by enabling traces to pass under overlying electrodes without making contact to them, having the effect of both relaxing the constraints on electrode size and number and enabling more complex electrode organization (such as the biomimetic one presented in this work). Although the arrays fabricated here had just 60 electrodes of connectivity with 120 traces total, this was without making full use of both layers for wire routing and connection of electrodes. In order to not make traces unnecessarily narrow and of too high impedance, we believe an extension of this process to three or more metal layers will be necessary to achieve 1024 electrodes of total connectivity. Indeed, this fabrication process is easily extendable to create such structures through addition of extra layers of parylene and metal. Given the encouraging biostability results presented here and the ability of these arrays to stimulate retinal tissue, future studies will include chronic stimulation from implanted parylene-based arrays in an animal model.

3.4.4 Thin-Film vs. Electroplated Platinum

If pulsed at close to the electrochemical safety limits for platinum (typically considered to be ~0.35 mC/cm^2 [113]), thin-film electrode arrays of platinum will invariably fail after some time. Shown in Figure 3-39 are SEM micrographs of electrodes that have undergone failure. The top image is an overview of a 1 X 4 electrode array, with the two images on the bottom showing electrodes at different stages of failure. There are two possible reasons for this type of failure. The first is corrosion of the overlying platinum under chronic pulsing, a likely possibility when pulsing at or close to the electrochemical safety limit [34]. The second is delamination of the metal layer in contact with the parylene from the surface. We have seen from processing that the titanium "adhesion" layer typically used when platinum is deposited on silicon or oxide is, in fact, unnecessary to achieve good mechanical adhesion to parylene (see Section 3.4.3). We hypothesize that this is because the high temperature of the platinum evaporant enables it to "melt" itself into the top layer of parylene, embedding the platinum atoms into the top surface of the parylene. From our preliminary evidence, we also believe that this titanium layer is also detrimental to adhesion under pulsing. In the two bottom images of Figure 3-39, it seems that a crack may have developed in the electrode surface (perhaps through some sort of focal corrosion mechanism), but that delamination of the electrode is likely to be the main mechanism of failure (SEM at left shows crack, SEM at right shows that the electrode has peeled from the parylene surface). In Figure 3-40, we see a magnified view of this crack.

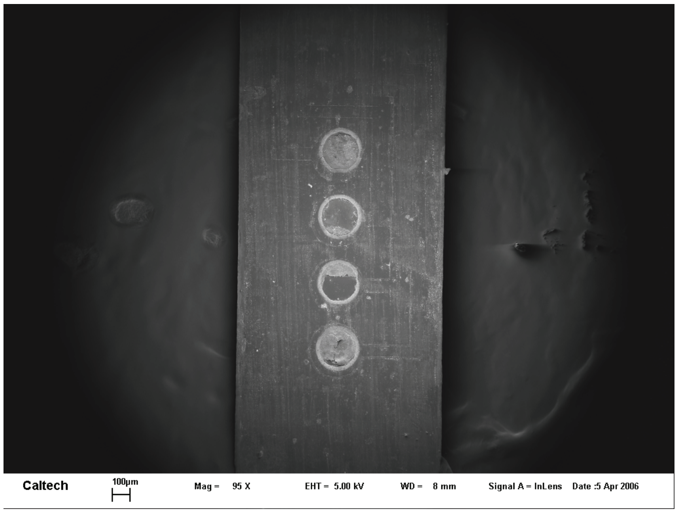

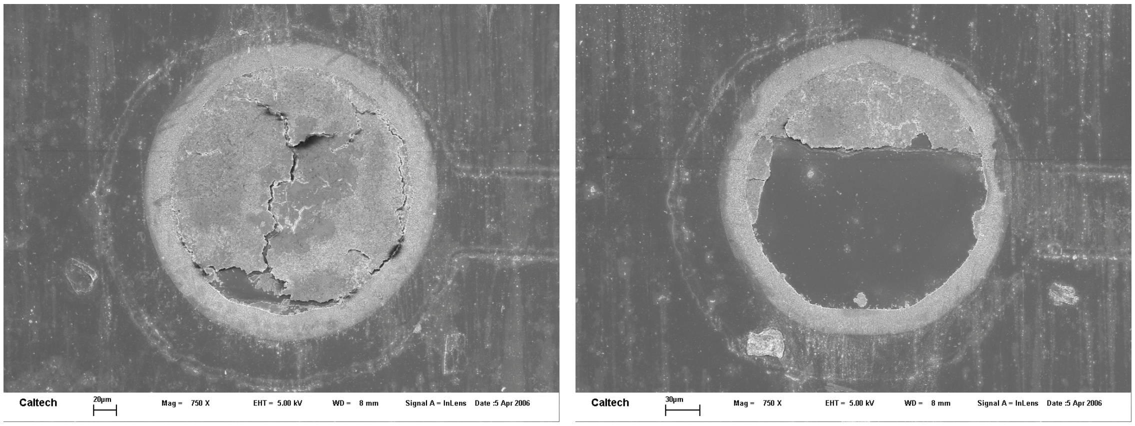

Figure 3-39. SEM micrographs of thin-film platinum electrodes after failure. (top) Overview of 1 X 4 array. (bottom) Magnified views of failed electrodes.

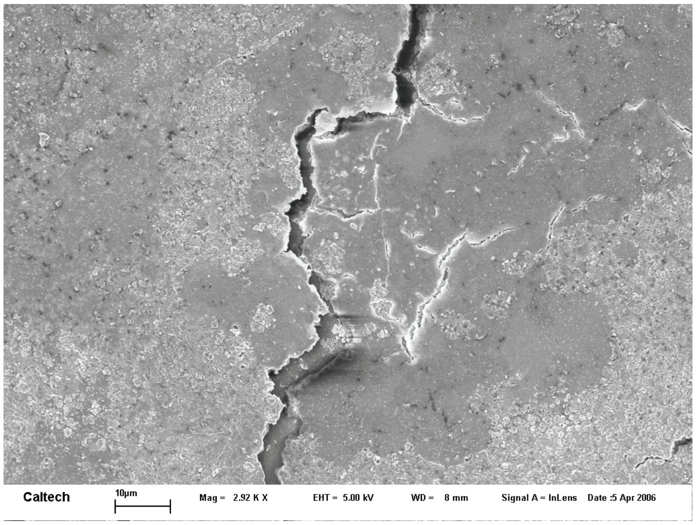

Figure 3-40. SEM showing magnified view of crack in electrode surface.

We aim to allay this problem through plating high surface-area platinum on the electrode surface. This would serve to increase the real surface area for charge transfer from an electrode of a defined geometric area. By doing this, the voltage necessary to inject the same amount of charge would be significantly lowered, likely below any levels necessary for corrosion to occur. In order to correctly test this hypothesis, the single-metal-layer electrode arrays in Figure 3-41 were fabricated. Initial plating tests were performed in a specially designed jig (Figure 3-42), and CVs as well as SEM micrographs were taken to assess electrode morphology.

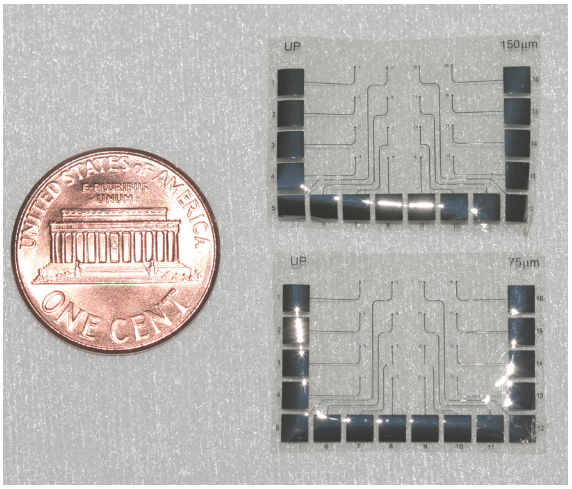

Figure 3-41. Fabricated thin film electroplating test arrays with 150 μm and 75 μm diameter electrodes.

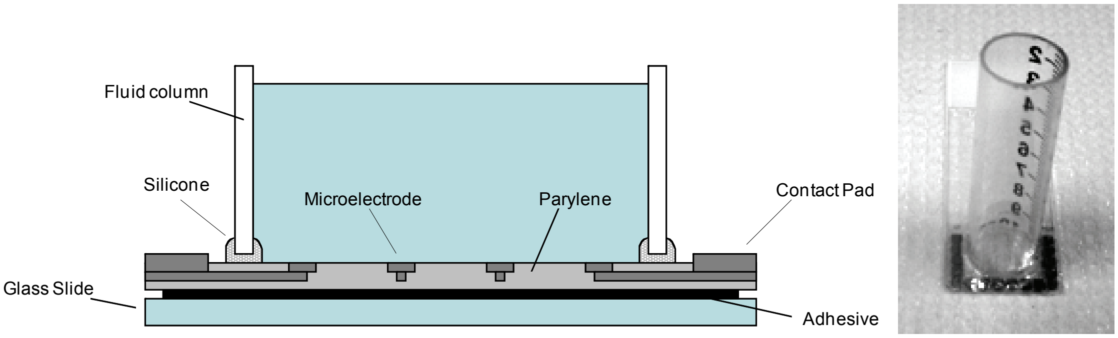

Figure 3-42. Jig for electrode platinization experiments. Courtesy of Dr. Jack Whalen.

The electrode morphologies of a typical array of 16 electrodes plated at different potentials are shown in Figure 3-43. Note that the 4 corner electrodes (1, 4, 13, and 16) were not plated. Magnified views of some of the possible morphologies attainable via this mechanism are shown in Figure 3-44. These micrographs show morphologies that likely correspond to a drastically increased surface area. In order to confirm this, CVs in O_2-free H_2SO_4 were taken of the electrodes before and after platinization. According to [114], "real" electrode surface area can be adequately estimated by integration of the area over the hydrogen adsorption peak (HP in Figure 2-15), or likewise the area under the hydrogen desorption peak (HO in Figure 2-15). The two CVs in Figure 3-45 show that

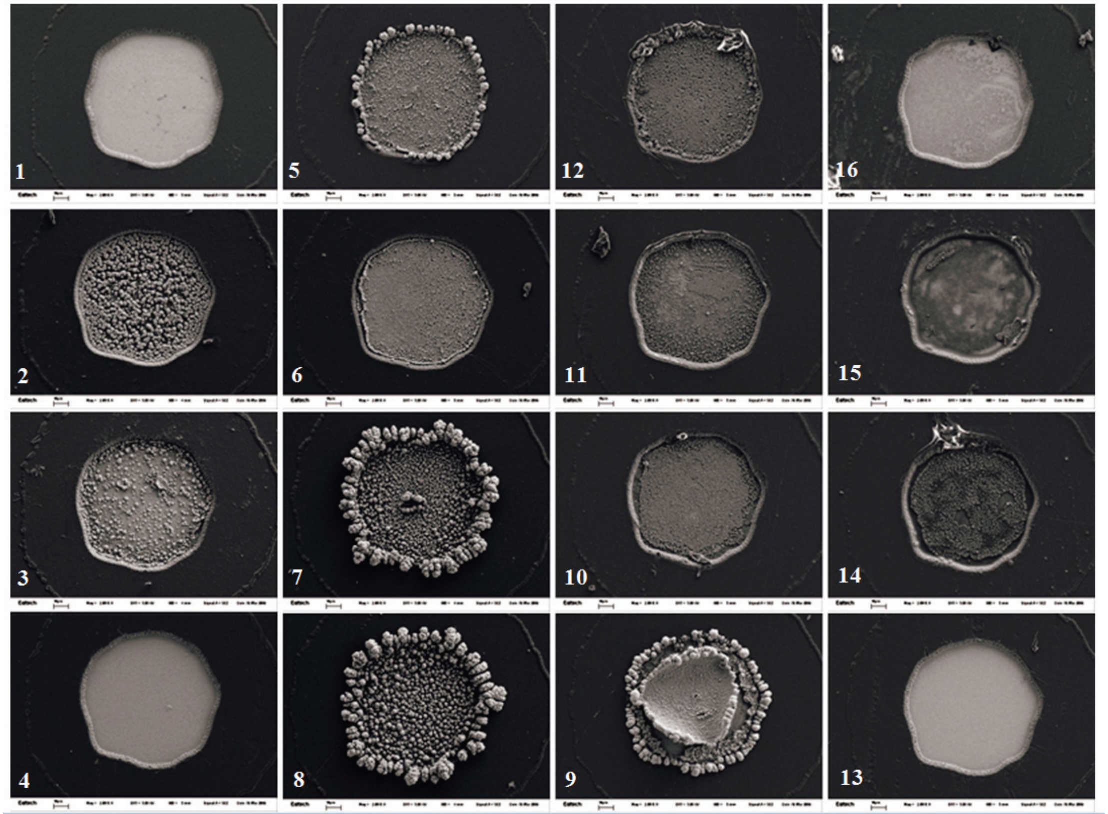

Figure 3-43. SEM of each of the electrodes on a typical 16-electrode array after platinization.

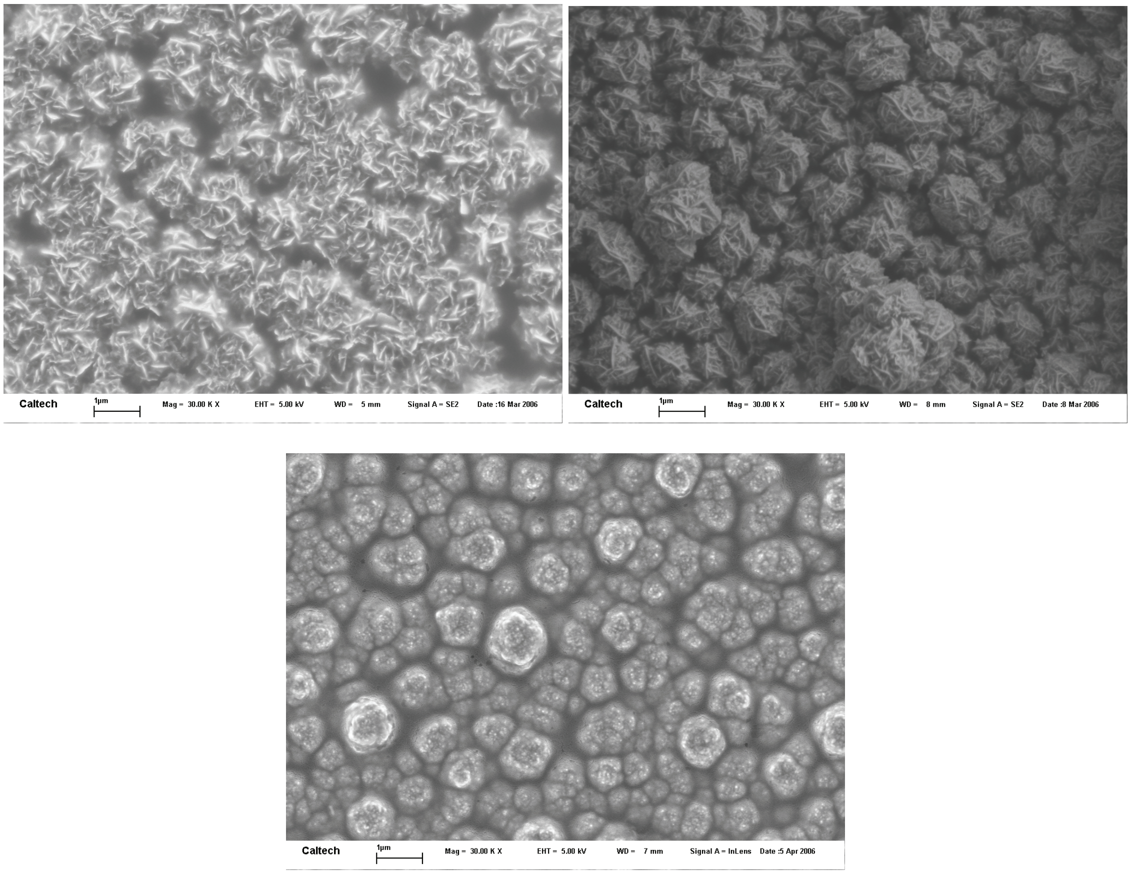

Figure 3-44. Magnified views of possible surface morphologies after platinization.

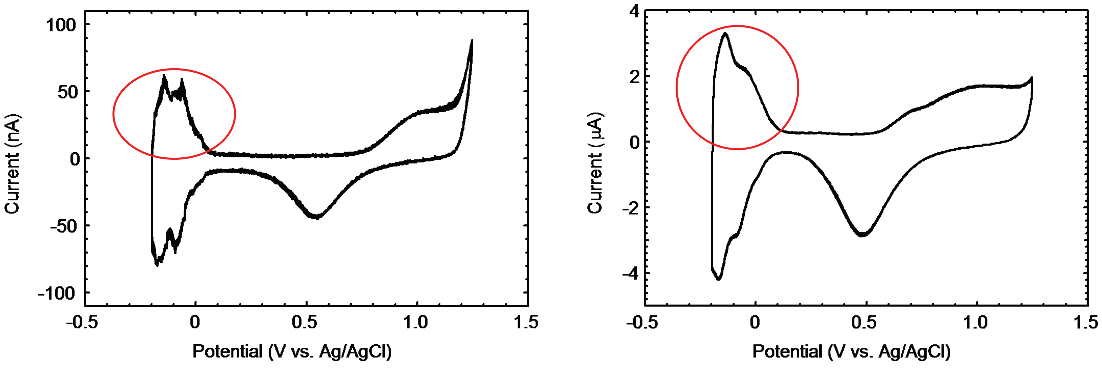

Figure 3-45. CVs showing more than 40-fold increase in electrode surface area from before plating (left) and after plating (right). The surface area is estimated by integrating the area under the peaks circled in red. Note change in scale of the ordinate. Scan rate: 100 mV/s. Electrolyte: O_2-free H_2SO_4 (N_2-bubbled).

there was a more than 40-fold increase in surface area after platinization when compared with the pre-plated surface area (note the change in scale of the ordinate from nA to μA). This was the maximal surface area increase noted, and was from the film plated at -0.6 V. From this, it was decided to use -0.6 V as the plating potential for subsequent experiments.

The ability of the electroplating process to extend electrode longevity was evaluated by chronically pulsing single-layer thin-film and electrodes platinum-plated at -0.6 V in PBS. CVs were performed in 250 mM aqueous sulphuric acid prior to plating and periodically during pulsing to estimate electrode surface area and overall electrode health. In addition, voltage responses to the current pulses were recorded and EIS was performed regularly. The plated and unplated electrodes were pulsed continuously for 50 days, or until failure occurred, at 100 Hz with a 60 μA (~0.34 mC/cm^2 of geometric electrode area) biphasic cathodic-first current pulse with 1 ms per phase and a 100 μs inter-phase delay.

The estimated surface area of the electrodes increased approximately 40 to 50 times between before and after plating, in accordance with the other preliminary work. Under pulsing, the voltage responses of both plated and unplated electrodes remained stable for approximately 29 days, at which point the unplated electrodes showed signs of failure. Voltage responses for one such electrode on day 26, 29, and 31 are overlaid in Figure 3-46 (top), which documents the progression of failure. The plated electrodes, on the other hand, remained intact for much longer, most surviving more than 50 days, or 430 million pulses, at which point the testing goal was met and the test was stopped.

Overlaid voltage responses for one such electrode, showing the voltage responses at day 26, day 31, and day 50, are shown in Figure 3-46 (bottom).

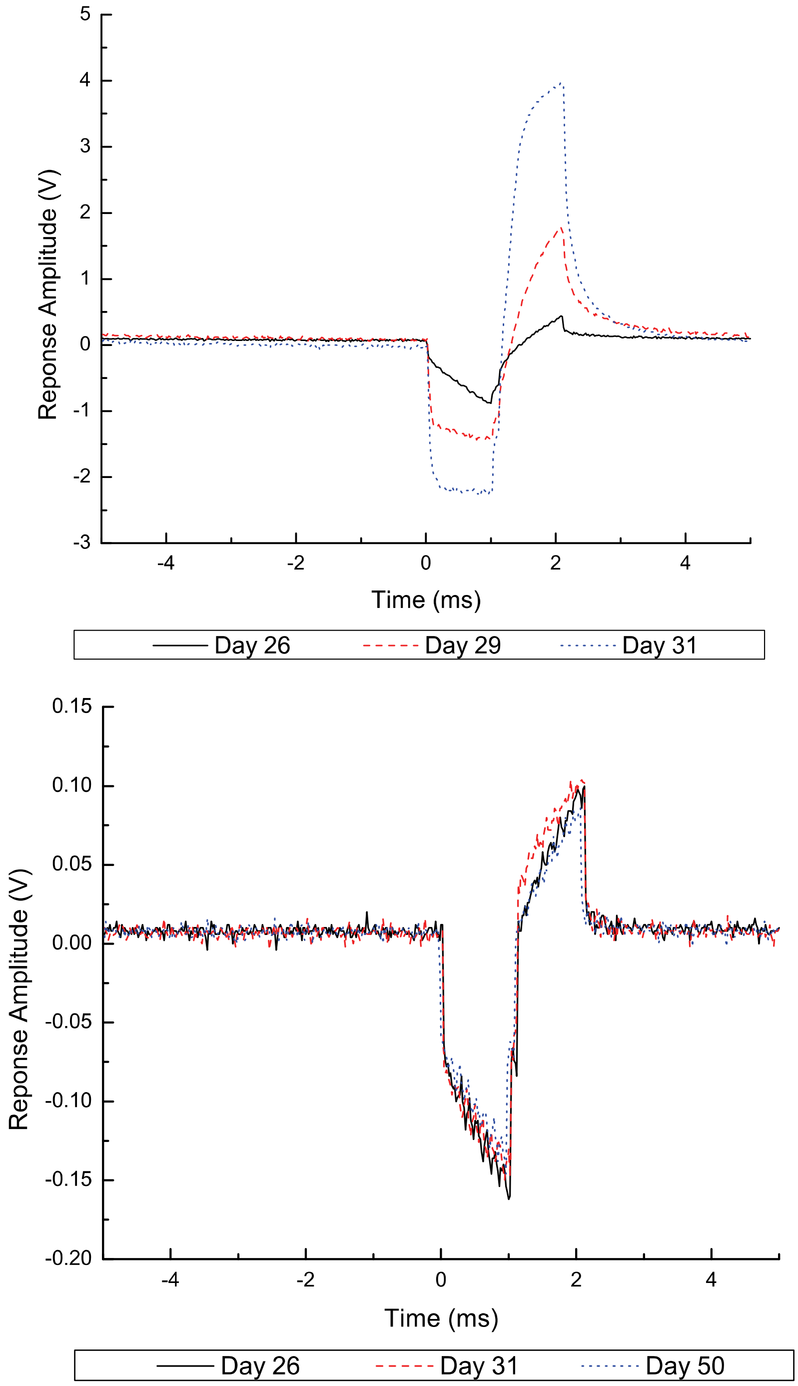

Figure 3-46. Voltage responses to a current pulse for (top) an unplated electrode, documenting the process of electrode failure, and (bottom) a plated electrode, showing steady responses throughout the 50 day test. Note response amplitudes for plated electrodes are far lower than those for the unplated electrode, as expected [34].

The electrochemical impedances at 1 kHz of a typical plated and unplated electrode are shown in Figure 3-47. A dramatic jump in impedance was observed for the unplated electrode at the time of failure, while the plated electrode demonstrated only minor variability in its lower impedance throughout the 430-million-pulse trial (most variability happened on the days that CVs were taken, as expected). These preliminary data corroborate the evidence that plating of the electrodes is beneficial to longevity, and suggest that high surface-area platinization of electrodes can have a dramatic effect on extending electrode life while lowering electrochemical impedance to charge delivery. Future work will include replication of these tests and chronic pulsing at high temperatures for longer times to further accelerate and assess the possible modes of failure.

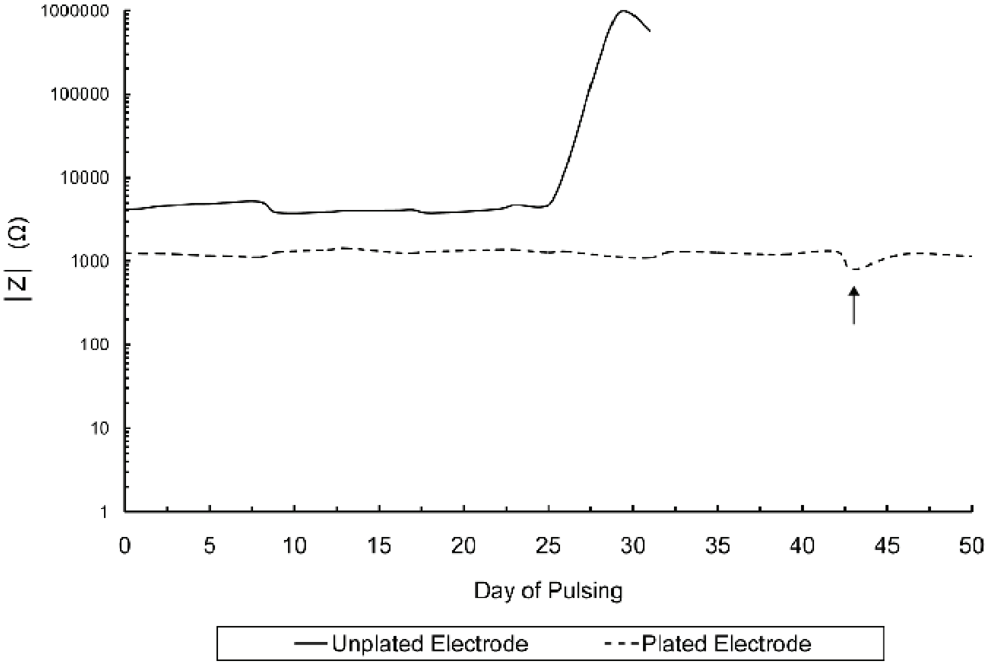

Figure 3-47. Magnitude of the electrochemical impedances at 1 kHz of an unplated and plated electrode over time. The unplated electrode showed a dramatic increase in impedance around day 30, at which time the test was stopped, whereas the plated electrode showed steady impedance through day 50. The arrow denotes a temporary dip in impedance due to CV scanning.

3.5 Iridium Electrode Arrays with Parylene HT

While the charge delivery capacity of platinum is sufficient for many applications, that of iridium is significantly higher [97], as it has four oxidation states as opposed to two [115]. In addition, iridium can be cycled to form an activated iridium oxide film (AIROF) [116] with even higher charge delivery capacity. Our investigation into the possibility of fabricating parylene-based flexible iridium electrode arrays spawned from such considerations. Usually, iridium or iridium oxide are deposited through sputtering [115, 117] or electroplating [118, 119], especially when they are applied to flexible substrates, a likely reason being that the high melting temperature of the material makes evaporation on polymers quite foreboding (thermal evaporation on thermally conductive substrates such as silicon is possible, however [120]).

Due to the higher thermal stability of parylene HT (long-term stability at 350 °C, intermittent exposures up to 450 °C [71] or 500 °C [121]), it was surmised that the material would be better suited to iridium array fabrication than would parylene C (the melting temperature of iridium is 2447 °C whereas that of platinum, for which a parylene C substrate works well, is 1772 °C [122]). Consequently, a minor modification of the single-metal-layer process was made to fabricate iridium electrode arrays (complete details in Appendix C). A thin parylene C layer (~2.4 μm) is deposited on the silicon wafer followed by a thicker layer of parylene HT (~5.7 μm) in a PDS2035 system (Specialty Coating Systems, Indianapolis, IN, USA). The parylene C layer facilitates fabrication and subsequent release, whereas the HT layer provides the necessary thermal stability. The dual photoresist layer is spun and patterned, and the iridium (~800 Å) is then e-beam evaporated on the wafer. After liftoff, a final parylene HT layer (~5.4 μm) is deposited and patterned as with the parylene C arrays, and the arrays are released in a water bath. This process was compared to an identical process performed using only parylene C structural layers.

Our comparison of iridium array fabrication on parylene C and fabrication on parylene HT yielded remarkable results. As can be seen in Figure 3-48, when e-beam evaporated and patterned on parylene C, the iridium film cracked and the liftoff was incomplete. Electrically, the traces from the contacts to the electrodes were non-conductive. However, when the arrays were fabricated using the hybrid parylene C/HT process, the evaporation and liftoff on the HT surface occurred routinely (Figure 3-48). In addition, electrical testing of contact-electrode-contact circuits using sets of 45-μm-wide traces ranging 56 mm to 70 mm in length revealed impedances ranging from approximately 12.8 kΩ to 16.7 kΩ, depending on the lengths of the traces in the circuit (the high resistance is due to the thin nature of the iridium wires).

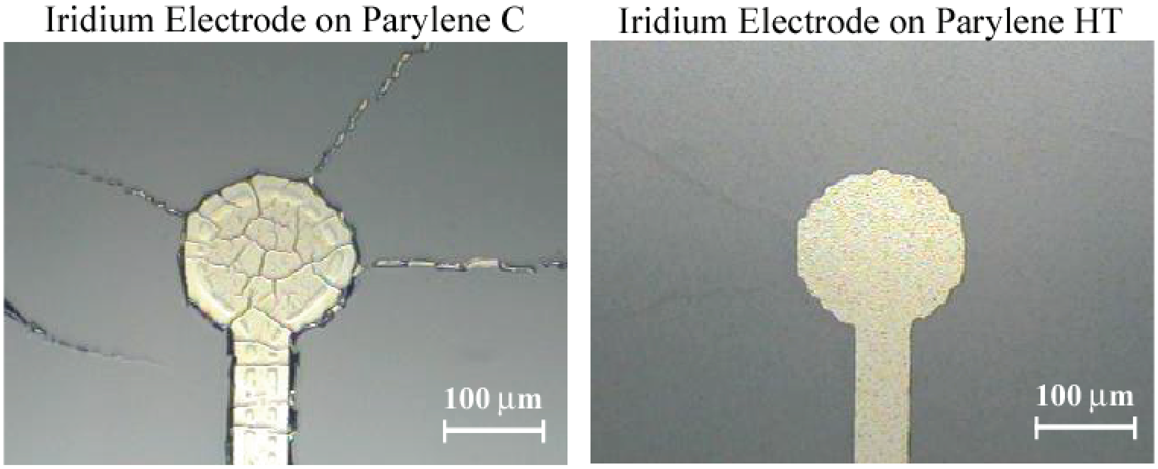

Figure 3-48. Photomicrograph of an iridium electrode on a parylene C surface after liftoff (left) compared with an iridium electrode on a parylene HT surface after liftoff (right). Parylene HT enables fabrication of flexible iridium electrode arrays through thermal evaporation.

An SEM of a fabricated parylene HT-based iridium electrode array is shown in Figure 3-49. The composition of the electrode surface was analyzed via energy dispersive spectroscopy (EDS) (histogram in Figure 3-50) and verified to be iridium (the fluorine and carbon are from parylene HT). This work constitutes, to our knowledge, the first time that iridium electrode arrays have been successfully fabricated on a parylene substrate through thermal evaporation. Future work includes electrochemical analysis and chronic pulsing of these and similarly fabricated iridium arrays.

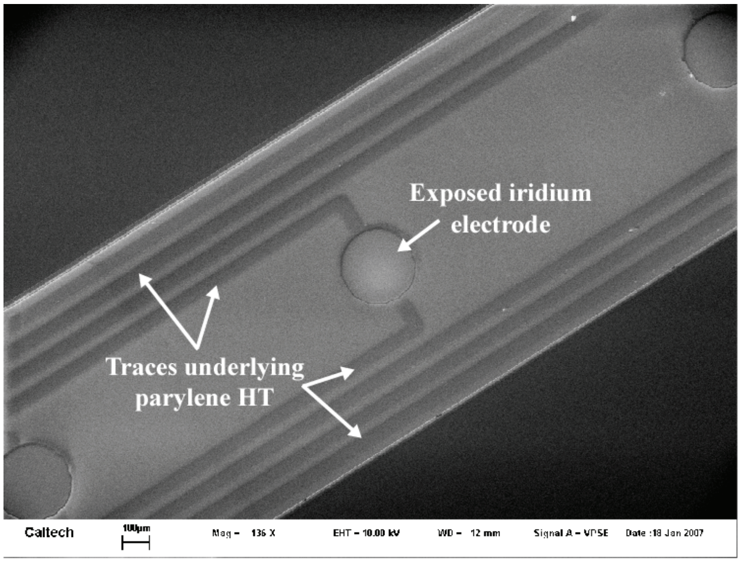

Figure 3-49. SEM of a fabricated parylene HT-based iridium MEA.

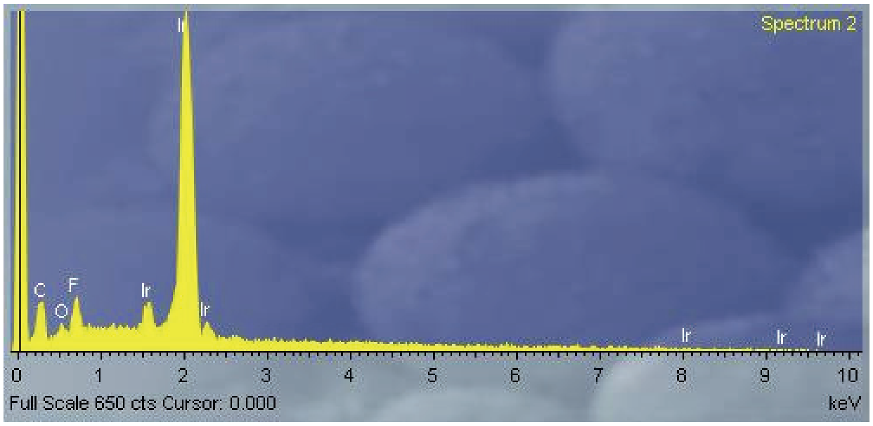

Figure 3-50. Compositional analysis through EDS verified exposed material is iridium.

3.6 Conclusions

Single- and dual-metal-layer fabrication processes for parylene-based electrode arrays have been outlined and demonstrated as robust techniques for building flexible MEAs. These revolutionary MEAs have the ability to stimulate and record from neural tissue in the retina, and demonstrate excellent biostability when chronically implanted in contact with canine retinas. The parylene-enabled dual-metal-layer process allows increased electrode density while obviating many of the issues typically associated with single-layer arrays, such as constraints on electrode size and electrode crowding due to wire routing. It is a simple matter to extend this process to increase the number of metal and parylene insulation layers, as will likely be necessary to fabricate a fully connected 1024-electrode device of approximately the same geometry. High surface-area platinum electroplating technology has shown encouraging results in terms of extending electrode life while also decreasing electrochemical impedance. In addition, evaporated iridium electrode arrays have been fabricated using the novel high-temperature stable variant of parylene, parylene HT, further adding to the repertoire of parylene-based technologies for neural interfaces.

Given these excellent results, we believe the next steps should include chronic stimulation tests *in vivo* in an animal retina to demonstrate long-term stimulation efficacy and biostability. In addition, it will be important to evaluate these electrode arrays at a much larger scale for a full understanding of possible failure modes. Additional electroplating technologies will be explored using processes that have already been qualified for use in retinal implantation, so that the compatibility of these techniques with our parylene electrode arrays can be studied. In the next chapter, we further the discussion of these parylene arrays through an exposition of the application of this technology to spinal cord prosthetics.

4 MULTIELECTRODE ARRAYS FOR SPINAL CORD STIMULATION AND RECORDING

4.1 Introduction

The same technology as described in the previous chapter can be applied in various other neural stimulation and recording applications. We have chosen to investigate the use of parylene-based multielectrode arrays in spinal cord prosthetics. In this chapter, we discuss the overall system for spinal cord stimulation and recording, show electrode arrays that have been fabricated to test the feasibility of such a system, and present both stimulation and recording results from our arrays in murine models. Our ultimate goal, given the known biocompatibility of parylene and the dearth of studies using high-density electrode arrays in cases of spinal cord injury, is to use a high-density parylene-based electrode array to facilitate stepping and standing in patients with spinal cord injury. Although we do not expect to control and time muscle activity directly to accomplish this, because of the innate functionality of the spinal cord, even after transection, we do aim to modulate the activity of the spinal cord using subthreshold electrical fields generated by the array. In addition, the ability to record from the electrodes in the array enables critical studies of cord activity as well as incoming sensory information, and, ultimately, modification of the stimulation parameters to achieve optimal stepping and standing. The goal of the present work, however, is to show that our electrodes can directly couple to the spinal cord through both stimulation and recording. Stimulation from our electrodes in this chapter is superthreshold to show this coupling capability, with the assumption that subthreshold tonic stimulation would be equally possible.

4.2 System Overview

The ideal spinal cord stimulation system, just like the retinal system, would have a power source, circuitry for driving the appropriate electrodes, as well as a cable and electrode array, this time implanted epidurally or subdurally on the spinal cord. We believe that a penetrating electrode array would be problematic for implantation and would likely lose efficacy and fail ultimately due to a gliosis over time, as has been shown in many other studies [34]. The power source could be an RF coil, or could, due to the much larger space available in the abdomen and back as compared with the eye, be a rechargeable battery capable of charging through the inductive link. The RF coil, in addition, would enable reprogramming of the implanted electronics for alternative stimulation protocols at the physician's discretion. The electrode array should be conformable to the spinal cord so that it can tonically stimulate at low currents and with high precision. While a completely implantable system is the ultimate goal, an interim goal is to stimulate the spinal cord chronically from an array connected to a head plug,

Figure 4-1. Proposed system for spinal cord array studies in a chronic murine preparation.

while simultaneously being able to record electromyograms (EMGs) (Figure 4-1). In order to achieve this, we have studied the efficacy of the multielectrode array portion of this system and have begun to develop a connector technology capable of connecting 36 electrodes in with a small enough form factor to be chronically mounted on a mouse skull.

4.3 Fabrication

Spinal cord arrays, consisting of five or ten electrodes of 250 μm diameter were designed (Figure 4-2). Interelectrode spacing was controlled so that each array of electrodes covered four to five segments of the murine lumbosacral spinal cord upon implantation. Suture holes were also designed into the body of the array to ensure proper

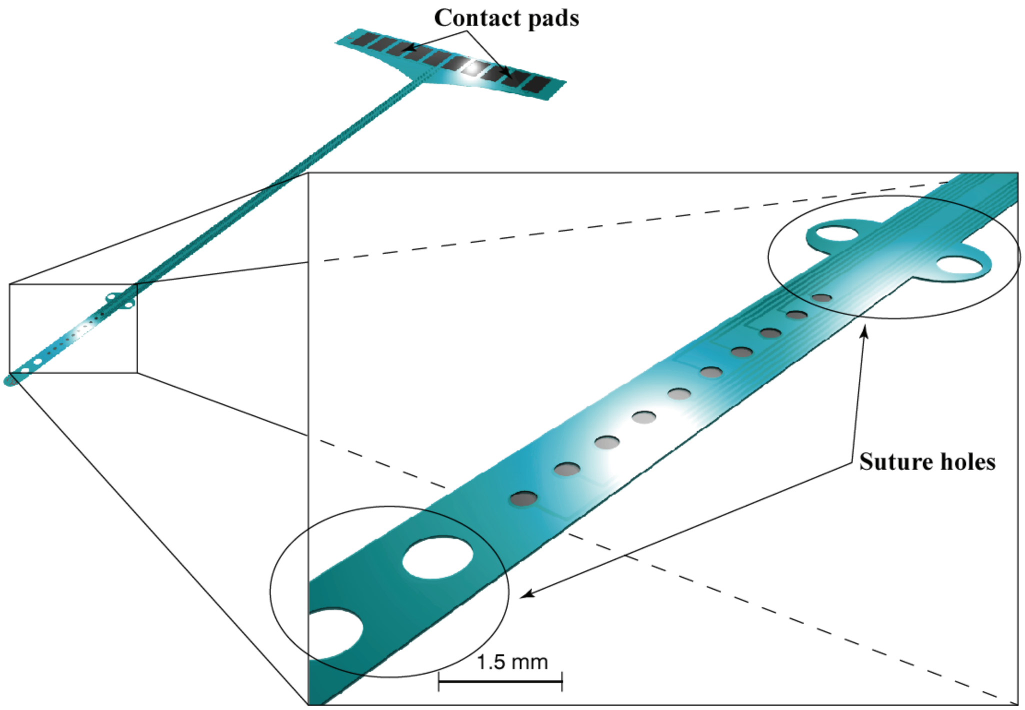

Figure 4-2. Graphical depiction of spinal cord MEA. Contact pads were designed to connect to Clincher connectors.

placement and attachment of the array on the cord, as well as to facilitate implantation (suture can be attached to the end of the array and can be threaded along the cord first to help direct the array along it).

The single-metal layer fabrication process was performed in the same manner as in Section 3.3.2, using a contact aligner process for fast throughput. The fabricated arrays were annealed to increase the adhesion of parylene to parylene. At the same time, they were clamped between two pieces of Teflon or glass slides coated with aluminum foil to ensure they would be flat during implantation. In the future, a specially designed metal cylinder could be used to more closely approximate the electrode arrays to the curvature of the spinal cord. The arrays were connected via Clincher connectors (FCI, Versailles Cedex, France) to the stimulation and recording electronics.

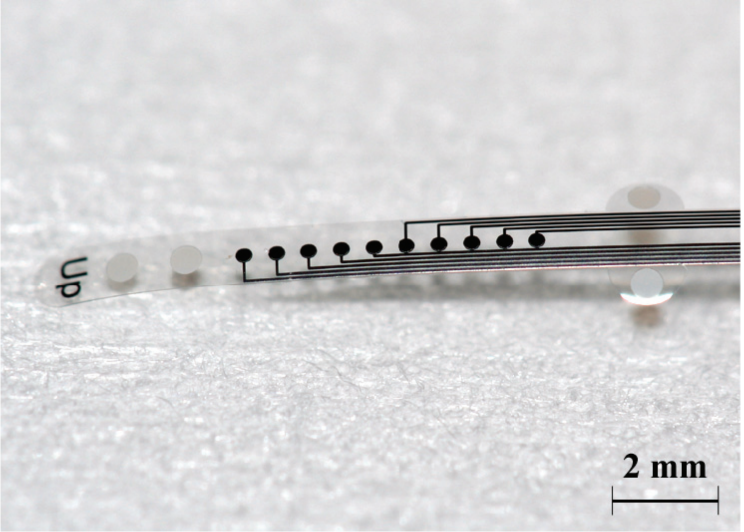

Figure 4-3. Parylene MEA for murine spinal cord stimulation and recording.

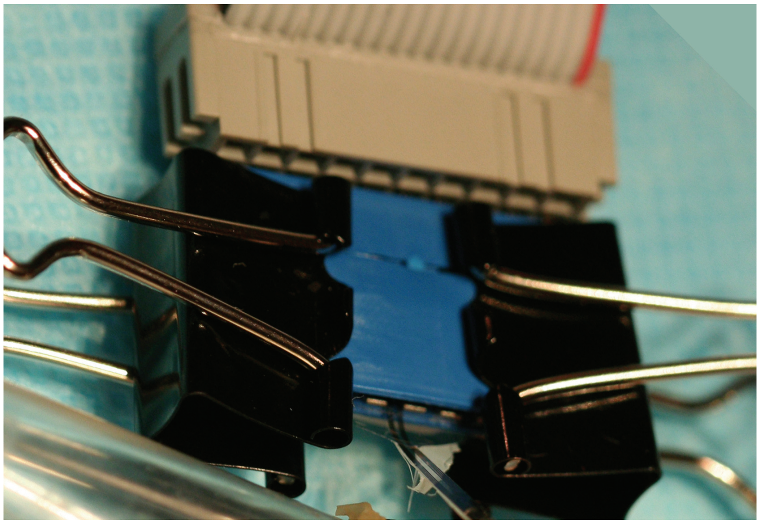

Figure 4-4. Clincher connector for connecting array to stimulation and recording electronics.

4.4 Results and Discussion

Just prior to implantation, the arrays were rinsed in isopropyl alcohol. Under isoflurane anesthesia, the spinal cord electrode arrays were implanted epidurally on spinal cord segments L2-S1 in nontransected mice. The electrodes were oriented linearly along the rostrocaudal extent of the cord. Recording capability was assessed by using the electrode array to record spinal cord potentials evoked by tibial nerve stimulation. Following stimulation of the tibial nerve, somatosensory evoked potentials were recorded from the cord dorsum at three lumbosacral levels (P1-P3, rostral to caudal). The recorded waveform consisted of three response peaks, two of which are clearly depicted in Figure 4-5 (N1 and N3). These findings closely mirror results reported previously in a study using conventional spinal cord recording electrodes [123] demonstrating that the recording capability of the array electrodes matches that of conventional electrodes. By measuring the difference in the response latencies obtained at each electrode position (corresponding to different levels of the spinal cord), and by utilizing the known, fixed interelectrode spacing, accurate measurements of the conduction velocities were obtained. The properties of these responses can potentially be used to diagnose the progressive recovery of the spinal cord as a result of treatments provided after a spinal cord injury.

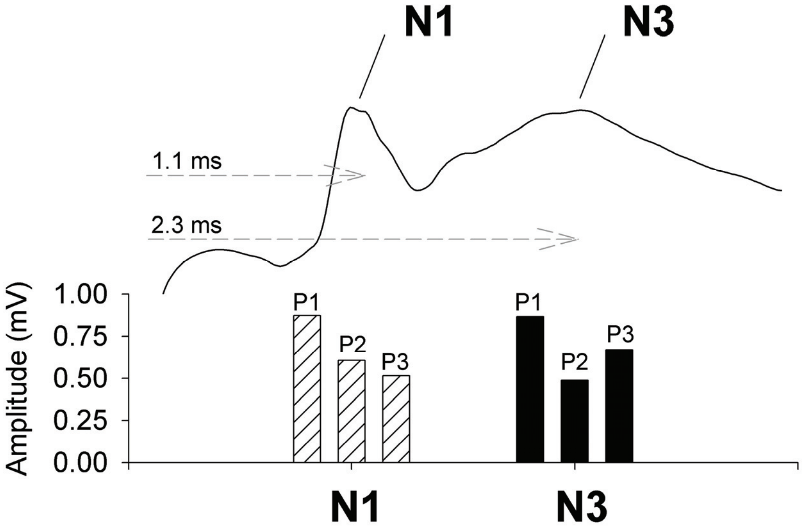

Figure 4-5. Peak amplitudes of somatosensory evoked potentials (N1 and N3) recorded from three levels of the rostrocaudal spinal cord (P1-P3). Example waveform at top shows approximate response times.

To test the capability of the electrode array to act as a multichannel stimulating device for generating hindlimb movements, constant-current monophasic stimulus pulses (amplitude: 50-850 μA, frequency: 0.3-10 Hz, pulse duration: 0.5 ms) were applied to the spinal cord between each of the array electrodes and a ground electrode located near the shoulder, while muscle activity was monitored using electromyogram (EMG) recordings of the tibialis anterior and medial gastrocnemius muscles. Stimulation generated a typical three-component EMG action potential consisting of an early (direct motor), a middle (monosynaptic), and a late (polysynaptic) response, classified by post-stimulus latency (Figure 4-6). These data clearly indicate that the parylene arrays were able to stimulate the spinal cord in such a way that the musculature was activated.

Because of the known spacing of the electrodes on the array (as compared with traditional fine-wire electrodes which do not have known interelectrode spacing), we were able, in addition, to determine whether electrode position had a significant impact

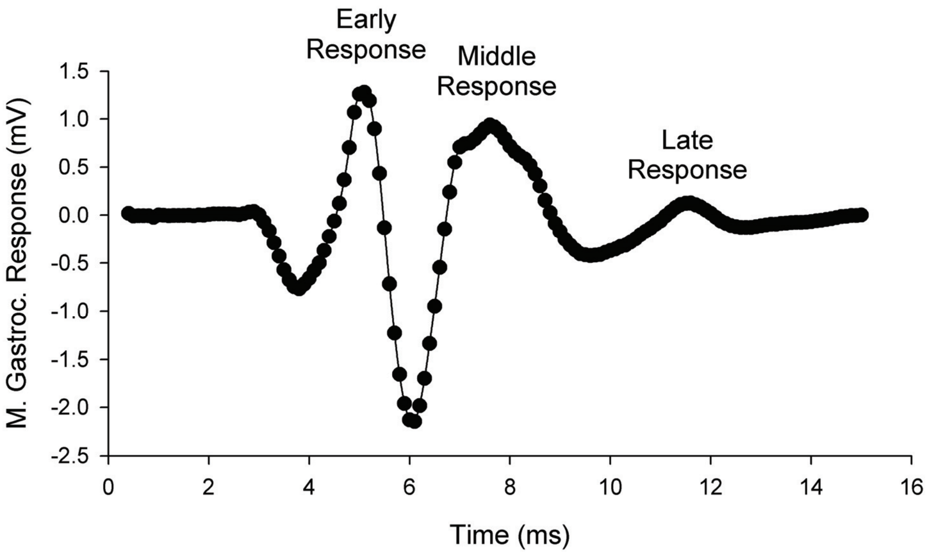

Figure 4-6. Typical medial gastrocnemius (ankle plantarflexor) EMG recording showing early, middle, and late responses after stimulation of spinal cord with parylene MEA.

on muscle recruitment. The appearance and magnitude of each of the EMG responses was indeed correlated with the choice of electrode position (Figure 4-7). This serves as evidence that position of stimulation is very important. With a one-dimensional array, it is difficult to assess whether a bilateral stimulation paradigm would also result in lateralization of response, but we strongly suspect that this would be the case.

Varying the interelectrode spacing between the stimulating electrode and a ground electrode now on the array, as opposed to at the shoulder, affected the sensitivity with which the target muscles were activated. The recruitment profile of the medial gastrocnemius middle response is shown in Figure 4-8 using interelectrode spacings of 1500 μm (filled bars) and 4500 μm (unfilled bars). With the smaller spacing, graded

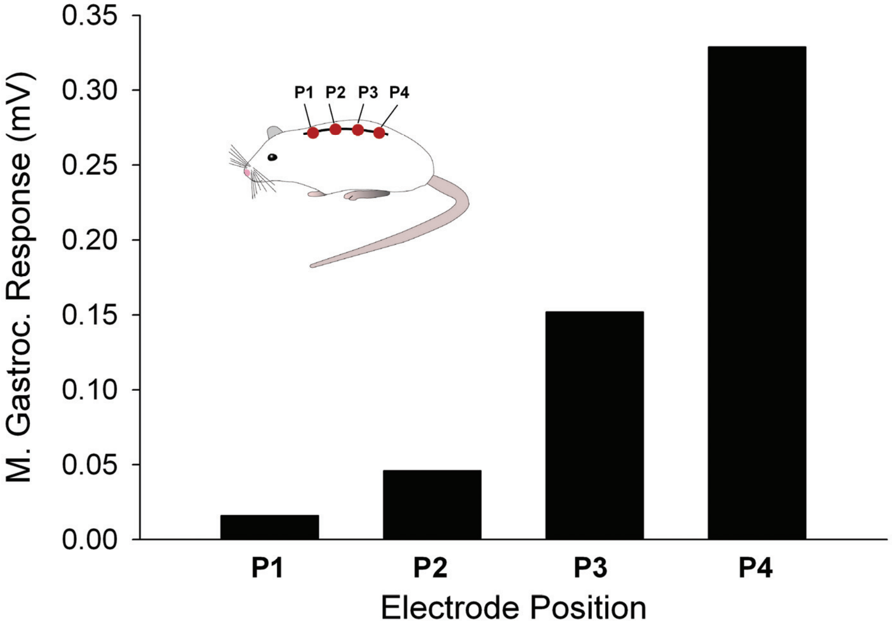

Figure 4-7. Medial gastrocnemius EMG showing varying levels of activation due to stimulation at different rostrocaudally located electrode sites.

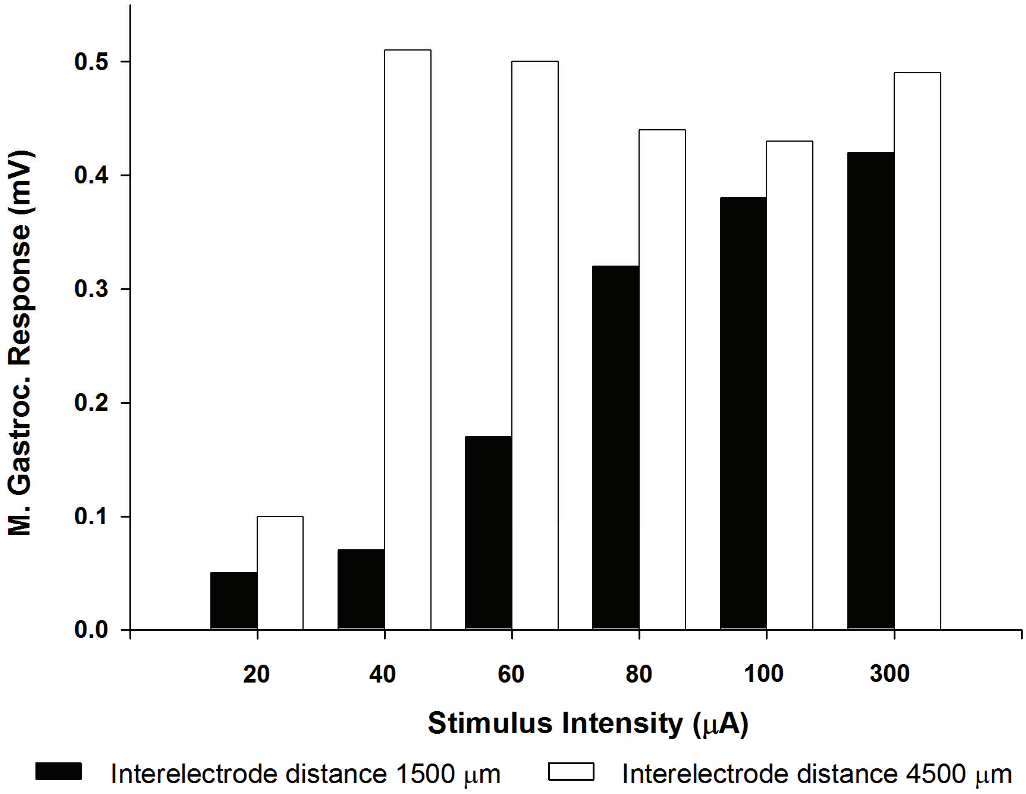

Figure 4-8. Effect of interelectrode spacing on muscle recruitment. Smaller spacings yielded graded muscle activation while larger spacings yielded maximal amplitude responses at low currents.

muscle activation was achieved. With the larger spacing, approaching a monopolar configuration, the muscle quickly attained maximal activation at low currents. Thus, the specific goal and sensitivity requirements of a particular motor task may dictate optimal interelectrode spacing and whether a monopolar or bipolar configuration is chosen.

4.5 Connectors

In order to achieve a chronically implantable system for our future studies, we have investigated the possibility of using a tight-pitch connector technology to serve as the electrical conduit between the stimulation and EMG recording electronics and the implanted device. A prototype spinal cord electrode array has been connected to a high-density assembly incorporating two 18 pin Omnetics Nano connectors (Omnetics Corporation, Minneapolis, MN, USA) and a PCB stiffener (Figure 4-9). These connectors mate with wired adaptors that enable connection to a breadboard, head unit, or other components necessary for recording and stimulation. A more robust and reliable connection methodology has been used to achieve electrical continuity between the pins of the connector and the parylene-based electrode contacts (Figure 4-10) with additional hardening of these connections through silicone encapsulation (Figure 4-11). Using this method, five electrodes have been connected using forward and return lines to two pins each, for a total of 10 pins of connectivity. As can be seen, this connector assembly has 36 pins available for connection. This connection strategy is readily scalable to enable higher-density arrays, for example, as will likely be necessary for human implants, and is fully compatible with the dual-layer process outlined in Chapter 3.

This connector, because it has been strengthened using thick silicone encapsulation of the pin region, is robust even under vigorous movement. Furthermore, moisture permeation to the pins is minimized using this protective method, long delaying and likely preventing any failure due to corrosive mechanisms at the connector. A ten-electrode array has been assembled in an identical fashion and is ready for *in vivo* testing. In addition, we are currently at the development stage with higher density and bilateral arrays.

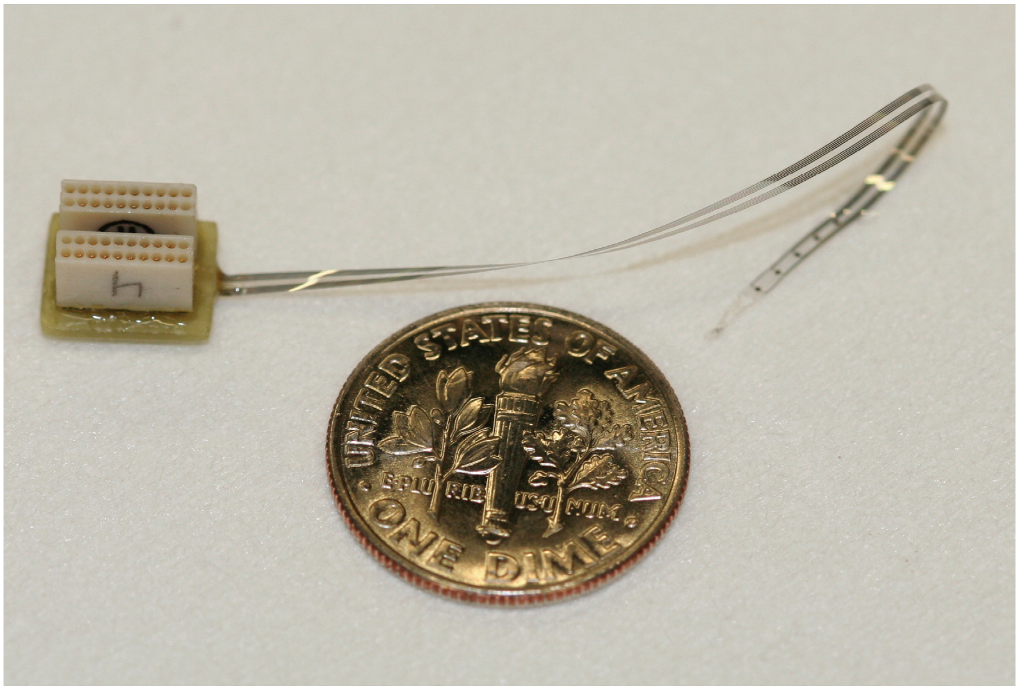

Figure 4-9. Five-electrode array connected to Omnetics assembly. In this prototype, forward and return lines to ten pins enable confirmation of high yield electrical continuity from the connector to each of the five electrodes in the prototype array. The connector assembly weighs approximately one gram after silicone encapsulation.

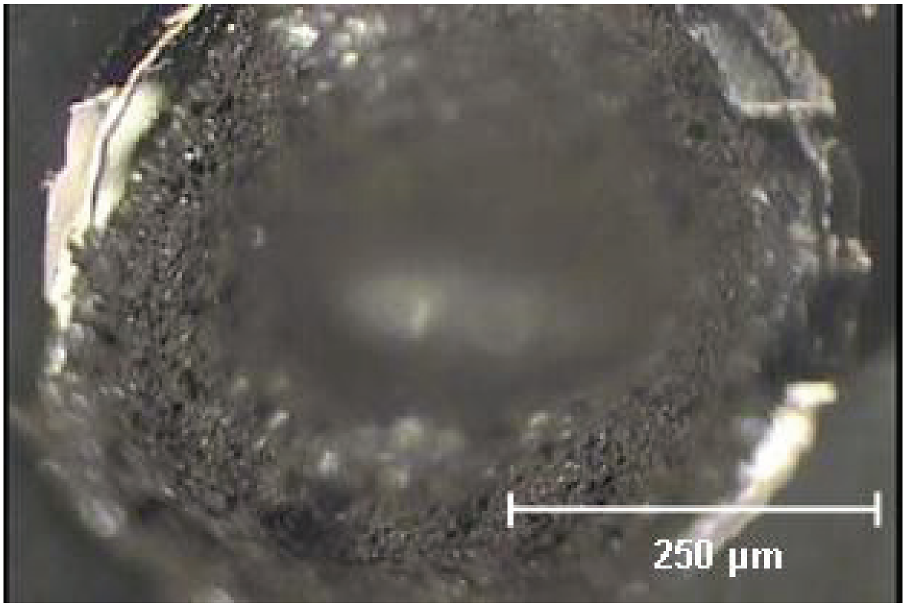

Figure 4-10. Metal bump joining pin of Omnetics Nano connector to electrode contact to enable high-density connection. Pin-to-pin pitch is approximately 650 µm.

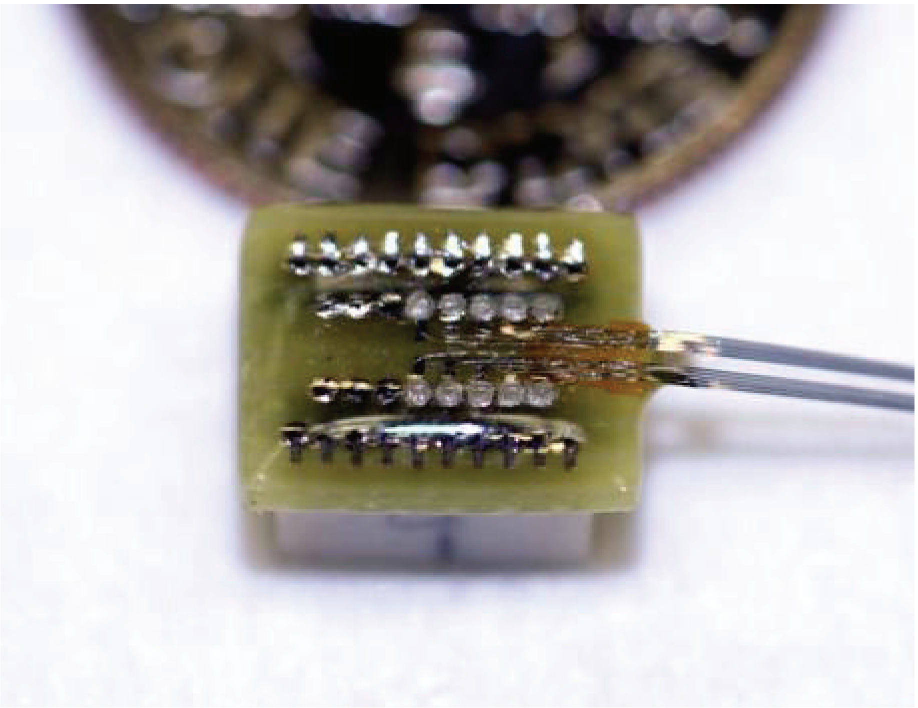

Figure 4-11. Silicone encapsulation at the region adjoining the parylene array with the Omnetics connector assembly hardens device against movement-related failures and prevents moisture penetration and corrosion at the pin to contact junctions.

4.6 Conclusions

As these results have shown, parylene-based electrode arrays can very useful in studies of the spinal cord and, most likely, for spinal cord prostheses for the treatment of spinal cord injury. The advantages of these microfabricated flexible MEAs, when compared with traditional fine-wire electrode arrays, include their ability to stimulate and record from locations with predetermined positions (with slight surgical variations) and very exact interelectrode spacings. Currently, we are developing higher-density MEAs capable of finer, bilateral stimulation for assessing the somatotopic distribution of locomotor circuits in the spinal cord. We believe that in order to achieve this without making the array excessively wide, these will have to be fabricated according to the multi-metal-layer fabrication process presented in Chapter 3. Our future work includes studies using these arrays in transected mice at both subthreshold and superthreshold levels, and use in different animal models, such as in the rat, to begin to assess scalability prior to human implantation. At the same time, we have started work using other already approved low-density chronic arrays in humans to assess epidural and subdural stimulation capability and efficacy in cases of spinal cord damage. We strongly believe that our ability to fabricate high-density biocompatible chronically implantable arrays that are flexible enough to conform to the dorsum of the spinal cord may lead to revolutionary treatments for patients with spinal cord injury.

5 CHIP-LEVEL INTEGRATED INTERCONNECT TECHNOLOGY

5.1 Introduction

Despite our ability to fabricate such a large number of electrodes in such a small area, a significant impediment to future progress is the problem of how to package and interconnect these multielectrode arrays with foundry-fabricated ASICs, discrete components (e.g., chip capacitors, oscillators, diodes) and RF coils in a way that provides for high lead-count interconnects. A wafer-level process is cost prohibitive, as it is necessary to maximize the area of a wafer devoted to IC processing to keep costs low. Furthermore, current technologies for packaging would be far too tedious and low yield to apply to a 1000-electrode device. In order to achieve our goal of a 1000-electrode retinal prosthesis and a high-density spinal cord stimulation system, then, a new way of forming such a package so as to enable high-lead-count integration is necessary.

We have invented a way to place prefabricated chips, manufactured, for example, at a foundry, into the fabrication process of a parylene-based multielectrode array and/or RF coil, such that all interconnections to the chip are made using standard photolithography and standard microfabrication techniques in a fully scalable manner [80]. This packaging scheme is now known as the chip-level integrated interconnect (CL-I^2) package. Figure 5-1 illustrates this concept, showing how a prefabricated stand-alone IC chip is can be directly integrated with an MEA and with, ultimately RF coil power and data connections. Figure 5-2 shows an overview of the fabrication process and how multiple chips could be joined together in this manner. A detailed discussion of the fabrication process, as adapted from [80], follows.

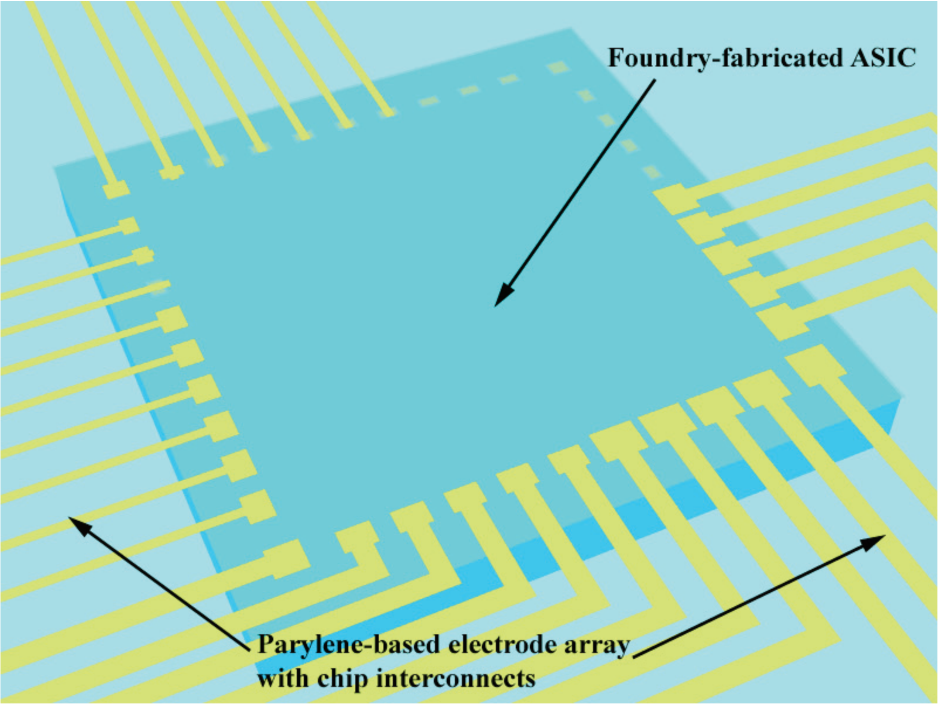

Figure 5-1. Illustration of the CL-I^2 packaging concept. A prefabricated ASIC or discrete component can be placed directly into the fabrication process of an overlying multielectrode array.

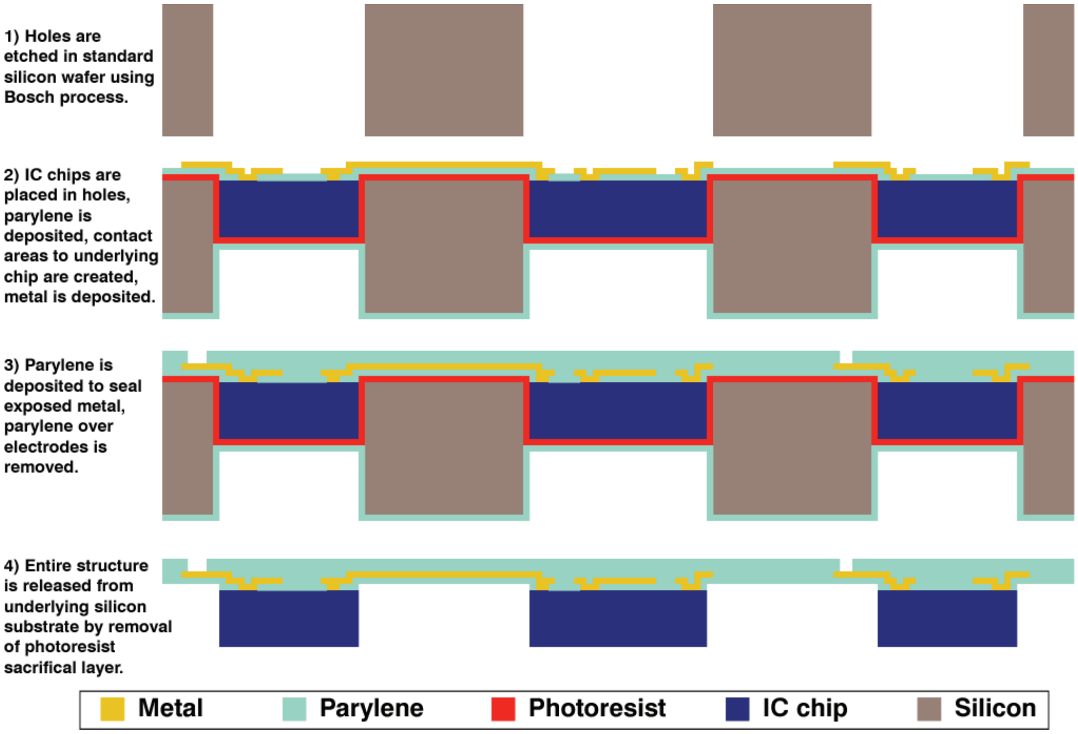

Figure 5-2. Overview of the CL-I^2 process. Multiple chip connections are possible.

5.2 Fabrication

Three MOSIS-fabricated ASICs, as well as seven chips fabricated to simulate them (with circuitry that facilitated testing), were used to demonstrate the CL-I^2 packaging technology. In order to fabricate the replicas of the MOSIS chips, these chips were imaged using a WYKO interferometer (Veeco Instruments Inc., Woodbury, NY, USA), and were found to have mean dimensions of 2.500 mm in length, 2.617 mm in width, and 254.2 µm in total thickness (Figure 5-3).

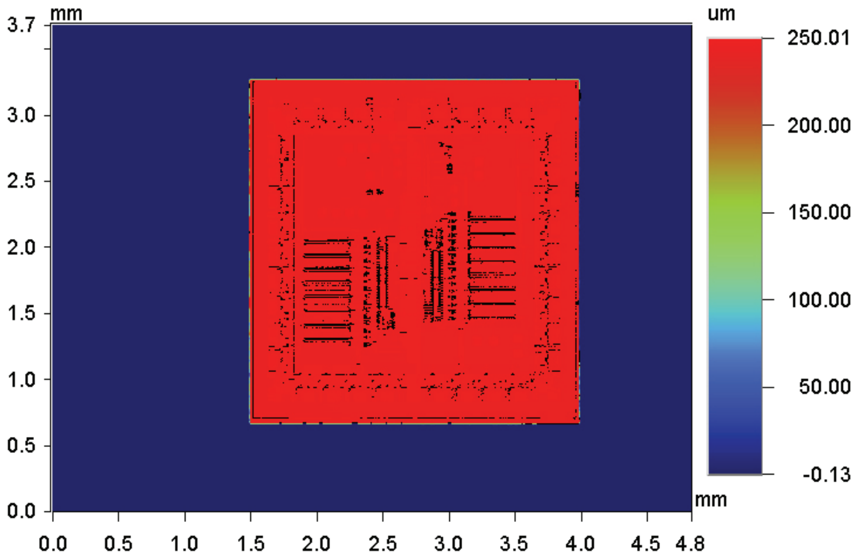

Figure 5-3. WYKO image of MOSIS-fabricated chip. Data were used to assess diced chip dimensions.

One hundred angstroms of chrome and 2000 Å of gold were e-beam evaporated on a 260 µm thick silicon wafer. Using a photoresist mask, the metal was wet etched to pattern pads of the same size and in the same locations as on the MOSIS-fabricated chips (approximately 70–100 × 100 μm^2 with a center-to-center pad spacing of approximately 200 µm), as well as a pattern of short circuits connecting these pads to nearby pads. After stripping the photoresist, a second photoresist layer was spun on the wafer and patterned as a mask for a Bosch through-wafer etch in a PlasmaTherm SLR-770B deep reactive ion etching (DRIE) system (Unaxis Corporation, St. Petersburg, FL, USA). This etch defined the length, width, and thickness of the simulated chips as 2.49 mm, 2.61 mm, and 260 µm, respectively. Finally, the photoresist mask was removed from the individual chips. In this manner, chips comprising simple electrical shorts and intrinsic resistors were fabricated as our primary CL-I^2 package test structures (Figure 5-4).

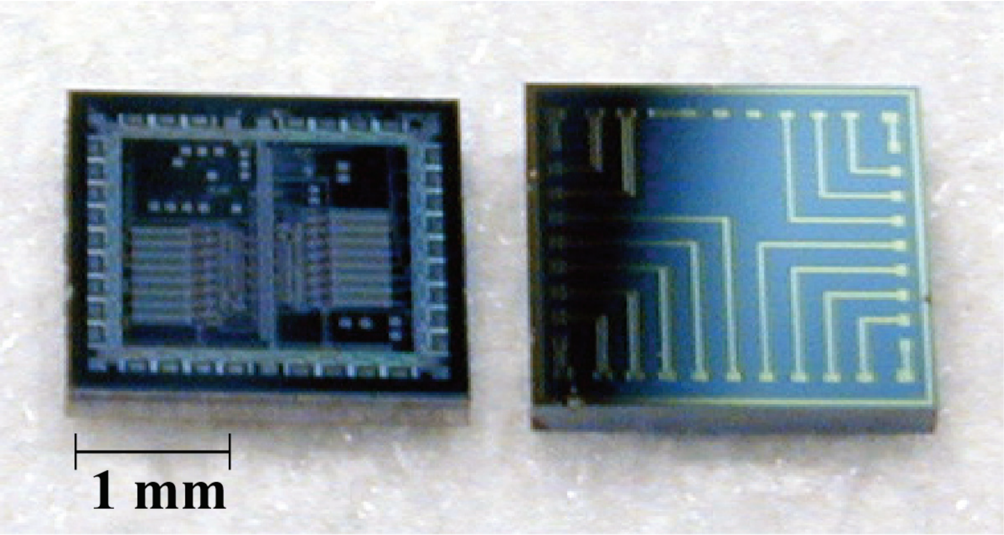

Figure 5-4. MOSIS ASIC (left) next to test chip (right).

The only properties of these prefabricated chips that had to be known before incorporation in the CL-I^2 process were their overall length, width, and thickness, and the dimensions and locations of the contact pads. Figure 5-5 gives a detailed CL-I^2 process flow, and Figure 5-6 gives a cross-sectional depiction of the interconnects as they are formed (corresponding to steps 5 through 10 of Figure 5-5). The complete fabrication process is given in Appendix D. To begin, shallow alignment marks are etched into a standard 550 μm thick silicon wafer using a thin photoresist mask and an SF_6 plasma. 2.51×2.63 mm^2 holes are then patterned after alignment in a 10X reduction stepper in thick photoresist and an optional silicon dioxide mask. Through holes are then etched using the Bosch DRIE process. After photoresist and oxide removal, Nitto tape is placed on the frontside of the wafer. The chips are then self-aligned in the holes by inserting them from the backside (the Nitto tape enables frontside planarization whereas the lateral dimensions of the etched cavity determine lateral displacement), and they are sealed in place using several drops of sacrificial photoresist to cover the backside of the chip and to fill the gaps around it. A subsequent approximately 12 µm thick parylene C deposition in a PDS2010 mechanically anchors the chips in place from the backside. After removal of the frontside parylene by peeling off the Nitto tape, vertical displacements of the chips are measured using a stylus profilometer (Alphastep 200 and P-15, KLA-Tencor, San Jose, CA, USA).

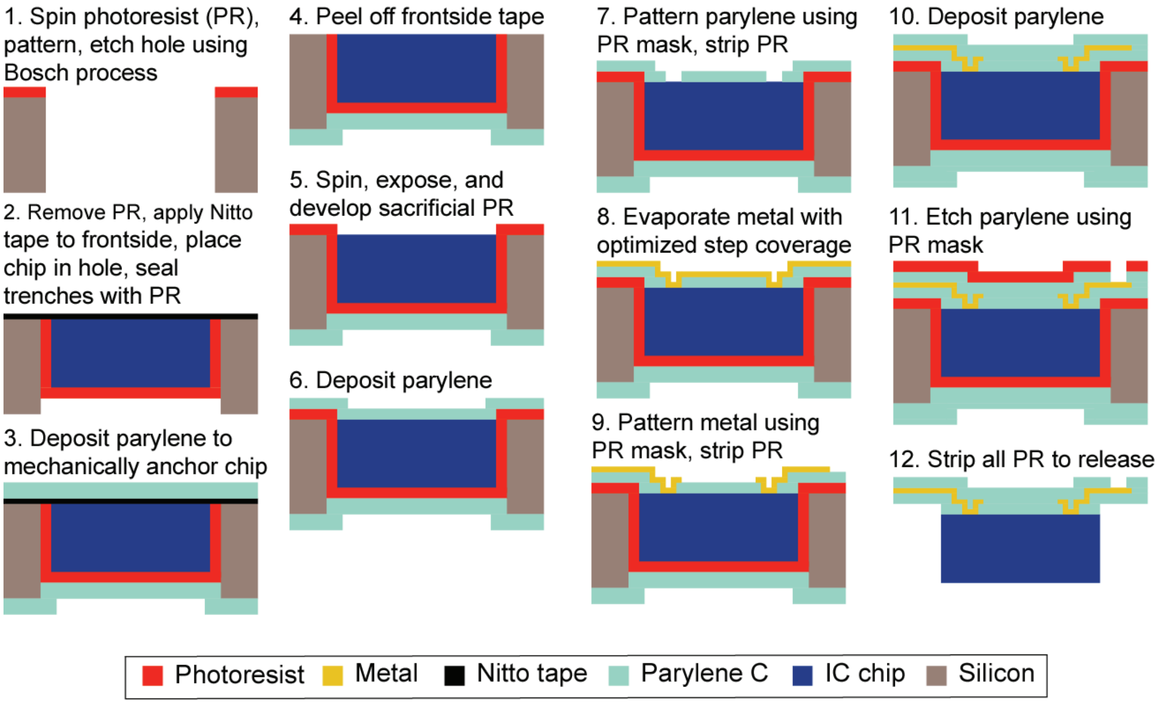

Figure 5-5. Detailed process flow for CL-I^2 package fabrication.

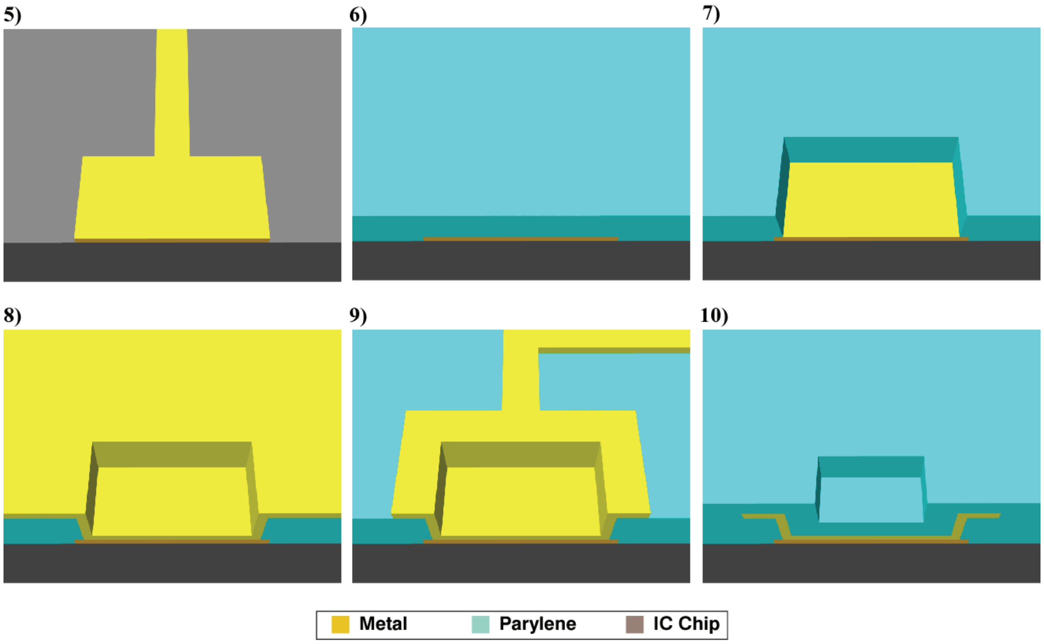

Figure 5-6. Interconnect cross-sectional views corresponding to steps 5–10 of Figure 5-5.

The parylene-based flexible electrodes, or, in this implementation, contact pads for electrical testing, are then fabricated on this wafer as if it were a whole wafer with prefabricated integrated circuitry. First, a photoresist sacrificial layer is spun on the wafer and patterned to expose the chip's surface. After baking to remove excess solvent, approximately 3 µm of parylene C is deposited on the entire wafer. Photoresist is spun on the wafer, exposed in the 10X reduction stepper, and developed to pattern etch holes above the on-chip pads, similar to the vias in the dual metal-layer process. This pattern is transferred into the parylene using an O_2 plasma in an RIE system, exposing the metal of these on-chip pads. Two hundred angstroms of titanium and 2000 Å of gold are deposited in the e-beam evaporation system using optimized step coverage, and patterned (using a photoresist mask and wet etching) to define the remote contact pads and remote pad to on-chip pad interconnects. The top photoresist is stripped, and a second layer of approximately 10 µm of parylene C is deposited and patterned as before, but this time to open the remote pads/electrodes to enable electrical testing. Finally, all photoresist, including the sacrificial layer, is removed by soaking the wafer in acetone, releasing a flexible parylene skin with embedded interconnects to the packaged ASIC. The host wafer can be substituted in the process with a precisely machined substrate, and can be reused after this release step. It is also important to note that the ASIC or discrete component can be of any thickness, but generally the thickness should be less than that of the host wafer or machined substrate, and it can have parylene or any hermetic coating deposited on it *a priori*, provided that the chip contacts can be opened using microfabrication techniques before the interconnect metal is laid down and patterned (Figure 5-5 and Figure 5-6, steps 8 and 9). Thus, this technology combines the best aspects of chip-level packaging, in which every surface of the prefabricated chip can be manipulated or coated beforehand, and wafer-level packaging, in that photolithography and microfabrication can be performed on the surface after such chip-level techniques.

5.3 Integration Testing Results

We successfully performed photolithography on ten prefabricated stand-alone chips using this paradigm: seven test chips (three conformally coated in parylene *a priori*) and three MOSIS-fabricated chips (one coated in parylene *a priori*). A MOSIS chip anchored in place in the host substrate (i.e., after step 4 of Figure 5-5) is shown centrally in Figure 5-7 with the host wafer shown on the perimeter. As is expected, minimizing vertical displacement of the ASIC from the wafer surface is crucial for further photolithography steps. Figure 5-8 gives typical surface profiles of all ten chips

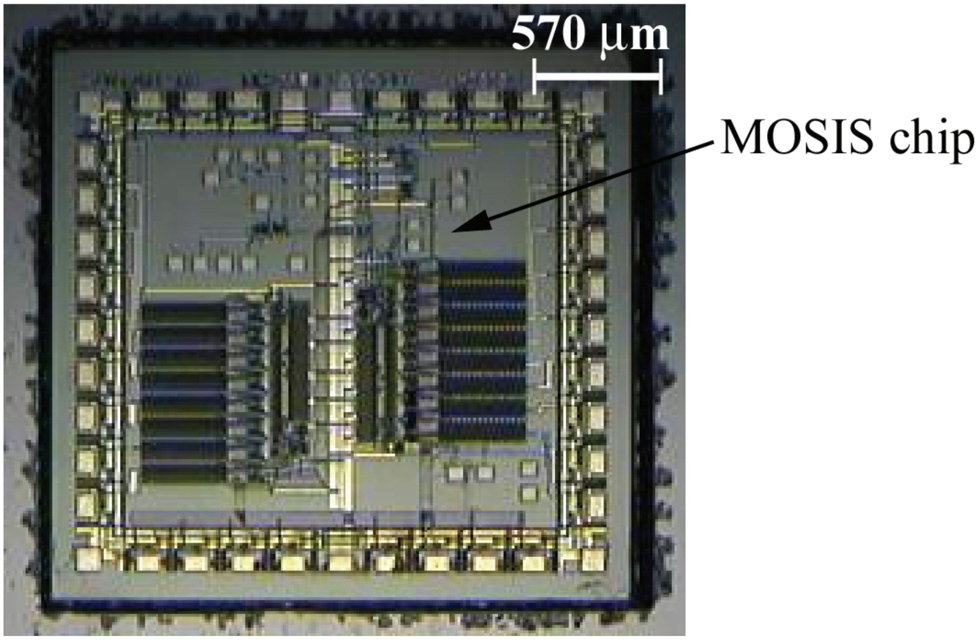

Figure 5-7. MOSIS chip (center) shown anchored in host silicon substrate (perimeter).

with respect to the surrounding host wafer, and indicates that for most chips, this vertical displacement was less than 5 μm after removal of the frontside Nitto tape. Photolithography on the somewhat anomalous test chips 2 and 7, however, was also successful. A detailed three-dimensional profile of the surface of MOSIS chip 3 and its surrounding host substrate is shown in Figure 5-9. As can be seen, the entire chip is recessed only 2.5 μm and is parallel with the host wafer's surface.

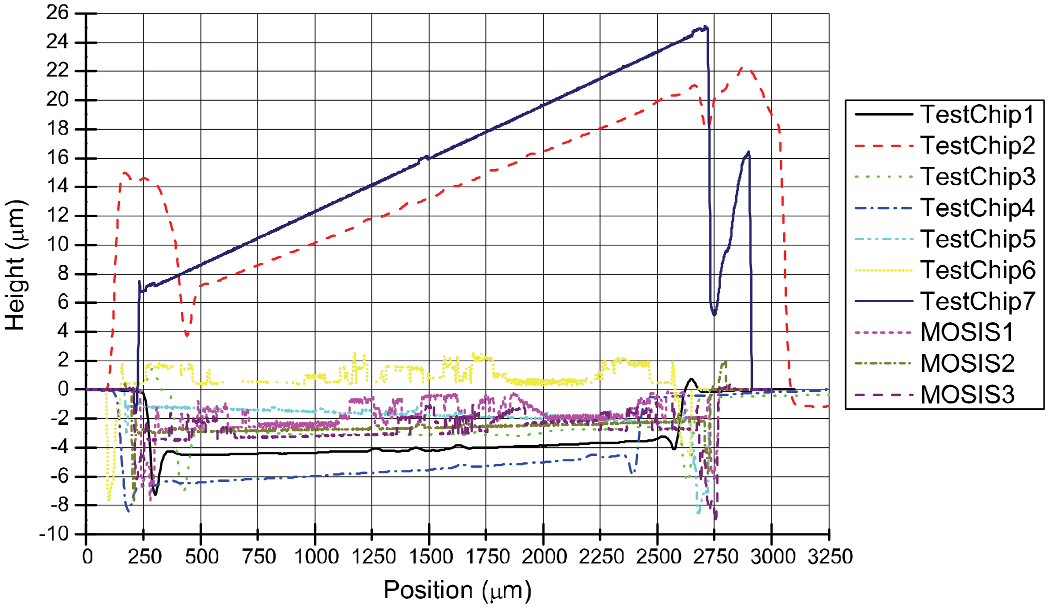

Figure 5-8. Typical single-axis vertical displacements of all 10 chips after mechanical anchoring in the host wafer (Figure 5-6, step 4), where the top surface of the wafer corresponds to 0 μm.

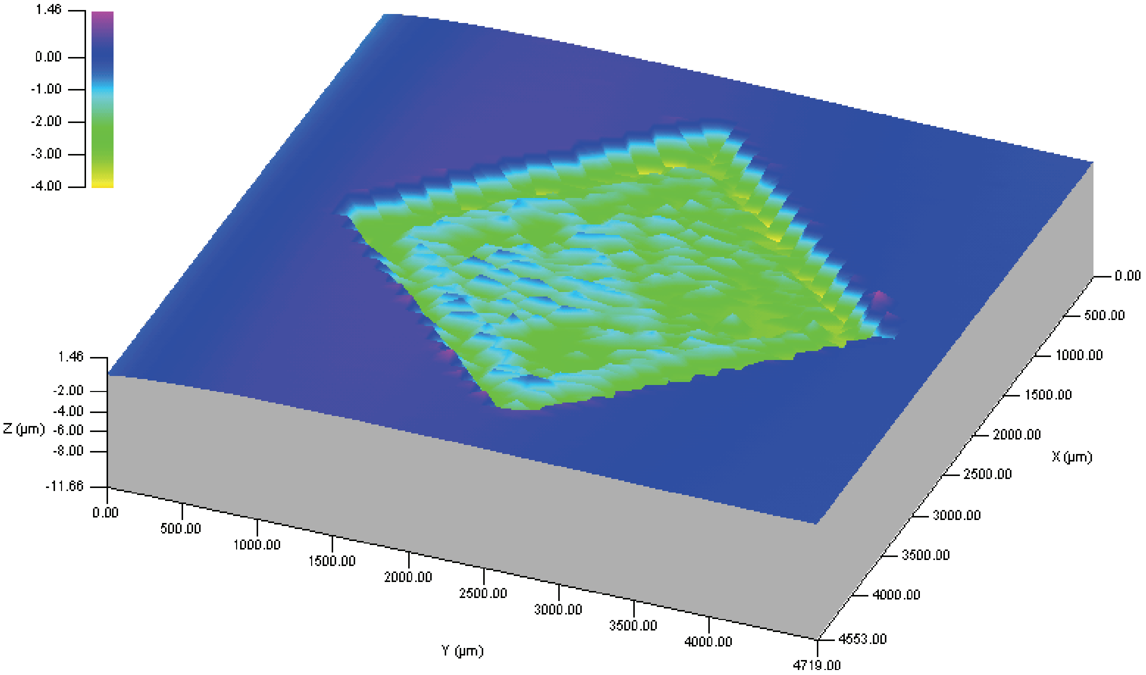

Figure 5-9. Detailed 3D profile of MOSIS chip 3 after mechanical anchoring in the host wafer.

The accurate horizontal alignment of the perimeter interconnects to the embedded chips is shown in Figure 5-10, with Figure 5-11 giving a detailed micrograph of a single interconnect for both the test chip (a) and the MOSIS chip (b). By design, the chips should be self-aligned to within 10 µm of lateral displacement; some chips were aligned far better than this, however others were misaligned worse than this. With tighter tolerances on the cavity sidewalls, or with chip-alignment lithographic equipment, this alignment error could be improved. The embedded chip with remote contact pads is shown in Figure 5-12, and Figure 5-13 depicts the flexibility of this package.

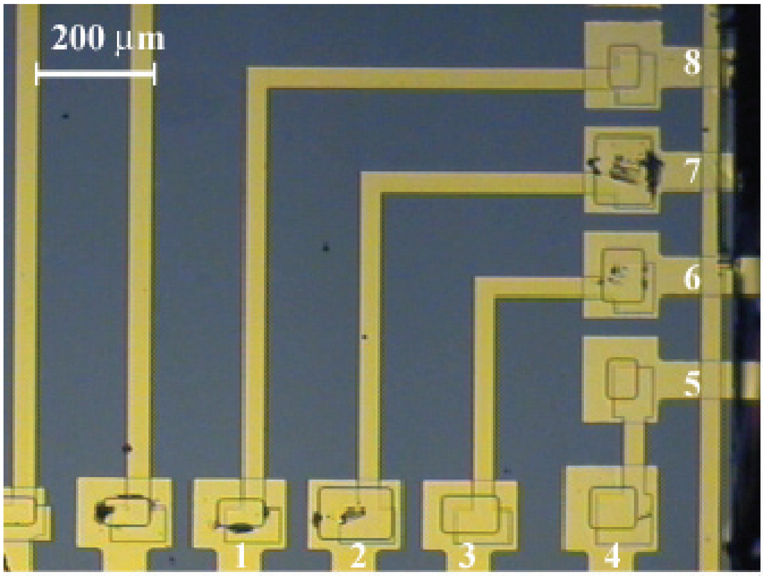

Figure 5-10. Embedded chip with fabricated perimeter interconnects (numbered traces connect to numbered remote pads shown in Figure 5-12).

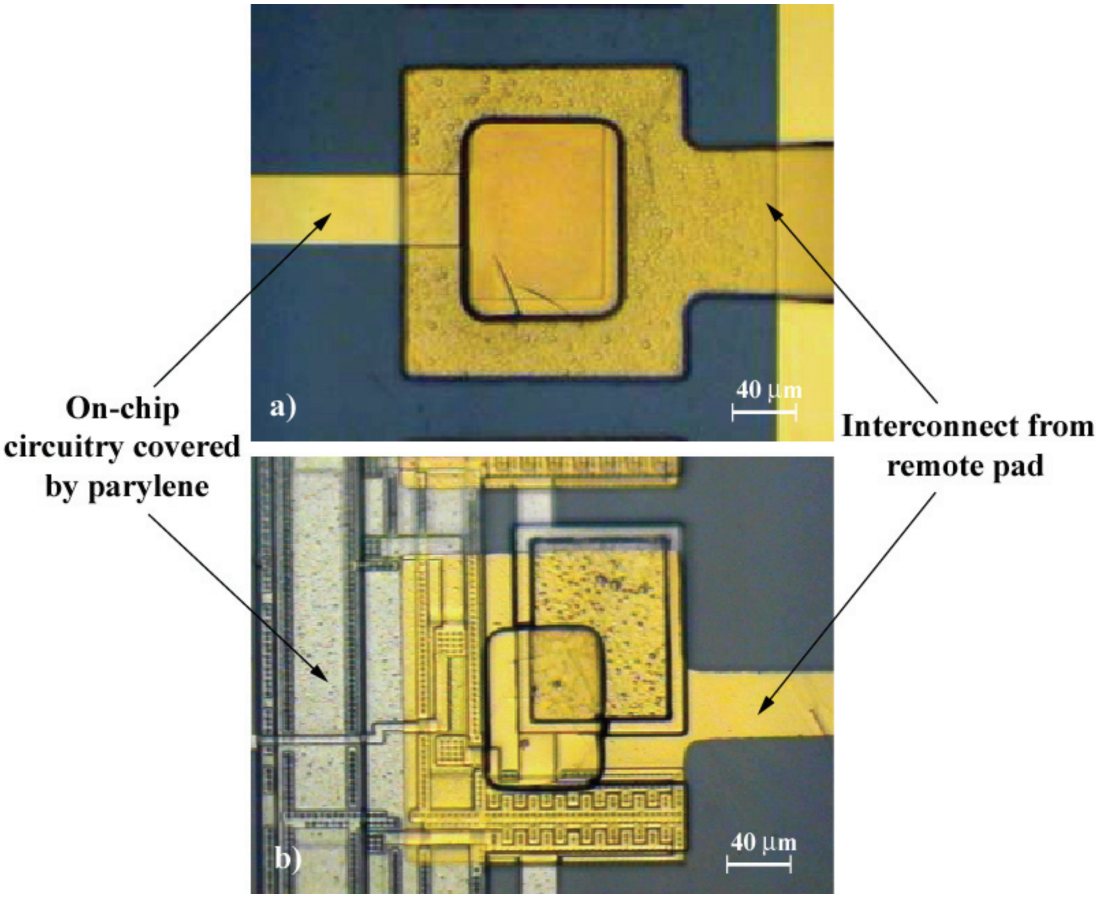

Figure 5-11. (a) Example of <10 µm lateral misalignment of a test chip; (b) Example of >10 µm lateral misalignment of a MOSIS chip.

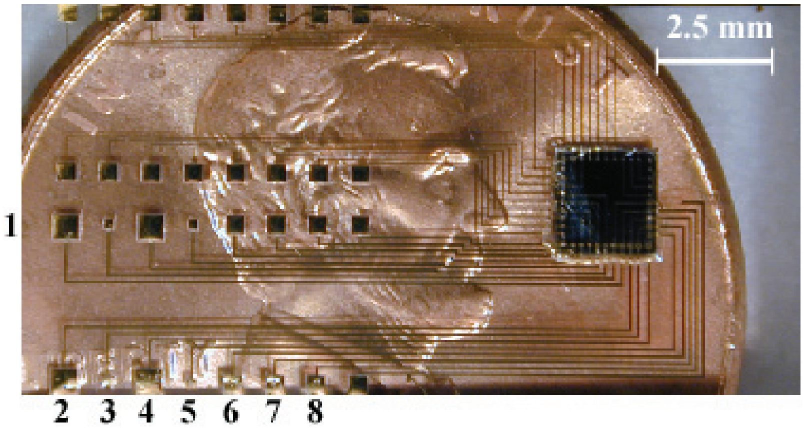

Figure 5-12. A CL-I^2 packaged chip shown resting on a penny (numbered pads used to generate to Table 5-1).

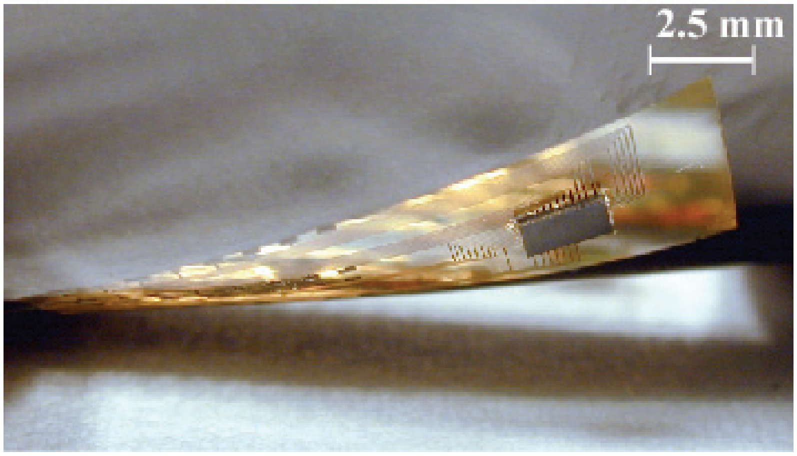

Figure 5-13. Demonstrates flexibility of CL-I^2 package. Chip can be seen underlying overlying parylene "skin."

The electrical resistance values between remote pads connected to the on-chip pads in a quadrant of a typical test chip (Table 5-1) are those expected: the electrical nature of the connection between pads 1 and 8, 2 and 7, 3 and 6, and 4 and 5 is a short with an average resistance of ~59.7 Ω, whereas, for example, shorted pads 3 and 6 show approximately the same intrinsic through-die resistance to pad 4. The measured I-V curve for the short (e.g., remote pad 3 across test chip to remote pad 6) showed ohmic contact (Figure 5-14 (left)), whereas for the intrinsic circuit (e.g., remote pad 3 through highly doped intrinsic resistor to remote pad 4) it showed the expected Schottky effect (Figure 5-14 (right)). Similar functional contacts with the MOSIS chip's pads were also verified.

Table 5-1. Resistance in Ω between remote pads connected to the embedded chip (arrows indicate shorted pairs)

Pad	1	2	3	4	5	6	7	8
1		323000	327000	330000	327000	325000	322000	61.0
2	323000		577000	448000	441000	580000	60.9	325000
3	327000	577000		599000	582000	59.9	454000	319000
4	330000	448000	599000		57.1	587000	499000	319000
5	327000	441000	582000	57.1		569000	490000	320000
6	325000	580000	59.9	587000	569000		478000	321000
7	322000	60.9	454000	499000	490000	478000		316000
8	61.0	325000	319000	319000	320000	321000	316000	

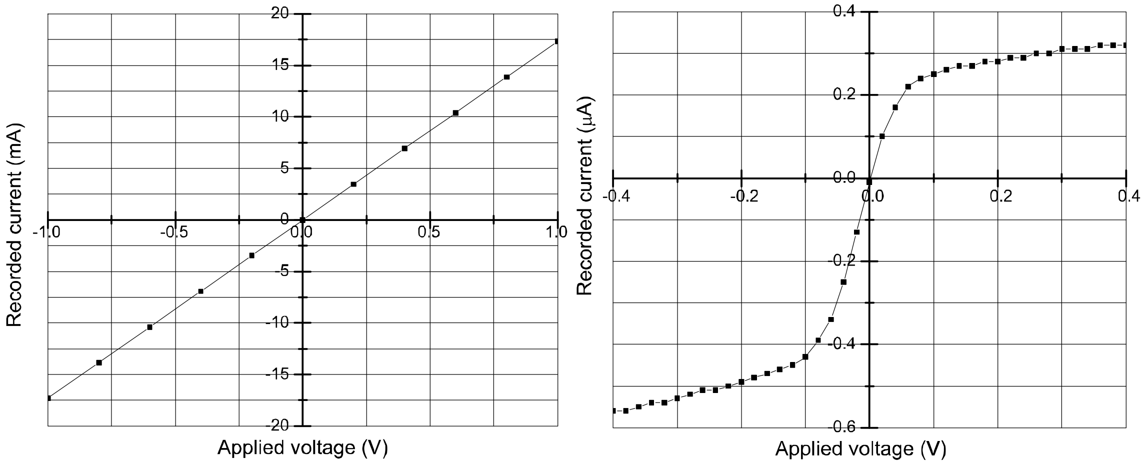

Figure 5-14. Measured I-V curves for short (left) and intrinsic circuit (right).

5.4 Discussion

It should be stressed that the lead-count and interconnect density limitations for this technology stem only from the limitations of the microfabrication and photolithography equipment used to fabricate the CL-I^2 package, and, in particular, to pattern the first parylene etch (Figure 5-5 and Figure 5-6, step 7). All interconnects to the chip are fabricated simultaneously during the metal deposition step, and depend on optimal step coverage of the parylene sidewall (aided in part by the slightly isotropic nature of the O_2 plasma etch of parylene [109]). The CL-I^2 process thus avoids the use of tedious and comparatively low-density ball-wedge [77] or wire bonding.

Our method of incorporating discrete modules into a MEMS process is far more cost-effective when compared with full-wafer IC processing and MEMS integration [124], because valuable space on the wafer is not wasted during the IC fabrication step. Furthermore, in comparison to other ASIC integration attempts [124-126], this packaging scheme is superior for biodevices because it takes advantage of parylene's low water-absorption [127] and highly conformal pinhole-free deposition, and because the package is both flexible and biocompatible. Among the feasible uses for this technology is the interconnection of chips, devices such as other CMOS-compatible MEMS, as well as discrete components such as chip capacitors, fabricated using different materials and processes, to make large conglomerate circuits for neural prostheses and for other applications. This technology is capable of far surpassing the projected number of I/O interconnects expected to be available by 2010 [128], while using lead-free, biocompatible materials. Fabrication is not limited to the use of parylene as either the backside anchoring material or as the frontside electrode insulation material, although, because of its superior electrical, mechanical, and water permeability properties when compared with other polymers, we believe parylene will ultimately prove to be the best choice for monolithic high-density neural prosthetics. It is interesting to note that another research group has, after our original publications [80, 129, 130], explored an integration technique in polyimide very similar to ours, with interconnect density motivations much akin to our own [131].

5.5 Monolithic System Design and Processing

We have designed a complete monolithic system that is currently undergoing process characterization and refinement. This system comprises a BION stimulator chip designed for neuromuscular prostheses [132], two chip capacitors (AVX Corporation, Myrtle Beach, SC, USA), and a specially designed three-layer RF coil. The chip capacitors and BION chips (after dicing) were analyzed using the WKYO system (Figure 5-15) to obtain their dimensions, which were averaged for the mask design.

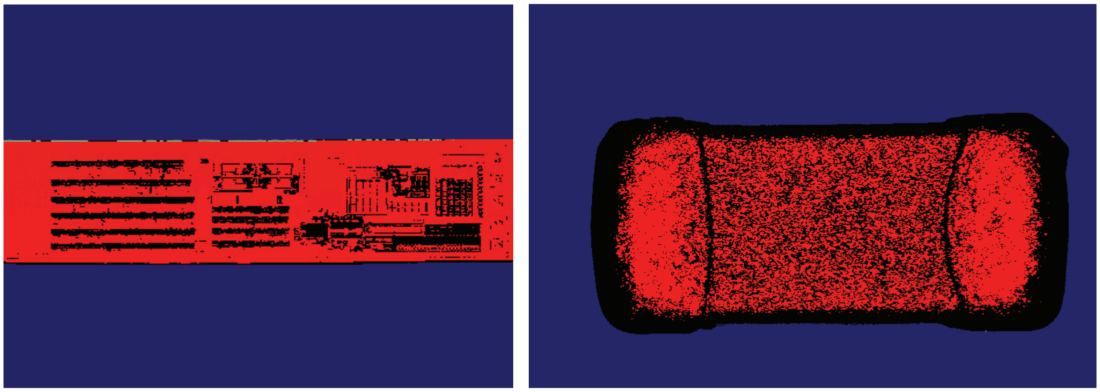

Figure 5-15. WYKO Images of BION chip (left) and AVX chip capacitor (right) (not to scale).

The components are all connected according to the CL-I^2 integration process, as shown in the mask design given in Figure 5-16. The complete fabrication process flow is given in Figure 5-17. This process is divided into two sections: the RF coil fabrication process, and the chip integration process. The RF coil is fabricated of gold for low impedance, and the electrodes and interconnects are fabricated of platinum for optimal stimulation capability. A novel via geometry has been incorporated, in which more than four sidewalls are made, to enable more efficient electrical coupling between the components during the final platinum deposition and to minimize possible failure (because these sidewalls are the locations of electrical conduction between the underlying chip and the overlying contacts).

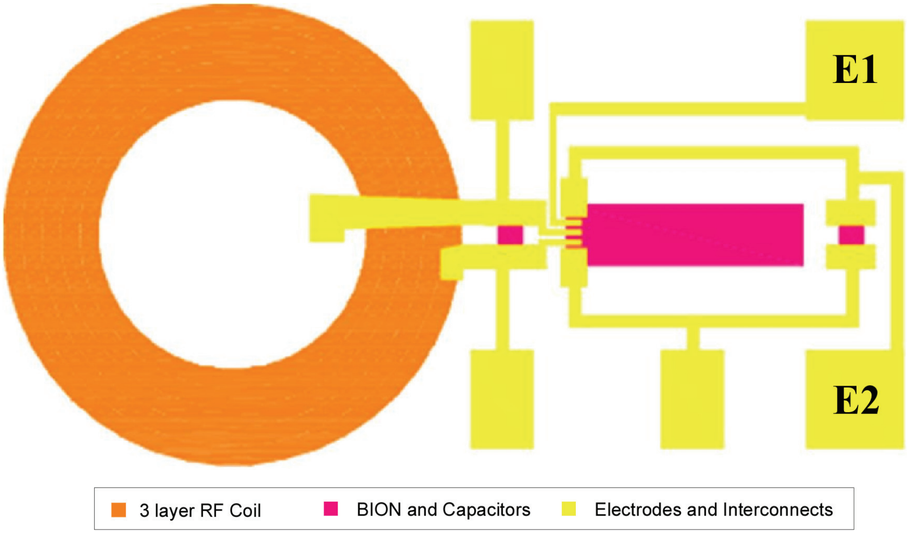

Figure 5-16. Design of completely integrated monolithically fabricated RF controlled stimulator connected according to CL-I^2 process. E1 and E2 are the electrodes controlled by the BION chip.

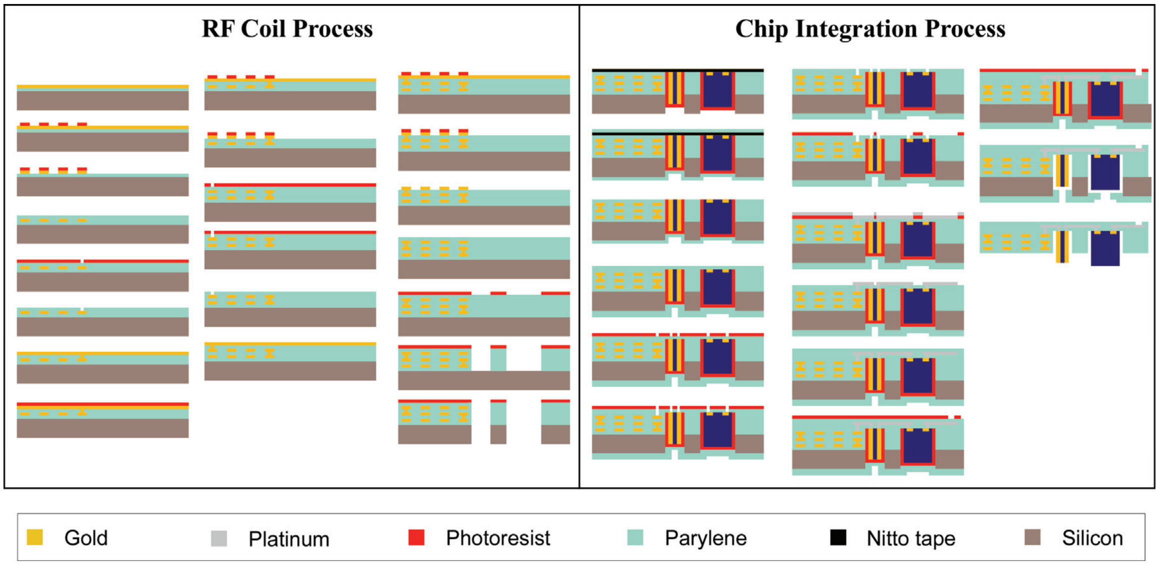

Figure 5-17. Integration process flow for monolithic RF coil stimulator using BION chip and chip capacitors.

Several unusual problems were encountered during processing of this prototype. There were bubbles formed in the parylene and under the gold (Figure 5-18) after deposition and the subsequent metal patterning steps during the RF coil fabrication process, an extremely atypical development. Because of the scarcity of the BION chips available for this fabrication process, and thus our desire for the process to turn out optimally in the first full fabrication run, future work will include repeating this fabrication process. Nevertheless, we have demonstrated the integration concept for a fully functional device using much more highly available RF identification (RFID) chip technology [133]. Although not a fully functional FES system, the RFID system has demonstrated our ability to microfabricate all interconnects to a functional chip and communicate with this chip from an external power source, a very important development. The proposed full monolithic system's microfabrication and integration process is given in Appendix E as a reference for future work.

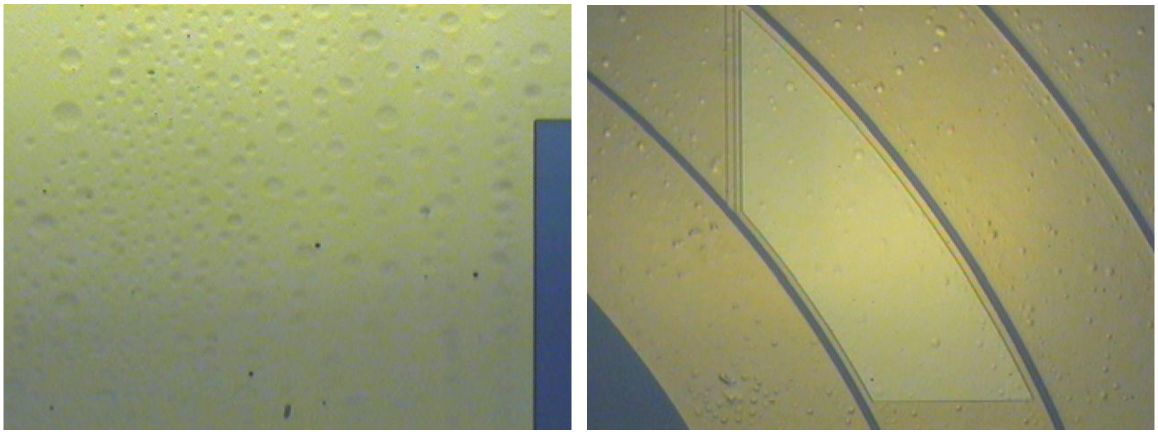

Figure 5-18. Bubbling problem encountered during fabrication of monolithic parylene-based device, requiring refabrication.

5.6 Monolithic Geometry Implantation Studies

It is important to test the feasibility of surgical implantation of such parylene-based devices in animal models to determine optimal implantation technique and to establish the robustness of the devices and materials under surgical manipulation. Already shown in Chapters 3 and 4 was implantation of electrode arrays in both the eye and the spinal cord. Because of the much greater space available in the abdomen and back for spinal cord electrode arrays, we feel that geometrical constraints will not limit technological advancement in this area. However, because of the extreme size limitations placed on a device intended to be placed in the human eye because of its low volume and complex anatomy, it is imperative to evaluate possible geometries for such a device prior to finalizing device specifications. To this end, a prototype geometry for an all-intraocular parylene-based device, simulating the overall profiles of the required components but without the fabrication complexities, was conceived (Figure 5-19) and fabricated in parylene C using a photoresist mask and an oxygen RIE. The design included an RF coil region, intended for implantation in the lens capsule, a flexible cable, to be passed through a posterior capsulotomy into the vitreous cavity, and an electrode array region, designed, as shown before, to be attached to the retina using a retinal tack. The proposed location of the RF coil within the lens capsule or just anterior to it in the ciliary sulcus would enable excellent alignment and coupling of an external primary coil on a pair of glasses with the implanted secondary coil, thus serving as impetus for testing a geometry with such component placement. A dummy chip was epoxied to the cable in one of the possible positions anticipated for the ASIC, partway down the parylene cable.

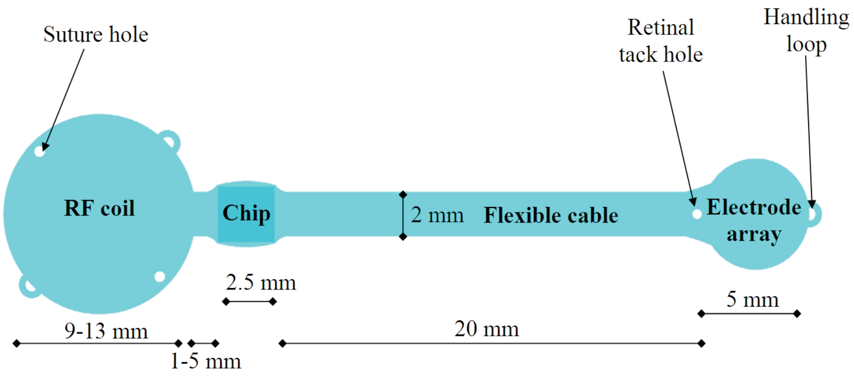

Figure 5-19. Prototype geometry for an all-intraocular parylene-based device with all required component regions for a completely implantable system.

This test structure was then implanted in several *ex vivo* porcine eyes to evaluate surgical approach and determine the device's mechanical stability in the eye (example surgical photographs are given in Figure 5-20). It was determined that O_2 plasma roughening to increase hydrophilicity of the surface in a comparison of several devices made little to no difference in terms of surgical outcome. A significant problem with this initial design was that the flexible cable was too long, causing the cable to fold over itself and become tangled during implantation. In addition, it was discovered that the point of attachment of the flexible cable to the RF coil region caused a cabling effect, where the

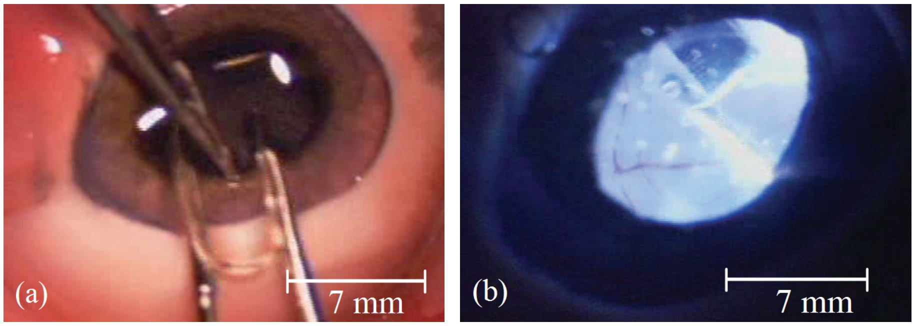

Figure 5-20. Example surgical photographs of prototype geometry implantation under (a) anterior and (b) intravitreal illumination.

RF coil region tended to be drawn through the posterior capsulotomy into the vitreous cavity during surgery.

To mitigate the surgical problems encountered with this first device, a second model was designed (Figure 5-21) that utilizes capsular retaining wings to tether the RF coil region in place in the crystalline lens capsule while the cable exits through the capsulotomy into the posterior segment. In addition, electrodes, wires, and contact pads were added to the overall structure to monitor for electrical malfunction upon implantation. To ease continuity testing, each of the four electrodes in this design was connected via two traces to large contact pads in the RF coil region. The length of the cable was also shortened to facilitate implantation in the porcine and canine animal models (it is important to note that these eyes have different average geometries than human eyes, so precise device dimensions will vary for human implantation). These devices were fabricated successfully (as shown in Figure 5-22 and Figure 5-23). The

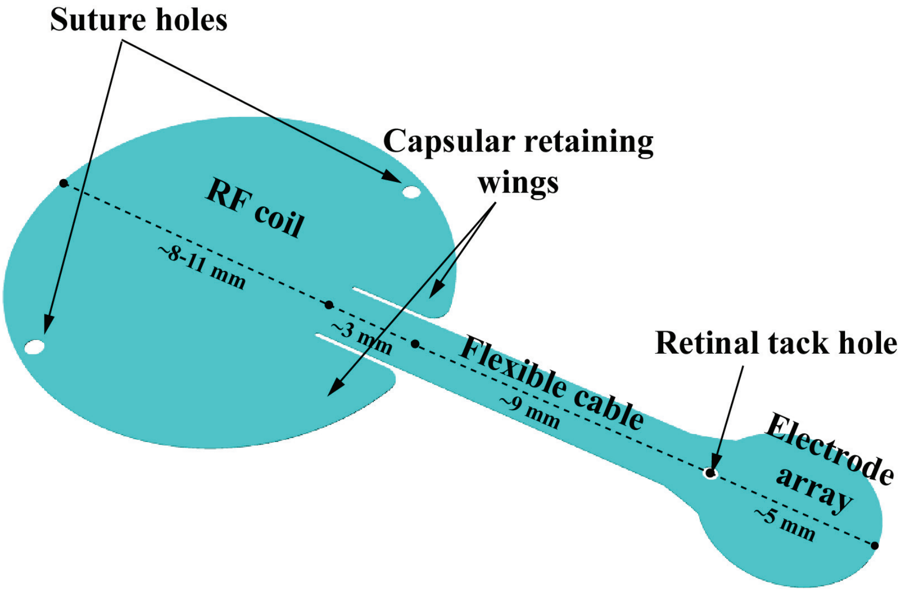

Figure 5-21. Improved geometry for an all-intraocular retinal prosthesis.

surface profile of the electrode region for this device is given in Figure 5-24, showing an overall parylene thickness of approximately 14 μm and electrodes recessed approximately 7 μm from the surface.

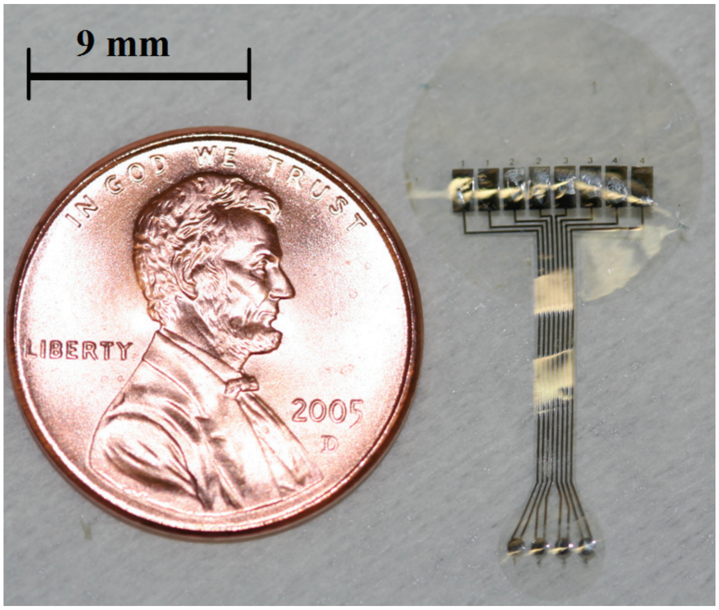

Figure 5-22. Fabricated surgical test structure for mechanical and electrical characterization.

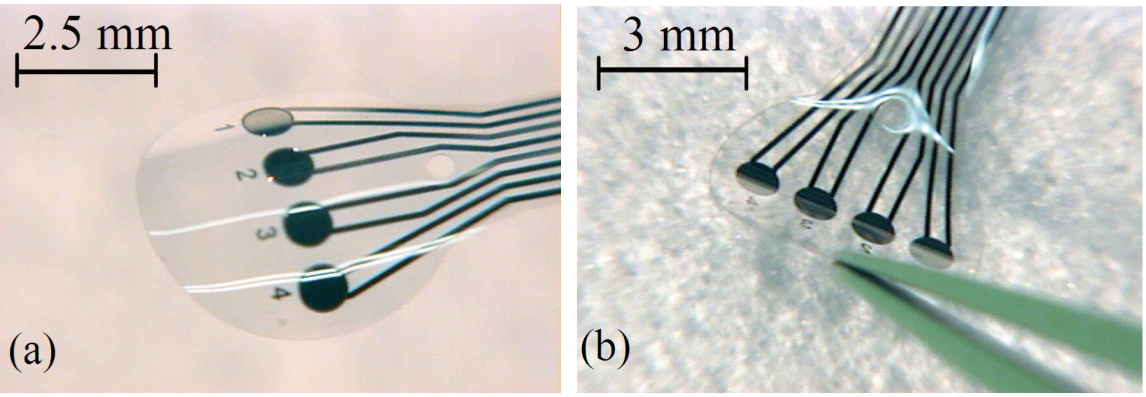

Figure 5-23. Fabricated surgical test structures: (a) retinal aspect highlighting electrodes and (b) vitreal aspect highlighting tack hole.

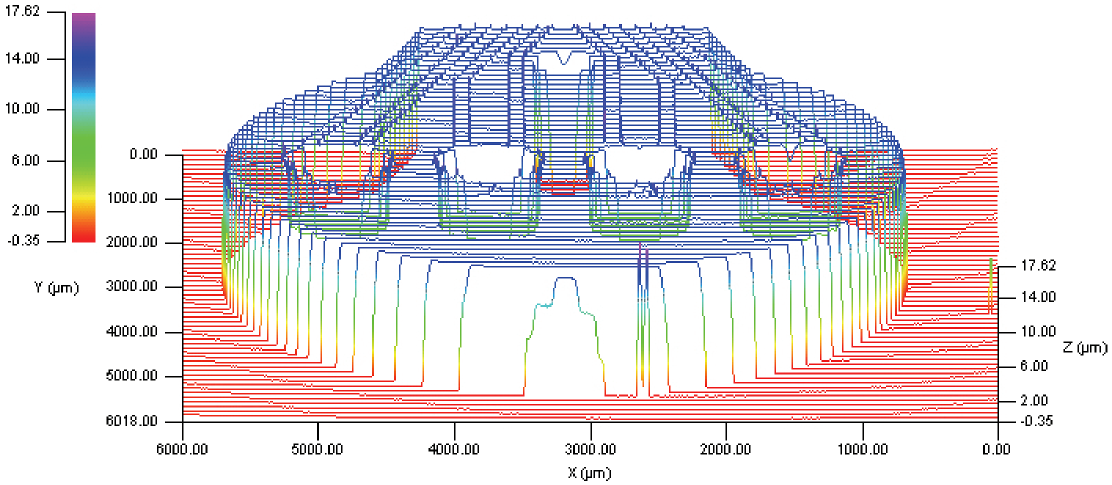

Figure 5-24. Surface profile of retinal aspect of electrode array region of surgical test structure.

Surgical implantation *in vivo* proceeded as follows: an incision approximately 5 to 7 mm long was made in the cornea, followed by an anterior capsulorhexis. The lens was extracted via phacoemulsification. A posterior capsulotomy was made, followed by removal of the vitreous posterior to the lens capsule. The electrode region was threaded under the cornea, through both holes in the capsule, and the RF coil region was then folded, introduced into the lens capsule and then unfolded. Vitrectomy was then performed through scleral ports, and the array region was tacked in place on the retina. Finally, the cornea was sutured closed as well as all the scleral ports. Intraoperative surgical photographs under anterior (a) and intravitreal (b) illumination are shown in Figure 5-25.

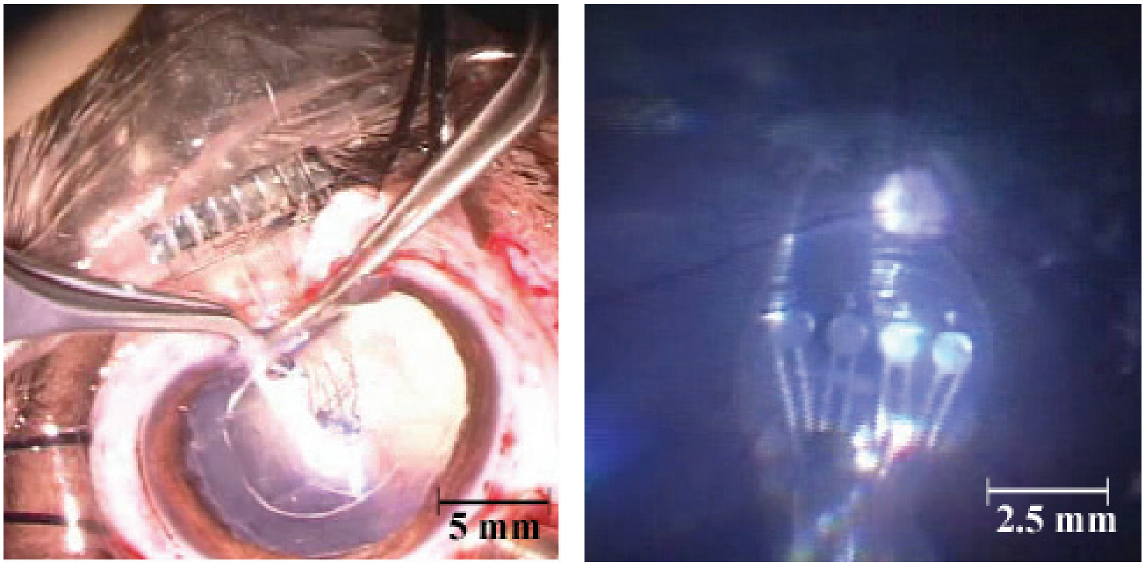

Figure 5-25. Surgical implantation of improved surgical structure under anterior illumination (left) and intravitreal illumination (right).

Upon surgical implantation, it was noted that the design modifications resulted in a better surgical outcome and that the RF coil region showed improved anchoring within the lens capsule. Pad-electrode-pad impedances were measured prior to implantation of this device using the anticipated surgical procedures *ex vivo* in a porcine eye and *in vivo* in a canine eye. After explantation, the eyes were sectioned to evaluate surgical positioning prior to extraction of the array. As shown in Figure 5-26, the array was tacked in place in at the correct retinal location (folds are an artifact from the fixation and sectioning procedure), while the capsular wings showed efficacy in maintaining the RF coil section at the correct location.

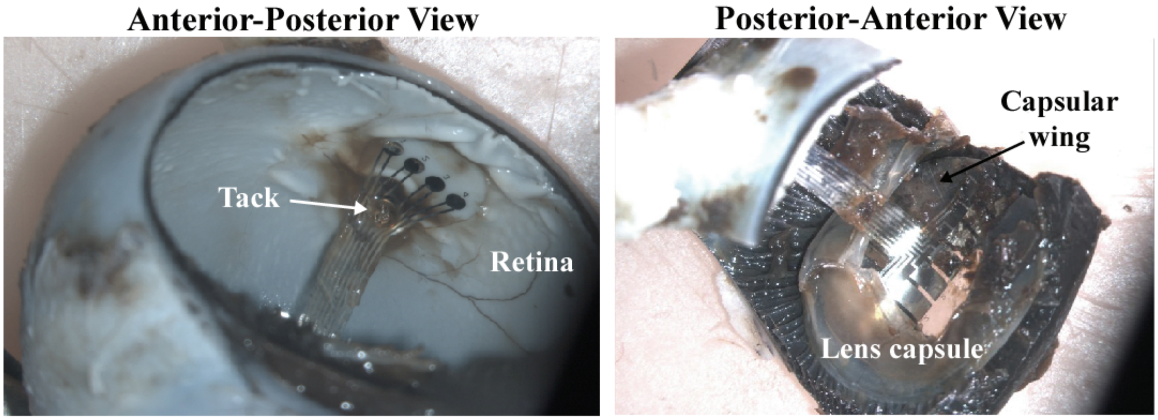

Anterior-Posterior View

Posterior-Anterior View

Figure 5-26. Views of typical array placement after enucleation and before removal for electrical testing. Array region was tacked in the correct location and the capsular wings helped keep the RF coil region in the lens capsule.

Line impedances were measured and compared with those measured prior. For two out of three surgeries using identically fabricated devices from the same run, the results graphed in Figure 5-27 show that the pre-surgical coil-electrode-coil circuit impedances fell into two groups based on the physical lengths of these circuits, the shorter having a mean impedance of 135 Ω and the longer having a mean impedance of 152 Ω. Post-surgical testing of the electrical characteristics of the circuits revealed mean impedances of 136 and 154 Ω for the short and long circuits, respectively, with no lines having been broken during the surgical procedures. Another device was made for a subsequent surgery. In this case, presurgical and post surgical impedances were nearly identical in 7 out of 8 lines. One line was broken during or after surgery. We believe that this is because the tack partially tore through the parylene and a line during implantation or explantation. This, however, could be easily mitigated by better tack handling during surgery or during removal. Nevertheless, these results indicate that the embedded thin-

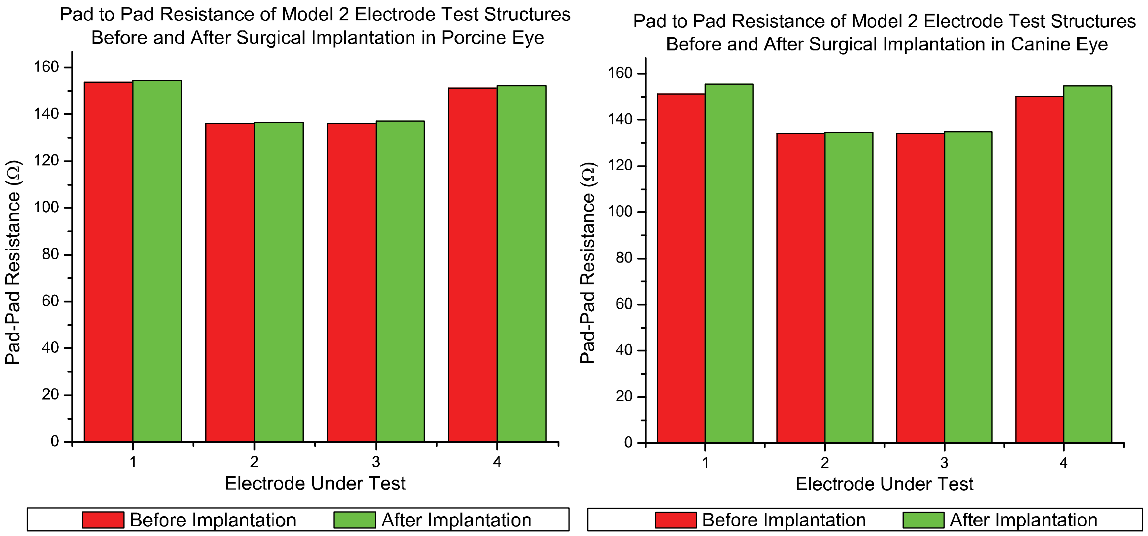

Figure 5-27. Pad-electrode-pad circuit resistances before and after surgical implantation in porcine eye (left) and canine eye (right).

film metal wires are robust under surgical and post-surgical procedures, and point to the utility of the novel surgical design in keeping the RF coil anchored either in the lens capsule or the sulcus while the cable makes its way back to the retina in the final implementation of an all-intraocular system.

5.7 Conclusions

This chapter has described a high-lead-count integration technology that is capable of achieving electrical contacts to prefabricated chips in a highly scalable manner. This means that, for the first time, the direct integration of individual prefabricated ASICs with CMOS compatible MEMS in a flexible, scalable, standard photolithography- and standard microfabrication-limited manner has been shown. This scalability means that our technology is capable of achieving the high lead count required for modern neural prostheses. This work constitutes a ground-breaking, biocompatible, and cost-effective technology for interconnecting prefabricated chips and ASICs with each other, with MEMS devices, and with neural prostheses. The design and processing results for a completely integrated monolithically fabricated device have been presented, work which will continue and be further expounded upon as this project continues. Finally, a novel geometry for an all-intraocular system has been devised and surgically tested, giving preliminary evidence that it is possible to introduce and anchor the relevant components of the full monolithic device in the target regions of the eye in such a way that all the parts are completely implanted and that there is no nidus for infection due to permanent scleral incisions. In addition, it has been shown that thin-film metal lines are robust under real surgical conditions. When combined with the high-lead-count electrode technologies presented in Chapters 3 and 4 and our RF coil technology [81, 134], this packaging technology and implantation scheme complete the suite of technologies and knowledge necessary for both a chronically implantable retinal and spinal cord prosthesis.

6 CONCLUSIONS

BioMEMS, an emerging field in which MEMS are designed, fabricated, and utilized to interface with and examine biological systems, is a discipline replete with incredible possibilities, but also one that is fraught with potential pitfalls. This is no more true than in the case of implantable microelectronics, where applications abound because of the near perfect match in the sizes of the functional components of the body, namely cells and neurons, and the technologies possible using microfabrication techniques, many of which we have discussed in Chapter 2. Materials must be carefully selected such that they are biocompatible with the body, while still enabling maximal functionality to be delivered to the patient, requirements that are often competing in nature. In this vein, the microtechnologies necessary for parylene-based retinal and spinal cord prosthetics have been presented, spurred by a discussion of the clinical problems of retinal and spinal disease in Chapter 1. Flexible microelectrode arrays fabricated of multiple metals and in various geometries have been presented in Chapters 3 and 4 to show both recording and stimulation results in the two neural models, the results of which are extremely promising. Because parylene C and HT are superior to many other polymers in terms of their mechanical, water permeability, and dielectric properties, devices fabricated using these materials as the main substrate are likely to be tolerable for many years in the human body without loss of functionality and without harm to the patient. A high-lead-count packaging scheme has also been presented in Chapter 5, a paradigm which we believe solves the problem of interconnection of such arrays with the driving or recording electronics necessary for their ultimate use. All evidence thus far points to the fact that parylene-based technologies are likely an ideal option for implantable neuroprostheses and microdevices, and the hope is that, soon, these technologies will be implemented in real devices to treat patients with these diseases.

It should be stressed that these technologies are not limited to use in these two groups of disease. In fact, the ability of our flexible arrays to conform to the geometries of interest in the human body enables them to be used in a variety of locations heretofore previously inaccessible with such high precision. Such locations include the surfaces of the cerebral cortex, another area of interest from both a scientific and treatment point of view due to such neurological problems as stroke, epilepsy, and memory loss. Areas of other interest include peripheral nerve and muscle. It is also possible to embed sensors in our arrays, as will likely be done in the near future, to assess mechanical forces placed on the tissues of interest by our arrays as well as to detect extrinsic pressures, such as those within the eye or within blood vessels.

Perhaps understandably, there is a public reticence to the implementation of such technologies in the human body. While such apprehension is not a recent phenomenon, the burgeoning era of computerized special effects in television and cinema has helped fuel the fear that the blending of “man” and “machine” can have devastating consequences. What is missed in such intimations is that, in the hands of ethical doctors, engineers, and other scientists, such consequences are extremely remote. But it is not about the inventors of these technologies, and it should never be about personal glory. All of that slips away the moment one talks to a person who has devoted their life to be a pioneer in the field by volunteering to be a test subject of such devices for the benefit of mankind. In such conversations, one realizes the full potential of this technology. Investigation into these devices not only has the possibility to positively affect the lives of such people, by enabling them to “walk” or “see” again, but it transcends all that by bringing about in all involved a sense of camaraderie. Indeed, the selfless motivation of such individuals who devote their most precious commodity, their body, to such studies, more than anything else highlights our very humanity. It shows that, despite the need for such technological innovation, it is only by working together and for one another that we, as a people, can break the bonds of human disease.

Appendix A: Single-Layer Electrode Array Microfabrication Process

Substrate: Prime silicon wafers, 550 μm thick, 4 inch diameter. Do not remove native oxide.

1) Alignment Marks (Single-Side, Front-Side Only) – Stepper Process Only

1. HMDS prime
    a. 2 mL
    b. Time: 1 minute
2. Spin AZ 4400
    a. Ramp rate: 1 krpm/sec
    b. Spin speed: 4 krpm
    c. Time: 40 seconds
3. Soft bake
    a. Temperature: 100 °C
    b. Time: 30 minutes
4. Expose the alignment marks – UV Cannon
    a. Time: 20 seconds
5. Develop in AZ351 Developer
    a. 3:1 DI H_2O:AZ351
    b. Time: 90 seconds
6. Rinse in DI H_2O
7. Spin dry
8. Examine the alignment marks
9. Etch the alignment marks
    a. Machine: RIE
    b. Plasma type: SF_6/O_2
    c. Plasma Pressure/Power/Time: 120 mTorr/120 W/10 min (Recipe 4)
10. Strip photoresist in ST-22
    a. Temperature: 80 °C
    b. Time: ~ 10 minutes
11. Rinse in Post-Solvent Rinse
12. Rinse in DI H_2O
13. Spin dry
14. Examine the alignment marks

2) Optional Sacrificial Photoresist – Not Suggested

1. Spin AZ 4400
    a. Ramp rate: 1 krpm/sec
    b. Spin speed: 4 krpm
    c. Time: 40 seconds
2. Hard bake

    a. Temperature: 100 °C
    b. Time: 12 hours

3) Deposit Parylene

1. PDS 2010
2. Parylene C: ~10 grams

4) Liftoff

1. Spin LOR3B
    a. Ramp rate: 1 krpm/sec
    b. Spin speed: 3 krpm
    c. Time: 40 seconds
2. Soft bake
    a. Temperature: 190 °C
    b. Time: 10 minutes
3. Spin AZ 1518
    a. Ramp rate: 1 krpm/sec
    b. Spin speed: 3 krpm
    c. Time: 40 seconds
4. Soft bake
    a. Temperature: 100 °C
    b. Time: 30 minutes

5a. Expose the pattern – Stepper
    a. Time: 0.35 seconds
    b. Stitching if necessary (2.5-5 μm overlap)

5b. Expose the pattern – Contact aligner
    a. Time: 25 seconds

6. Develop in AZ351 Developer
    a. 4:1 DI H_2O:AZ351
    b. Time: 1 minute
7. Rinse in DI H_2O
8. Spin dry
9. Examine
10. Hard bake
    a. Temperature: 120 °C
    b. Time: 12 hours
11. Descum
    a. Machine: PEII
    b. Plasma type: O_2
    c. Plasma Pressure/Power/Time: 200 mTorr/50 W/2 min
12. Deposit metal in e-beam
    a. (optional) Ti: 200 Å
    b. Pt: 2000-5000 Å
13. Strip photoresist in ST-22
    a. Temperature: 80 °C
    b. Time: 2 hours

14. Rinse in DI H_2O
15. Spin dry
16. Examine

5) Deposit Parylene

1. PDS 2010
2. Parylene C: ~7 grams

6) Etch Parylene

1. Spin AZ 9260
    a. Ramp rate: 1 krpm/sec
    b. Spin speed: 1 krpm
    c. Time: 40 seconds
2. Soft bake
    a. Temperature: 100 °C
    b. Time: 30 minutes

3a. Expose the electrode and geometry etch pattern – Stepper
    a. Time: 10 seconds
    b. Stitching if necessary (2.5-5 μm overlap)

3b. Expose the electrode and geometry etch pattern – Contact Aligner
    a. Time: 99.9 seconds

4. Develop in AZ351 Developer
    a. 3:1 DI H_2O:AZ351
    b. Time: 5 minutes
5. Rinse in DI H_2O
6. Spin dry
7. Examine
8. Etch Parylene
    a. Machine: RIE
    b. Plasma type: O_2
    c. Plasma Pressure/Power/Time: 350 mTorr/400 W/30 min (Recipe 3)
9. Spin AZ 9260 (no strip)
    a. Ramp rate: 1 krpm/sec
    b. Spin speed: 1 krpm
    c. Time: 40 seconds
10. Soft bake
    a. Temperature: 100 °C
    b. Time: 30 minutes

11a. Expose the geometry etch pattern – Stepper
    a. Time: 10 seconds
    b. Stitching if necessary (2.5-5 μm overlap)

11b. Expose the geometry etch pattern – Contact aligner
    a. Time: 99.9 seconds

12. Develop in AZ351 Developer
    a. 120 mL:55 mL DI H_2O:AZ351
    b. Time: 7 minutes

13. Rinse in DI H_2O
14. Spin dry
15. Examine
16. Etch Parylene
    a. Machine: RIE
    b. Plasma type: O_2
    c. Plasma Pressure/Power/Time: 350 mTorr/400 W/25 min (Recipe 3)
17. Strip photoresist in ST-22
    a. Temperature: 80 °C
    b. Time: 10 minutes
18. Rinse in Post-Solvent Rinse
19. Rinse in DI H_2O
20. Examine

7) Release Devices

1a. If sacrificial photoresist used – not suggested
    a. Soak in acetone for 2 days
    b. Peel
1b. If no sacrificial photoresist used
    a. Place in water bath
    b. Tap edge of array with tweezers and peel
2. Rinse in DI H_2O
3. Examine

8) Anneal for Parylene-Parylene Adhesion

1. Place and clamp in appropriate jig
2. Place in vacuum oven
    a. N_2 backfill at 10 Torr
    b. Temperature: 200 °C
    c. Time: 2 days
3. Vent
4. Examine

Appendix B: Dual-Layer Electrode Array Microfabrication Process

Substrate: Prime silicon wafers, 550 μm thick, 4 inch diameter. Do not remove native oxide.

1) Alignment Marks (Single-Side, Front-Side Only) – Stepper Process Only

1. HMDS prime
    a. 2 mL
    b. Time: 1 minute
2. Spin AZ 4400
    a. Ramp rate: 1 krpm/sec
    b. Spin speed: 4 krpm
    c. Time: 40 seconds
3. Soft bake
    a. Temperature: 100 °C
    b. Time: 30 minutes
4. Expose the alignment marks – UV Cannon
    a. Time: 20 seconds
5. Develop in AZ351 Developer
    a. 3:1 DI H_2O:AZ351
    b. Time: 90 seconds
6. Rinse in DI H_2O
7. Spin dry
8. Examine the alignment marks
9. Etch the alignment marks
    a. Machine: RIE
    b. Plasma type: SF_6/O_2
    c. Plasma Pressure/Power/Time: 120 mTorr/120 W/10 min (Recipe 4)
10. Strip photoresist in ST-22
    a. Temperature: 80 °C
    b. Time: ~ 10 minutes
11. Rinse in Post-Solvent Rinse
12. Rinse in DI H_2O
13. Spin dry
14. Examine the alignment marks

2) Optional Sacrificial Photoresist – Not Suggested

1. Spin AZ 4400
    a. Ramp rate: 1 krpm/sec
    b. Spin speed: 4 krpm
    c. Time: 40 seconds
2. Hard bake

    a. Temperature: 100 °C
    b. Time: 12 hours

3) Deposit Parylene

1. PDS 2010
2. Parylene C: ~8 grams

4) 1st Liftoff

1. Spin LOR3B
    a. Ramp rate: 1 krpm/sec
    b. Spin speed: 3 krpm
    c. Time: 40 seconds
2. Soft bake
    a. Temperature: 190 °C
    b. Time: 10 minutes
3. Spin AZ 1518
    a. Ramp rate: 1 krpm/sec
    b. Spin speed: 3 krpm
    c. Time: 40 seconds
4. Soft bake
    a. Temperature: 100 °C
    b. Time: 30 minutes

5a. Expose the 1st layer pattern – Stepper
    a. Time: 0.35 seconds
    b. Stitching if necessary (2.5-5 µm overlap)

5b. Expose the 1st layer pattern – Contact aligner
    a. Time: 25 seconds

6. Develop in AZ351 Developer
    a. 4:1 DI H_2O:AZ351
    b. Time: 1 minute
7. Rinse in DI H_2O
8. Spin dry
9. Examine
10. Hard bake
    a. Temperature: 120 °C
    b. Time: 12 hours
11. Descum
    a. Machine: PEII
    b. Plasma type: O_2
    c. Plasma Pressure/Power/Time: 200 mTorr/50 W/2 min
12. Deposit metal in e-beam
    a. (optional) Ti: 200 Å
    b. Pt: 2000-5000 Å
13. Strip photoresist in ST-22
    a. Temperature: 80 °C
    b. Time: 2 hours

14. Rinse in DI H_2O
15. Spin dry
16. Examine

5) Deposit Parylene

1. PDS 2010
2. Parylene C: ~2 grams

6) Etch Vias

1. Spin AZ 4400
    a. Ramp rate: 1 krpm/sec
    b. Spin speed: 2 krpm
    c. Time: 40 seconds
2. Soft bake
    a. Temperature: 100 °C
    b. Time: 30 minutes

3a. Expose the via pattern – Stepper
    a. Time: 1.5 seconds
    b. Stitching if necessary (2.5-5 μm overlap)
3b. Expose the via pattern – Contact aligner
    a. Time: 50 seconds

4. Develop in AZ351 Developer
    a. 4:1 DI H_2O:AZ351
    b. Time: 2:30 minutes
5. Rinse in DI H_2O
6. Spin dry
7. Examine
8. Etch Parylene
    a. Machine: RIE
    b. Plasma type: O_2
    c. Plasma Pressure/Power/Time: 350 mTorr/400 W/9 min (Recipe 3)
9. Strip photoresist in ST-22
    a. Temperature: 80 °C
    b. Time: 10 minutes
10. Rinse in Post-Solvent Rinse
11. Rinse in DI H_2O
12. Examine

7) 2nd Liftoff

1. Spin LOR3B
    a. Ramp rate: 1 krpm/sec
    b. Spin speed: 3 krpm
    c. Time: 40 seconds
2. Soft bake
    a. Temperature: 190 °C
    b. Time: 10 minutes

3. Spin AZ 1518
    a. Ramp rate: 1 krpm/sec
    b. Spin speed: 3 krpm
    c. Time: 40 seconds
4. Soft bake
    a. Temperature: 100 °C
    b. Time: 30 minutes
5a. Expose the 2^{nd} layer pattern – Stepper
    a. Time: 0.35 seconds
    b. Stitching if necessary (2.5-5 μm overlap)
5b. Expose the 2^{nd} layer pattern – Contact aligner
    a. Time: 25 seconds
6. Develop in AZ351 Developer
    a. 4:1 DI H_2O:AZ351
    b. Time: 1 minute
7. Rinse in DI H_2O
8. Spin dry
9. Examine
10. Hard bake
    a. Temperature: 120 °C
    b. Time: 12 hours
11. Descum
    a. Machine: PEII
    b. Plasma type: O_2
    c. Plasma Pressure/Power/Time: 200 mTorr/50 W/2 min
12. Deposit metal in e-beam
    a. (optional) Ti: 200 Å
    b. Pt: 2000-5000 Å
13. Strip photoresist in ST-22
    a. Temperature: 80 °C
    b. Time: 2 hours
14. Rinse in DI H_2O
15. Spin dry
16. Examine

8) Deposit Parylene

1. PDS 2010
2. Parylene C: ~7 grams

9) Etch Parylene

1. Spin AZ 9260
    a. Ramp rate: 1 krpm/sec
    b. Spin speed: 1 krpm
    c. Time: 40 seconds
2. Soft bake
    a. Temperature: 100 °C

  - b. Time: 30 minutes
- 3a. Expose the electrode and geometry etch pattern – Stepper
  - a. Time: 10 seconds
  - b. Stitching if necessary (2.5-5 μm overlap)
- 3b. Expose the electrode and geometry etch pattern – Contact aligner
  - a. Time: 99.9 seconds
- 4. Develop in AZ351 Developer
  - a. 3:1 DI H_2O:AZ351
  - b. Time: 5 minutes
- 5. Rinse in DI H_2O
- 6. Spin dry
- 7. Examine
- 8. Etch Parylene
  - a. Machine: RIE
  - b. Plasma type: O_2
  - c. Plasma Pressure/Power/Time: 350 mTorr/400 W/30 min (Recipe 3)
- 9. Spin AZ 9260 (no strip)
  - a. Ramp rate: 1 krpm/sec
  - b. Spin speed: 1 krpm
  - c. Time: 40 seconds
- 10. Soft bake
  - a. Temperature: 100 °C
  - b. Time: 30 minutes
- 11a. Expose the geometry etch pattern – Stepper
  - a. Time: 10 seconds
  - b. Stitching if necessary (2.5-5 μm overlap)
- 11b. Expose the geometry etch pattern – Contact aligner
  - a. Time: 99.9 seconds
- 12. Develop in AZ351 Developer
  - a. 120 mL:55 mL DI H_2O:AZ351
  - b. Time: 7 minutes
- 13. Rinse in DI H_2O
- 14. Spin dry
- 15. Examine
- 16. Etch Parylene
  - a. Machine: RIE
  - b. Plasma type: O_2
  - c. Plasma Pressure/Power/Time: 350 mTorr/400 W/25 min (Recipe 3)
- 17. Strip photoresist in ST-22
  - a. Temperature: 80 °C
  - b. Time: 10 minutes
- 18. Rinse in Post-Solvent Rinse
- 19. Rinse in DI H_2O
- 20. Examine

10) Release Devices

- 1a. If sacrificial photoresist used – not suggested
  - a. Soak in acetone for 2 days
  - b. Peel
- 1b. If no sacrificial photoresist used
  - a. Place in water bath
  - b. Tap edge of array with tweezers and peel
- 2. Rinse in DI H_2O
- 3. Examine

11) Anneal for Parylene-Parylene Adhesion

- 1. Place and clamp in appropriate jig
- 2. Place in vacuum oven
  - a. N_2 backfill at 10 Torr
  - b. Temperature: 200 °C
  - c. Time: 2 days
- 3. Vent
- 4. Examine

Appendix C: Parylene HT Iridium Electrode Array Microfabrication Process

Substrate: Prime silicon wafers, 550 μm thick, 4 inch diameter. Do not remove native oxide.

1) Alignment Marks (Single-Side, Front-Side Only) – Stepper Process Only

1. HMDS prime
    a. 2 mL
    b. Time: 1 minute
2. Spin AZ 4400
    a. Ramp rate: 1 krpm/sec
    b. Spin speed: 4 krpm
    c. Time: 40 seconds
3. Soft bake
    a. Temperature: 100 °C
    b. Time: 30 minutes
4. Expose the alignment marks – UV Cannon
    a. Time: 20 seconds
5. Develop in AZ351 Developer
    a. 3:1 DI H_2O:AZ351
    b. Time: 90 seconds
6. Rinse in DI H_2O
7. Spin dry
8. Examine the alignment marks
9. Etch the alignment marks
    a. Machine: RIE
    b. Plasma type: SF_6/O_2
    c. Plasma Pressure/Power/Time: 120 mTorr/120 W/10 min (Recipe 4)
10. Strip photoresist in ST-22
    a. Temperature: 80 °C
    b. Time: ~ 10 minutes
11. Rinse in Post-Solvent Rinse
12. Rinse in DI H_2O
13. Spin dry
14. Examine the alignment marks

2) Optional Sacrificial Photoresist – Not Suggested

1. Spin AZ 4400
    a. Ramp rate: 1 krpm/sec
    b. Spin speed: 4 krpm
    c. Time: 40 seconds
2. Hard bake

    a. Temperature: 100 °C
    b. Time: 12 hours

3) Deposit Parylene

1. PDS 2035
2. Parylene C: ~6 grams
3. Parylene HT: ~23 grams

4) Liftoff

1. Spin LOR3B
    a. Ramp rate: 1 krpm/sec
    b. Spin speed: 3 krpm
    c. Time: 40 seconds
2. Soft bake
    a. Temperature: 190 °C
    b. Time: 10 minutes
3. Spin AZ 1518
    a. Ramp rate: 1 krpm/sec
    b. Spin speed: 3 krpm
    c. Time: 40 seconds
4. Soft bake
    a. Temperature: 100 °C
    b. Time: 30 minutes

5a. Expose the pattern – Stepper
    a. Time: 0.35 seconds
    b. Stitching if necessary (2.5-5 µm overlap)

5b. Expose the pattern – Contact aligner
    a. Time: 25 seconds

6. Develop in AZ351 Developer
    a. 4:1 DI H_2O:AZ351
    b. Time: 1 minute
7. Rinse in DI H_2O
8. Spin dry
9. Examine
10. Hard bake
    a. Temperature: 120 °C
    b. Time: 12 hours
11. Descum
    a. Machine: PEII
    b. Plasma type: O_2
    c. Plasma Pressure/Power/Time: 200 mTorr/50 W/2 min
12. Deposit metal in e-beam
    a. Ir: 800 Å
13. Strip photoresist in ST-22
    a. Temperature: 80 °C
    b. Time: 2 hours

14. Rinse in DI H_2O
15. Spin dry
16. Examine
17. If necessary
    a. 5 min ultrasonic rinse in n-methyl-2-pyrrolidone
    b. H_2O rinse

5) Deposit Parylene

1. PDS 2035

2a. Parylene HT: ~23 grams

2b. Or perhaps next time do parylene C: ~15 grams

6) Etch Parylene

1. Spin AZ 9260
    a. Ramp rate: 1 krpm/sec
    b. Spin speed: 1 krpm
    c. Time: 40 seconds
2. Soft bake
    a. Temperature: 100 °C
    b. Time: 30 minutes

3a. Expose the electrode and geometry etch pattern – Stepper
    a. Time: 10 seconds
    b. Stitching if necessary (2.5-5 µm overlap)

3b. Expose the electrode and geometry etch pattern – Contact aligner
    a. Time: 99.9 seconds

4. Develop in AZ351 Developer
    a. 3:1 DI H_2O:AZ351
    b. Time: 5 minutes
5. Rinse in DI H_2O
6. Spin dry
7. Examine
8. Etch Parylene
    a. Machine: RIE
    b. Plasma type: O_2
    c. Plasma Pressure/Power/Time: 350 mTorr/400 W/30 min (Recipe 3)
9. Spin AZ 9260 (no strip)
    a. Ramp rate: 1 krpm/sec
    b. Spin speed: 1 krpm
    c. Time: 40 seconds
10. Soft bake
    a. Temperature: 100 °C
    b. Time: 30 minutes

11a. Expose the geometry etch pattern – Stepper
    a. Time: 10 seconds
    b. Stitching if necessary (2.5-5 µm overlap)

11b. Expose the geometry etch pattern – Contact aligner

    a. Time: 99.9 seconds
12. Develop in AZ351 Developer
    a. 120 mL:55 mL DI H_2O:AZ351
    b. Time: 7 minutes
13. Rinse in DI H_2O
14. Spin dry
15. Examine
16. Etch Parylene
    a. Machine: RIE
    b. Plasma type: O_2
    c. Plasma Pressure/Power/Time: 350 mTorr/400 W/25 min (Recipe 3)
17. Strip photoresist in ST-22
    a. Temperature: 80 °C
    b. Time: 10 minutes
18. Rinse in Post-Solvent Rinse
19. Rinse in DI H_2O
20. Examine

7) Release Devices

1a. If sacrificial photoresist used – not suggested
    a. Soak in acetone for 2 days
    b. Peel
1b. If no sacrificial photoresist used
    a. Place in water bath
    b. Tap edge of array with tweezers and peel
2. Rinse in DI H_2O
3. Examine

8) Anneal for Parylene-Parylene Adhesion

1. Place and clamp in appropriate jig
2. Place in vacuum oven
    a. N_2 backfill at 10 Torr
    b. Temperature: 200 °C
    c. Time: 2 days
3. Vent
4. Examine

Appendix D: CL-I^2 Microfabrication Process

Substrate: Prime silicon wafers, 550 μm thick, 4 inch diameter. Do not remove native oxide.

1) Alignment Marks (Single-Side, Front-Side Only)

1. HMDS prime
    a. 2 mL
    b. Time: 1 minute
2. Spin AZ 4400
    a. Ramp rate: 1 krpm/sec
    b. Spin speed: 4 krpm
    c. Time: 40 seconds
3. Soft bake
    a. Temperature: 100 °C
    b. Time: 30 minutes
4. Expose the alignment marks – UV Cannon
    a. Time: 20 seconds
5. Develop in AZ351 Developer
    a. 3:1 DI H_2O:AZ351
    b. Time: 90 seconds
6. Rinse in DI H_2O
7. Spin dry
8. Examine the alignment marks
9. Etch the alignment marks
    a. Machine: RIE
    b. Plasma type: SF_6/O_2
    c. Plasma Pressure/Power/Time: 120 mTorr/120 W/10 min (Recipe 4)
10. Strip photoresist in ST-22
    a. Temperature: 80 °C
    b. Time: ~ 10 minutes
11. Rinse in Post-Solvent Rinse
12. Rinse in DI H_2O
13. Spin dry
14. Examine the alignment marks

2) Etch Chip Cavities

1. Spin AZ 9260
    a. Ramp rate: 1 krpm/sec
    b. Spin speed: 1 krpm
    c. Time: 40 seconds
2. Soft bake
    a. Temperature: 100 °C
    b. Time: 30 minutes

3. Expose the pattern – Stepper
    a. Time: 10 seconds
4. Develop in AZ351 Developer
    a. 3:1 DI H_2O:AZ351
    b. Time: 5 minutes
5. Rinse in DI H_2O
6. Spin dry
7. Examine
8. Remove photoresist ring
9. Attach to backside wafer with several drops of 1518
10. DRIE etch with B=7 seconds process
    a. 700 loops
11. Strip photoresist and remove backside wafer in ST-22
    a. Temperature: 80 °C
    b. Time: 2 hours

3) Seal Chips in Wafer

1. Place Nitto tape on front side
2. Place chips in from back side
3. Paint thick layer of 9260 on back side
4. Bake
    a. Temperature: 100 °C
    b. Time: 60 minutes
5. Deposit parylene
    a. PDS 2035
    b. Parylene C: ~20 grams → can be more
6. Peel off Nitto tape
7. Profile surface in profilometer

From this point forward, try to avoid using vacuum chuck

4) Sacrificial Photoresist – May Be Optional

1. Spin AZ 4400
    a. Ramp rate: 1 krpm/sec
    b. Spin speed: 4 krpm
    c. Time: 40 seconds
2. Soft bake
    a. Temperature: 100 °C
    b. Time: 30 minutes
3. Expose the surface of the chip – Stepper
    a. Time: 1 second
4. Develop in AZ351 Developer
    a. 3:1 DI H_2O:AZ351
    b. Time: 2 minutes
5. Rinse in DI H_2O
6. Spin dry

7. Examine
8. Hard bake
    a. Temperature: 100 °C
    b. Time: 1 hour

5) Deposit Parylene

1. PDS 2010
2. Parylene C: ~5.5 grams
3. Profile surface in profilometer

6) Etch Vias

1. Spin AZ 9260
    a. Ramp rate: 1 krpm/sec
    b. Spin speed: 3 krpm
    c. Time: 40 seconds
2. Soft bake
    a. Temperature: 100 °C
    b. Time: 30 minutes
3. Expose the via pattern – Stepper
    a. Time: 4.5 seconds
4. Develop in AZ351 Developer
    a. 3:1 DI H_2O:AZ351
    b. Time: 4 minutes
5. Rinse in DI H_2O
6. Spin dry
7. Examine
8. Etch Parylene
    a. Machine: RIE
    b. Plasma type: O_2
    c. Plasma Pressure/Power/Time: 350 mTorr/400 W/11 min (Recipe 3)
9. Strip photoresist in ST-22
    a. Temperature: 80 °C
    b. Time: 5 minutes
10. Rinse in Post-Solvent Rinse
11. Rinse in DI H_2O
12. Examine

7) Deposit Metal

1. Deposit metal in e-beam
    a. Ti: 200 Å
    b. Au: 2000 Å

8) Etch Metal

1. Spin AZ 9260
    a. Ramp rate: 1 krpm/sec
    b. Spin speed: 3 krpm

    - c. Time: 40 seconds
2. Soft bake
    - a. Temperature: 100 °C
    - b. Time: 30 minutes
3. Expose the metal pattern – Stepper
    - a. Time: 4.5 seconds
    - b. Stitching if necessary (2.5-5 µm overlap)
    - c. Flood expose surrounding die
4. Develop in AZ351 Developer
    - a. 3:1 DI H_2O:AZ351
    - b. Time: 4 minutes
5. Rinse in DI H_2O
6. Spin dry
7. Examine
8. Wet etch
    - a. Au etch (1 minute)
    - b. Ti etch (BHF for 20 seconds; or 10:10:200 HF:H_2O_2:H_2O for 4 seconds)
    - c. Rinse in DI H_2O
    - d. Spin dry
    - e. Examine
9. Flood expose in UV cannon
    - a. 10 seconds
10. Strip in straight AZ351 Developer
    - a. 2 minutes
11. Rinse in DI H_2O
12. Spin dry
13. Examine
14. Test for contact on probe station

9) Deposit Parylene

1. PDS 2010
2. Parylene C: ~10-15 grams

10) Etch Parylene

1. Spin AZ 9260
    - a. Ramp rate: 1 krpm/sec
    - b. Spin speed: 1 krpm
    - c. Time: 40 seconds
2. Soft bake
    - a. Temperature: 100 °C
    - b. Time: 30 minutes
3. Expose the electrode and geometry etch pattern – Stepper
    - a. Time: 10 seconds
    - b. Stitching if necessary (2.5-5 µm overlap)
4. Develop in AZ351 Developer

    - a. 3:1 DI H_2O:AZ351
    - b. Time: 5 minutes
- 5. Rinse in DI H_2O
- 6. Spin dry
- 7. Examine
- 8. Etch Parylene
    - a. Machine: RIE
    - b. Plasma type: O_2
    - c. Plasma Pressure/Power/Time: 350 mTorr/400 W/30 min (Recipe 3)
- 9. Spin AZ 9260 (no strip)
    - a. Ramp rate: 1 krpm/sec
    - b. Spin speed: 1 krpm
    - c. Time: 40 seconds
- 10. Soft bake
    - a. Temperature: 100 °C
    - b. Time: 30 minutes
- 11. Expose the geometry etch pattern – Stepper
    - a. Time: 10 seconds
    - b. Stitching if necessary (2.5-5 μm overlap)
- 12. Develop in AZ351 Developer
    - a. 120 mL:55 mL DI H_2O:AZ351
    - b. Time: 7 minutes
- 13. Rinse in DI H_2O
- 14. Spin dry
- 15. Examine
- 16. Etch Parylene
    - a. Machine: RIE
    - b. Plasma type: O_2
    - c. Plasma Pressure/Power/Time: 350 mTorr/400 W/30 min (Recipe 3)
- 17. Strip photoresist in ST-22
    - a. Temperature: 80 °C
    - b. Time: 10 minutes
- 18. Rinse in Post-Solvent Rinse
- 19. Rinse in DI H_2O
- 20. Examine

11) Release Devices

- 1. Remove sacrificial photoresist
    - a. Poke holes over chips on backside
    - b. Soak in acetone for 2 days
    - c. Peel
- 2. Rinse in DI H_2O
- 3. Examine

12) Anneal for Parylene-Parylene Adhesion

1. Place and clamp in appropriate jig
2. Place in vacuum oven
    a. N_2 backfill at 10 Torr
    b. Temperature: 200 °C
    c. Time: 2 days
3. Vent
4. Examine

Appendix E: Proposed Monolithic Prosthesis Microfabrication Process

Substrate: Prime silicon wafers, 550 µm thick, 4 inch diameter. Do not remove native oxide.

1) Alignment Marks (Single-Side, Front-Side Only)

1. HMDS prime
    a. 2 mL
    b. Time: 1 minute
2. Spin AZ 4400
    a. Ramp rate: 1 krpm/sec
    b. Spin speed: 4 krpm
    c. Time: 40 seconds
3. Soft bake
    a. Temperature: 100 °C
    b. Time: 30 minutes
4. Expose the alignment marks – UV Cannon
    a. Time: 20 seconds
5. Develop in AZ351 Developer
    a. 3:1 DI H_2O:AZ351
    b. Time: 90 seconds
6. Rinse in DI H_2O
7. Spin dry
8. Examine the alignment marks
9. Etch the alignment marks
    a. Machine: RIE
    b. Plasma type: SF_6/O_2
    c. Plasma Pressure/Power/Time: 120 mTorr/120 W/10 min (Recipe 4)
10. Strip photoresist in ST-22
    a. Temperature: 80 °C
    b. Time: ~ 10 minutes
11. Rinse in Post-Solvent Rinse
12. Rinse in DI H_2O
13. Spin dry
14. Examine the alignment marks

2) Sacrificial Photoresist – May Be Optional

1. Spin AZ 4400
    a. Ramp rate: 1 krpm/sec
    b. Spin speed: 4 krpm
    c. Time: 40 seconds
2. Hard bake

    - a. Temperature: 100 °C
    - b. Time: 1 hour

3) Deposit Parylene

1. PDS 2035
2. Parylene C: ~17 grams → 7 μm

4) Deposit Metal

1. Deposit metal in e-beam
    - a. Ti: 200 Å
    - b. Au: 5000 Å

5) Etch Metal

1. Spin AZ 1518
    - a. Ramp rate: 1 krpm/sec
    - b. Spin speed: 3 krpm
    - c. Time: 40 seconds
2. Soft bake
    - a. Temperature: 100 °C
    - b. Time: 30 minutes
3. Expose the metal pattern – Stepper
    - a. Time: 0.7 seconds
    - b. Stitching if necessary (2.5-5 μm overlap)
    - c. Flood expose surrounding die, neighboring electrode region, and alignment marks
    - d. DCR5;ALIGN,ELEC,COIL (Blank Frame,Blank Frame,First Metal Layer)
4. Develop in AZ351 Developer
    - a. 4:1 DI H_2O:AZ351
    - b. Time: 2 minutes
5. Rinse in DI H_2O
6. Spin dry
7. Examine
8. Wet etch
    - a. Au etch (2 minutes)
    - b. Ti etch (BHF for 20 seconds)
    - c. Rinse in DI H_2O
    - d. Spin dry
    - e. Examine
9. Strip photoresist in ST-22
    - a. Temperature: 80 °C
    - b. Time: 5 minutes

11. Rinse in Post-Solvent Rinse
12. Rinse in DI H_2O
13. Spin dry
14. Examine

6) Deposit Parylene

1. PDS 2035
2. Parylene C: ~3 grams → 1.5 µm

7) Etch Vias

1. Spin AZ 9260
    a. Ramp rate: 1 krpm/sec
    b. Spin speed: 3 krpm
    c. Time: 40 seconds
2. Soft bake
    a. Temperature: 100 °C
    b. Time: 30 minutes
3. Expose the via 1 pattern – Stepper
    a. Time: 7 seconds
    b. DCR5;COIL
4. Develop in AZ351 Developer
    a. 3:1 DI H_2O:AZ351
    b. Time: 6 minutes
5. Rinse in DI H_2O
6. Spin dry
7. Examine
8. Etch Parylene
    a. Machine: RIE
    b. Plasma type: O_2
    c. Plasma Pressure/Power/Time: 350 mTorr/400 W/7 min (Recipe 3)
9. Strip photoresist in ST-22
    a. Temperature: 80 °C
    b. Time: 5 minutes
10. Rinse in Post-Solvent Rinse
11. Rinse in DI H_2O
12. Examine

8) Deposit Metal

1. Deposit metal in e-beam
    a. Ti: 200 Å
    b. Au: 5000 Å

9) Etch Metal

1. Spin AZ 1518
    a. Ramp rate: 1 krpm/sec
    b. Spin speed: 3 krpm
    c. Time: 40 seconds
2. Soft bake
    a. Temperature: 100 °C
    b. Time: 30 minutes

3. Expose the metal pattern – Stepper
    a. Time: 0.7 seconds
    b. Stitching if necessary (2.5-5 μm overlap)
    c. Flood expose surrounding die, neighboring electrode region, and alignment marks
    d. DCR5;ALIGN,ELEC,COIL (Blank Frame,Blank Frame,Second Metal Layer)
4. Develop in AZ351 Developer
    a. 4:1 DI H_2O:AZ351
    b. Time: 2 minutes
5. Rinse in DI H_2O
6. Spin dry
7. Examine
8. Wet etch
    a. Au etch (2 minutes)
    b. Ti etch (BHF for 20 seconds)
    c. Rinse in DI H_2O
    d. Spin dry
    e. Examine
9. Strip photoresist in ST-22
    a. Temperature: 80 °C
    b. Time: 5 minutes
11. Rinse in Post-Solvent Rinse
12. Rinse in DI H_2O
13. Spin dry
14. Examine

10) Deposit Parylene

1. PDS 2035
2. Parylene C: ~3 grams → 1.5 μm

11) Etch Vias

1. Spin AZ 9260
    a. Ramp rate: 1 krpm/sec
    b. Spin speed: 3 krpm
    c. Time: 40 seconds
2. Soft bake
    a. Temperature: 100 °C
    b. Time: 30 minutes
3. Expose the via 2 pattern – Stepper
    c. Time: 7 seconds
    d. DCR5;COIL
4. Develop in AZ351 Developer
    a. 3:1 DI H_2O:AZ351
    b. Time: 6 minutes
5. Rinse in DI H_2O

6. Spin dry
7. Examine
8. Etch Parylene
    a. Machine: RIE
    b. Plasma type: O_2
    c. Plasma Pressure/Power/Time: 350 mTorr/400 W/12 min (Recipe 3)
9. Strip photoresist in ST-22
    a. Temperature: 80 °C
    b. Time: 5 minutes
10. Rinse in Post-Solvent Rinse
11. Rinse in DI H_2O
12. Examine

12) Deposit Metal

1. Deposit metal in e-beam
    a. Ti: 200 Å
    b. Au: 5000 Å

13) Etch Metal

1. Spin AZ 1518
    a. Ramp rate: 1 krpm/sec
    b. Spin speed: 3 krpm
    c. Time: 40 seconds
2. Soft bake
    a. Temperature: 100 °C
    b. Time: 30 minutes
3. Expose the metal pattern – Stepper
    a. Time: 0.7 seconds
    b. Stitching if necessary (2.5-5 µm overlap)
    c. Flood expose surrounding die, neighboring electrode region, and alignment marks
    d. DCR5;ALIGN,ELEC,COIL (Blank Frame,Blank Frame,Third Metal Layer)
4. Develop in AZ351 Developer
    a. 4:1 DI H_2O:AZ351
    b. Time: 2 minutes
5. Rinse in DI H_2O
6. Spin dry
7. Examine
8. Wet etch
    a. Au etch (2 minutes)
    b. Ti etch (BHF for 20 seconds)
    c. Rinse in DI H_2O
    d. Spin dry
    e. Examine
9. Strip photoresist in ST-22

    - a. Temperature: 80 °C
    - b. Time: 5 minutes
11. Rinse in Post-Solvent Rinse
12. Rinse in DI H_2O
13. Spin dry
14. Examine

14) Deposit Parylene

1. PDS 2035
2. Parylene C: ~6 grams → 3 μm

15) Etch Parylene

1. Spin AZ 9260
    - a. Ramp rate: 1 krpm/sec
    - b. Spin speed: 1 krpm
    - c. Time: 40 seconds
2. Soft bake
    - a. Temperature: 100 °C
    - b. Time: 30 minutes
3. Expose the Chip Cavity Etch – Stepper
    - a. Time: 10 seconds
    - b. DCR5;ELEC (Cap/Chip Cavity Etch)
4. Develop in AZ351 Developer
    - a. 3:1 DI H_2O:AZ351
    - b. Time: 5 minutes
5. Rinse in DI H_2O
6. Spin dry
7. Examine
8. Etch Parylene
    - a. Machine: RIE
    - b. Plasma type: O_2
    - c. Plasma Pressure/Power/Time: 350 mTorr/400 W/30 min (Recipe 3)
9. Spin AZ 9260 (no strip)
    - a. Ramp rate: 1 krpm/sec
    - b. Spin speed: 1 krpm
    - c. Time: 40 seconds
10. Soft bake
    - a. Temperature: 100 °C
    - b. Time: 30 minutes
11. Expose the Chip Cavity Etch – Stepper
    - a. Time: 10 seconds
    - b. DCR5;ELEC (Cap/Chip Cavity Etch)
12. Develop in AZ351 Developer
    - a. 120 mL:55 mL DI H_2O:AZ351
    - b. Time: 7 minutes
13. Rinse in DI H_2O

14. Spin dry
15. Examine
16. Etch Parylene
    a. Machine: RIE
    b. Plasma type: O_2
    c. Plasma Pressure/Power/Time: 350 mTorr/400 W/30 min or until done (Recipe 3)
17. Examine

16) Etch Chip Cavities

1. Spin AZ 9260 (no strip)
    a. Ramp rate: 1 krpm/sec
    b. Spin speed: 1 krpm
    c. Time: 40 seconds
2. Soft bake
    a. Temperature: 100 °C
    b. Time: 30 minutes
3. Expose the pattern – Stepper
    a. Time: 10 seconds
    b. DCR5;ELEC (Cap/Chip Cavity Etch)
4. Develop in AZ351 Developer
    a. 3:1 DI H_2O:AZ351
    b. Time: 5 minutes
5. Rinse in DI H_2O
6. Spin dry
7. Examine
8. Remove photoresist ring
9. Attach to backside wafer with several drops of 1518
10. DRIE etch with B=7 seconds process
    a. 700 loops
11. Strip photoresist and remove backside wafer in ST-22
    a. Temperature: 80 °C
    b. Time: 2 hours

17) Seal Chips in Wafer

1. Place Nitto tape on front side
2. Place chips in from back side
3. Paint thick layer of 9260 on back side
4. Bake
    a. Temperature: 100 °C
    b. Time: 60 minutes
5. Deposit parylene
    a. PDS 2035
    b. Parylene C: ~20 grams → can be more
6. Peel off Nitto tape
7. Profile surface in profilometer

From this point forward, try to avoid using vacuum chuck

18) Deposit Parylene

1. PDS 2035
2. Parylene C: ~3 grams → 1.5 μm
3. Profile surface in profilometer

19) Etch Vias

1. Spin AZ 9260
    a. Ramp rate: 1 krpm/sec
    b. Spin speed: 3 krpm
    c. Time: 40 seconds
2. Soft bake
    a. Temperature: 100 °C
    b. Time: 30 minutes
3. Expose the Coil and Chip Contact pattern – Stepper
    a. Time: 7 seconds
    b. DCR5;COIL,ELEC (Coil Contact Vias,Cap/Chip Contact Etch)
4. Develop in AZ351 Developer
    a. 3:1 DI H_2O:AZ351
    b. Time: 6 minutes
5. Rinse in DI H_2O
6. Spin dry
7. Examine
8. Etch Parylene
    a. Machine: RIE
    b. Plasma type: O_2
    c. Plasma Pressure/Power/Time: 350 mTorr/400 W/7 min (Recipe 3)
9. Strip photoresist in ST-22
    a. Temperature: 80 °C
    b. Time: 5 minutes
10. Rinse in Post-Solvent Rinse
11. Rinse in DI H_2O
12. Examine

20) Liftoff

1. Spin LOR3B
    a. Ramp rate: 1 krpm/sec
    b. Spin speed: 3 krpm
    c. Time: 40 seconds
2. Soft bake
    a. Temperature: 190 °C
    b. Time: 10 minutes
3. Spin AZ 1518
    a. Ramp rate: 1 krpm/sec

   b. Spin speed: 3 krpm
   c. Time: 40 seconds
4. Soft bake
   a. Temperature: 100 °C
   b. Time: 30 minutes
5. Expose the liftoff layer pattern – Stepper
   a. Time: 0.35 seconds
   b. DCR5;COIL,ELEC (Metal Liftoff,Metal Liftoff)
6. Develop in AZ351 Developer
   a. 4:1 DI H_2O:AZ351
   b. Time: 1 minute
7. Rinse in DI H_2O
8. Spin dry
9. Examine
10. Hard bake
    a. Temperature: 120 °C
    b. Time: 12 hours
11. Descum
    a. Machine: PEII
    b. Plasma type: O_2
    c. Plasma Pressure/Power/Time: 200 mTorr/50 W/2 min
12. Deposit metal in e-beam
    a. (optional) Ti: 200 Å
    b. Pt: 2000-5000 Å
13. Strip photoresist in ST-22
    a. Temperature: 80 °C
    b. Time: 2 hours
14. Rinse in DI H_2O
15. Spin dry
16. Examine

21) Deposit Parylene

1. PDS 2010
2. Parylene C: ~7 grams

22) Etch Parylene

1. Spin AZ 9260
   a. Ramp rate: 1 krpm/sec
   b. Spin speed: 1 krpm
   c. Time: 40 seconds
2. Soft bake
   a. Temperature: 100 °C
   b. Time: 30 minutes
3. Expose the electrode and geometry etch pattern – Stepper
   a. Time: 10 seconds

    - b. DCR5;ELEC,ELEC,ELEC,COIL (Electrode Opening Etch,Probe Opening Etch,Parylene Etch 2, Parylene Etch 2)
4. Develop in AZ351 Developer
    - a. 3:1 DI H_2O:AZ351
    - b. Time: 5 minutes
5. Rinse in DI H_2O
6. Spin dry
7. Examine
8. Etch Parylene
    - a. Machine: RIE
    - b. Plasma type: O_2
    - c. Plasma Pressure/Power/Time: 350 mTorr/400 W/30 min (Recipe 3)
9. Spin AZ 9260 (no strip)
    - a. Ramp rate: 1 krpm/sec
    - b. Spin speed: 1 krpm
    - c. Time: 40 seconds
10. Soft bake
    - a. Temperature: 100 °C
    - b. Time: 30 minutes
11. Expose the geometry etch pattern – Stepper
    - a. Time: 10 seconds
    - b. DCR5; ELEC,COIL (Parylene Etch 2, Parylene Etch 2)
12. Develop in AZ351 Developer
    - a. 120 mL:55 mL DI H_2O:AZ351
    - b. Time: 7 minutes
13. Rinse in DI H_2O
14. Spin dry
15. Examine
16. Etch Parylene
    - a. Machine: RIE
    - b. Plasma type: O_2
    - c. Plasma Pressure/Power/Time: 350 mTorr/400 W/30 min (Recipe 3)
17. Strip photoresist in ST-22
    - a. Temperature: 80 °C
    - b. Time: 10 minutes
18. Rinse in Post-Solvent Rinse
19. Rinse in DI H_2O
20. Examine

23) Release Devices

1. Remove sacrificial photoresist
    - a. Poke holes over chips on backside
    - b. Soak in acetone for 2 days
    - c. Peel
2. Rinse in DI H_2O
3. Examine

24) Anneal for Parylene-Parylene Adhesion

1. Place and clamp in appropriate jig
2. Place in vacuum oven
   a. N_2 backfill at 10 Torr
   b. Temperature: 200 °C
   c. Time: 2 days
3. Vent
4. Examine

References

[1] Washington University School of Medicine, "Eye and retina," http://thalamus.wustl.edu/course/eyeret.html (accessed: Jul 6, 2007).

[2] World Health Organization, "Magnitude and causes of visual impairment: Fact sheet n°282," http://www.who.int/mediacentre/factsheets/fs282/en/ (accessed: Jul 6, 2007).

[3] The Eye Diseases Prevalence Research Group, "Prevalence of age-related macular degeneration in the United States," *Archives of Ophthalmology,* vol. 122 (4), pp. 564-572, Apr 1, 2004.

[4] G. Fishman, V. Vasquez, M. Fishman, and D. Berger, "Visual loss and foveal lesions in Usher's syndrome," *British Journal of Ophthalmolology,* vol. 63 (7), pp. 484-488, Jul 1, 1979.

[5] B. W. Jones, C. B. Watt, J. M. Frederick, W. Baehr, C.-K. Chen, E. M. Levine, A. H. Milam, M. M. Lavail, and R. E. Marc, "Retinal remodeling triggered by photoreceptor degenerations," *The Journal of Comparative Neurology,* vol. 464 (1), pp. 1-16, 2003.

[6] E. Margalit and S. R. Sadda, "Retinal and optic nerve diseases," *Artificial Organs,* vol. 27 (11), pp. 963-974, 2003.

[7] A. Santos, M. S. Humayun, E. de Juan, Jr., R. J. Greenburg, M. J. Marsh, I. B. Klock, and A. H. Milam, "Preservation of the inner retina in retinitis pigmentosa. A morphometric analysis," *Archives of Ophthalmology,* vol. 115 (4), pp. 511-515, Apr 1, 1997.

[8] R. E. MacLaren, R. A. Pearson, A. MacNeil, R. H. Douglas, T. E. Salt, M. Akimoto, A. Swaroop, J. C. Sowden, and R. R. Ali, "Retinal repair by transplantation of photoreceptor precursors," *Nature,* vol. 444 (7116), pp. 203-207, 2006.

[9] M. Humayun, R. Propst, E. de Juan, Jr., K. McCormick, and D. Hickingbotham, "Bipolar surface electrical stimulation of the vertebrate retina," *Archives of Ophthalmology,* vol. 112 (1), pp. 110-116, Jan 1, 1994.

[10] M. S. Humayun, E. de Juan, Jr., G. Dagnelie, R. J. Greenberg, R. H. Propst, and D. H. Phillips, "Visual perception elicited by electrical stimulation of retina in blind humans," *Archives of Ophthalmology,* vol. 114 (1), pp. 40-46, Jan 1, 1996.

[11] M. A. Schiefer and W. M. Grill, "Sites of neuronal excitation by epiretinal electrical stimulation," *IEEE Transactions on Neural Systems and Rehabilitation Engineering,* vol. 14 (1), pp. 5-13, 2006.

[12] A. Y. Chow and V. Y. Chow, "Subretinal electrical stimulation of the rabbit retina," *Neuroscience Letters,* vol. 225 (1), pp. 13-16, Mar 28, 1997.

[13] C. Veraart, M. C. Wanet-Defalque, B. Gerard, A. Vanlierde, and J. Delbeke, "Pattern recognition with the optic nerve visual prosthesis," *Artificial Organs,* vol. 27 (11), pp. 996-1004, Nov, 2003.

[14] E. M. Schmidt, M. J. Bak, F. T. Hambrecht, C. V. Kufta, D. K. ORourke, and P. Vallabhanath, "Feasibility of a visual prosthesis for the blind based on intracortical microstimulation of the visual cortex," *Brain,* vol. 119, pp. 507-522, Apr, 1996.

[15] E. M. Maynard, "Visual prostheses," *Annual Review of Biomedical Engineering,* vol. 3 (1), pp. 145-168, 2001.

[16] J. S. Pezaris and R. C. Reid, "Demonstration of artificial visual percepts generated through thalamic microstimulation," *PNAS,* vol. 104 (18), pp. 7670-7675, May 1, 2007.

[17] M. C. Peterman, J. Noolandi, M. S. Blumenkranz, and H. A. Fishman, "Localized chemical release from an artificial synapse chip," *PNAS,* vol. 101 (27), pp. 9951-4, Jul 6, 2004.

[18] J. D. Weiland, W. Liu, and M. S. Humayun, "Retinal prosthesis," *Annual Review of Biomedical Engineering,* vol. 7 (1), pp. 361-401, 2005.

[19] D. W. Choi, "Glutamate neurotoxicity and diseases of the nervous system," *Neuron,* vol. 1 (8), pp. 623-34, Oct, 1988.

[20] E. Zrenner, "Will retinal implants restore vision?," *Science,* vol. 295 (5557), pp. 1022-1025, Feb 8, 2002.

[21] E. A. DeYoe, G. J. Carman, P. Bandettini, S. Glickman, J. Wieser, R. Cox, D. Miller, and J. Neitz, "Mapping striate and extrastriate visual areas in human cerebral cortex," *PNAS,* vol. 93 (6), pp. 2382-2386, Mar 19, 1996.

[22] M. S. Humayun, J. D. Weiland, G. Y. Fujii, R. Greenberg, R. Williamson, J. Little, B. Mech, V. Cimmarusti, G. Van Boemel, and G. Dagnelie, "Visual perception in a blind subject with a chronic microelectronic retinal prosthesis," *Vision Research,* vol. 43 (24), pp. 2573-2581, Nov, 2003.

[23] M. S. Humayun, R. Freda, I. Fine, A. Roy, G. Fujii, R. J. Greenberg, J. Little, B. Mech, J. D. Weiland, and E. de Juan, "Implanted intraocular retinal prosthesis in

six blind subjects," *Investigative Ophthalmology and Visual Science,* vol. 46, p. 1144, 2005.

[24] B. S. Wilson, C. C. Finley, D. T. Lawson, R. D. Wolford, D. K. Eddington, and W. M. Rabinowitz, "Better speech recognition with cochlear implants," *Nature,* vol. 352 (6332), pp. 236-8, Jul 18, 1991.

[25] Neurosurgerytoday.org, "Spinal cord injury," http://www.neurosurgerytoday.org/what/patient_e/spinal.asp (accessed: Jul 10, 2007).

[26] L. J. Noble and J. R. Wrathall, "Correlative analyses of lesion development and functional status after graded spinal-cord contusive injuries in the rat," *Experimental Neurology,* vol. 103 (1), pp. 34-40, Jan, 1989.

[27] National Spinal Cord Injury Statistical Center, "Spinal cord injury: Facts and figures at a glance," http://images.main.uab.edu/spinalcord/pdffiles/Facts06.pdf (accessed: Jul 10, 2007).

[28] National Institute of Neurological Disorders and Stroke, National Institutes of Health, "Spinal cord injury: Hope through research," http://www.ninds.nih.gov/disorders/sci/detail_sci.htm (accessed: Jul 10, 2007).

[29] J. W. Little, J. F. Ditunno, S. A. Stiens, and R. M. Harris, "Incomplete spinal cord injury: Neuronal mechanisms of motor recovery and hyperreflexia," *Archives of Physical Medicine and Rehabilitation,* vol. 80 (5), pp. 587-599, May, 1999.

[30] H. Gray, *Anatomy of the human body*, 20th ed. Philadelphia, PA, USA: Lea & Febiger, 1918.

[31] J. H. Burridge, P. N. Taylor, S. A. Hagan, D. E. Wood, and I. D. Swain, "The effects of common peroneal stimulation on the effort and speed of walking: A randomized controlled trial with chronic hemiplegic patients," *Clinical Rehabilitation,* vol. 11 (3), pp. 201-210, Aug, 1997.

[32] J. Rozman, R. Acimovicjanezic, I. Tekavcic, M. Kljajic, and M. Trlep, "Implantable stimulator for selective stimulation of the common peroneal nerve- a preliminary report," *Journal of Medical Engineering & Technology,* vol. 18 (2), pp. 47-53, Mar-Apr, 1994.

[33] P. Taylor, J. Burridge, A. Dunkerley, D. Wood, J. Norton, C. Singleton, and I. Swain, "Clinical audit of 5 years provision of the Odstock dropped foot stimulator," *Artificial Organs,* vol. 23 (5), pp. 440-442, May, 1999.

[34] K. W. Horch and G. S. Dhillon, *Neuroprosthetics theory and practice*. River Edge, NJ, USA: World Scientific, 2004.

[35] R. Brissot, P. Gallien, M. P. Le Bot, A. Beaubras, D. Laisne, J. Beillot, and J. Dassonville, "Clinical experience with functional electrical stimulation-assisted

gait with parastep in spinal cord-injured patients," *Spine,* vol. 25 (4), pp. 501-508, Feb 15, 2000.

[36] D. Graupe and K. H. Kohn, "Functional neuromuscular stimulator for short-distance ambulation by certain thoracic-level spinal-cord-injured paraplegics," *Surgical Neurology,* vol. 50 (3), pp. 202-207, Sep, 1998.

[37] P. S. Shurrager and R. A. Dykman, "Walking spinal carnivores," *Journal of Comparative and Physiological Psychology,* vol. 44 (3), pp. 252-262, 1951.

[38] R. D. de Leon, J. A. Hodgson, R. R. Roy, and V. R. Edgerton, "Full weight-bearing hindlimb standing following stand training in the adult spinal cat," *Journal of Neurophysiology,* vol. 80 (1), pp. 83-91, Jul, 1998.

[39] R. D. de Leon, J. A. Hodgson, R. R. Roy, and V. R. Edgerton, "Retention of hindlimb stepping ability in adult spinal cats after the cessation of step training," *Journal of Neurophysiology,* vol. 81 (1), pp. 85-94, Jan, 1999.

[40] E. C. Field-Fote, "Spinal cord control of movement: Implications for locomotor rehabilitation following spinal cord injury," *Physical Therapy,* vol. 80 (5), pp. 477-484, May, 2000.

[41] S. J. Harkema, B. H. Dobkin, and V. R. Edgerton, "Activity dependent plasticity after human spinal cord injury," *Experimental Neurology,* vol. 151 (1), pp. 156-156, May, 1998.

[42] J. R. Wolpaw and A. M. Tennissen, "Activity-dependent spinal cord plasticity in health and disease," *Annual Review of Neuroscience,* vol. 24, pp. 807-843, 2001.

[43] S. Grillner, "Neurobiological bases of rhythmic motor acts in vertebrates," *Science,* vol. 228 (4696), pp. 143-148, 1985.

[44] E. Bizzi, F. A. Mussaivaldi, and S. Giszter, "Computations underlying the execution of movement- a biological perspective," *Science,* vol. 253 (5017), pp. 287-291, Jul 19, 1991.

[45] L. Guevremont, J. A. Norton, and V. K. Mushahwar, "Physiologically based controller for generating overground locomotion using functional electrical stimulation," *Journal of Neurophysiology,* vol. 97 (3), pp. 2499-2510, Mar 1, 2007.

[46] T. Flash and B. Hochner, "Motor primitives in vertebrates and invertebrates," *Current Opinion in Neurobiology,* vol. 15 (6), pp. 660-666, Dec, 2005.

[47] M. C. Tresch and O. Kiehn, "Population reconstruction of the locomotor cycle from interneuron activity in the mammalian spinal cord," *Journal of Neurophysiology,* vol. 83 (4), pp. 1972-1978, Apr, 2000.

[48] A. J. Fong, L. L. Cai, C. K. Otoshi, D. J. Reinkensmeyer, J. W. Burdick, R. R. Roy, and V. R. Edgerton, "Spinal cord-transected mice learn to step in response to quipazine treatment and robotic training," *Journal of Neuroscience,* vol. 25 (50), pp. 11738-11747, Dec 14, 2005.

[49] V. K. Mushahwar, D. M. Gillard, M. J. A. Gauthier, and A. Prochazka, "Intraspinal microstimulation generates locomotor-like and feedback-controlled movements," *IEEE Transactions on Neural Systems and Rehabilitation Engineering,* vol. 10 (1), pp. 68-81, Mar, 2002.

[50] V. K. Mushahwar and K. W. Horch, "Proposed specifications for a lumbar spinal cord electrode array for control of lower extremities in paraplegia," *IEEE Transactions on Rehabilitation Engineering,* vol. 5 (3), pp. 237-243, 1997.

[51] T. Iwahara, Y. Atsuta, E. Garciarill, and R. D. Skinner, "Spinal-cord stimulation-induced locomotion in the adult cat," *Brain Research Bulletin,* vol. 28 (1), pp. 99-105, Jan, 1992.

[52] M. R. Dimitrijevic, Y. Gerasimenko, and M. M. Pinter, "Evidence for a spinal central pattern generator in humans," *Neuronal Mechanisms for Generating Locomotor Activity,* vol. 860, pp. 360-376, 1998.

[53] I. Lavrov, Y. P. Gerasimenko, R. M. Ichiyama, G. Courtine, Z. Hui, R. R. Roy, and V. R. Edgerton, "Plasticity of spinal cord reflexes after a complete transection in adult rats: Relationship to stepping ability," *Journal of Neurophysiology,* vol. 96 (4), pp. 1699-1710, Oct, 2006.

[54] L. McKerracher, G. Doucet, and S. Rossignol, *Spinal cord trauma: Neural repair and functional recovery*. Amsterdam; Boston: Elsevier, 2002.

[55] L. J. Seligman, "Electrical stimulation of the spinal cord: A critical review," *Pacing and Clinical Electrophysiology,* vol. 10 (1), pp. 176-179, Jan, 1987.

[56] E. Roederer, N. H. Goldberg, and M. J. Cohen, "Modification of retrograde degeneration in transected spinal axons of the lamprey by applied DC current," *Journal of Neuroscience,* vol. 3 (1), pp. 153-160, Jan 1, 1983.

[57] C. C. Stichel and H. W. Muller, "Experimental strategies to promote axonal regeneration after traumatic central nervous system injury," *Progress in Neurobiology,* vol. 56 (2), pp. 119-148, 1998.

[58] G. E. Moore, "Cramming more components onto integrated circuits (Reprinted from Electronics, pg 114-117, April 19, 1965)," *Proceedings of the IEEE,* vol. 86 (1), pp. 82-85, Jan, 1998.

[59] Y. C. Tai, L. S. Fan, and R. S. Muller, "IC-processed micro-motors: Design, technology, and testing," in Tech. Digest *IEEE Int. Conf. on MEMS*, Salt Lake City, UT, USA, pp. 1-6, 1989.

[60] K. A. Shaw, Z. L. Zhang, and N. C. Macdonald, "SCREAM-I - a single mask, single-crystal silicon, reactive ion etching process for microelectromechanical structures," *Sensors and Actuators A-Physical,* vol. 40 (1), pp. 63-70, Jan, 1994.

[61] M. J. Madou, *Fundamentals of microfabrication: The science of miniaturization*, 2nd ed. Boca Raton: CRC Press, 2002.

[62] A. Tooker, E. Meng, J. Erickson, Y. C. Tai, and J. Pine, "Biocompatible parylene neurocages," *IEEE Engineering in Medicine and Biology Magazine,* vol. 24 (6), pp. 30-33, Nov-Dec, 2005.

[63] G. T. A. Kovacs, N. I. Maluf, and K. E. Petersen, "Bulk micromachining of silicon," *Proceedings of the IEEE,* vol. 86 (8), pp. 1536-1551, Aug, 1998.

[64] J. M. Bustillo, R. T. Howe, and R. S. Muller, "Surface micromachining for microelectromechanical systems," *Proceedings of the IEEE,* vol. 86 (8), pp. 1552-1574, Aug, 1998.

[65] T. D. Kudrle, H. P. Neves, D. C. Rodger, and N. C. MacDonald, "A microactuated millimeter wave phase shifter," in Tech. Digest *Int. Conf. on Solid-State Sensors and Actuators*, Sendai, Japan, pp. 1276-1279 1999.

[66] X.-Q. Wang and Y.-C. Tai, "A normally closed in-channel micro check valve," in Tech. Digest *IEEE Int. Conf. on MEMS*, Miyazaki, Japan, pp. 68-73, 2000.

[67] Specialty Coating Systems, "Parylene knowledge: Discovery/history," http://www.scscoatings.com/parylene_knowledge/history.cfm (accessed: Jul 8, 2007).

[68] M. Szwarc, "Some remarks on the CH2=Benzene=CH2 molecule," *Discussions of the Faraday Society,* vol. 2, pp. 46-49, 1947.

[69] W. F. Gorham, "A new general synthetic method for preparation of linear poly-p-xylylenes," *Journal of Polymer Science Part A-1: Polymer Chemistry,* vol. 4 (12), pp. 3027-3039, 1966.

[70] L. Wolgemuth, "Crystal-clear coating covers components," *Medical Design,* vol. 6 (10), pp. 48-51, Dec 1, 2006.

[71] Specialty Coating Systems, "New SCS parylene HT conformal coating ideal for high-temperature applications," http://www.scscoatings.com/news/press_parylene-ht.cfm (accessed: Jun 24, 2007).

[72] Specialty Coating Systems, "Reliable protection for advanced electronics," www.sensorsexpo.com/exbdata/6698/brochures/SCS%20Electronic%20Coatings.pdf (accessed: Jun 24, 2007).

[73] Specialty Coating Systems, "Parylene knowledge: Specifications and properties," http://www.scscookson.com/parylene_knowledge/specifications.cfm (accessed: Jul 8, 2007).

[74] J. E. Mark, *Polymer data handbook*. New York: Oxford University Press, 1999.

[75] J.-H. Lee and W. Y. Ji, "Electrical and mechanical properties of silicone rubber for high voltage insulation," in Tech. Digest *International Conference on Properties and Applications of Dielectric Materials*, Nagoya, Japan, 2003.

[76] B. Bhushan and Z. Burton, "Adhesion and friction properties of polymers in microfluidic devices," *Nanotechnology,* vol. 16 (4), pp. 467-478, Apr, 2005.

[77] T. Stieglitz, W. Haberer, C. Lau, and M. Goertz, "Development of an inductively coupled epiretinal vision prosthesis," in Tech. Digest *Int. IEEE Eng. in Med. and Biol. Soc. Meet.*, San Francisco, CA, USA, pp. 4178-4181 Vol.6, 2004.

[78] A. C. Hoogerwerf and K. D. Wise, "A three-dimensional microelectrode array for chronic neural recording," *IEEE Transactions on Biomedical Engineering,* vol. 41 (12), pp. 1136-1146, 1994.

[79] Kishimoto Sangyo Co., Ltd., "diX conformal coatings," http://www.kisco-net.co.jp/kagaku/dix/kind_e.html (accessed: Jul 8, 2007).

[80] D. C. Rodger, J. D. Weiland, M. S. Humayun, and Y.-C. Tai, "Scalable high lead-count parylene package for retinal prostheses," *Sensors and Actuators B: Chemical,* vol. 117 (1), pp. 107-114, 2006.

[81] W. Li, D. C. Rodger, E. Meng, J. D. Weiland, M. S. Humayun, and Y.-C. Tai, "Flexible parylene packaged intraocular coil for retinal prostheses," in Tech. Digest *Int. IEEE-EMBS Microtech. in Med. and Bio. Meet.*, Okinawa, Japan, pp. 105-108, 2006.

[82] R. Kumar, D. Molin, L. Young, and F. Ke, "New high temperature polymer thin coating for power electronics," in Tech. Digest *APEC Meet.*, Anaheim, CA, USA, pp. 1247-1249, 2004.

[83] P. J. Chen, D. C. Rodger, M. S. Humayun, and Y. C. Tai, "Unpowered spiral-tube parylene pressure sensor for intraocular pressure sensing," *Sensors and Actuators A-Physical,* vol. 127 (2), pp. 276-282, Mar 13, 2006.

[84] P. J. Chen, D. C. Rodger, E. M. Meng, M. S. Humayun, and Y. C. Tai, "Surface-micromachined parylene dual valves for on-chip unpowered microflow regulation," *Journal of Microelectromechanical Systems,* vol. 16 (2), pp. 223-231, Apr, 2007.

[85] E. Meng, P.-J. Chen, D. Rodger, Y.-C. Tai, and M. Humayun, "Implantable parylene MEMS for glaucoma therapy," in Tech. Digest *Int. IEEE-EMBS Microtech. in Med. and Bio. Meet.*, Oahu, HI, USA, pp. 116-119, 2005.

[86] A. J. Bard and L. R. Faulkner, *Electrochemical methods: Fundamentals and applications*, 2nd ed. New York: Wiley, 2001.

[87] V. S. Bagotsky, *Fundamentals of electrochemistry*, 2nd ed. Hoboken, N.J.: Wiley-Interscience, 2006.

[88] J. Bockris, A. Reddy, and M. Gamboa-Aldeco, *Modern electrochemistry*, 2nd ed. New York: Plenum Press, 1998.

[89] L. S. Robblee and T. L. Rose, "The electrochemistry of electrical stimulation," in Tech. Digest *Int. IEEE Eng. in Med. and Biol. Soc. Meet.*, Philadelphia, PA, USA, pp. 1479-1480, 1990.

[90] L. A. Geddes, "Accuracy limitations of chronaxie values," *IEEE Transactions on Biomedical Engineering,* vol. 51 (1), pp. 176-181, Jan, 2004.

[91] J. E. B. Randles, "Kinetics of rapid electrode reactions," *Discussions of the Faraday Society,* vol. 1, pp. 11-19, 1947.

[92] Y. Yang and S. B. Khoo, "Fabrication of self-assembled monolayer of 8-mercaptoquinoline on polycrystalline gold electrode and its selective catalysis for the reduction of metal ions and the oxidation of biomolecules," *Sensors and Actuators B: Chemical,* vol. 97 (2-3), pp. 221-230, 2004.

[93] X. Beebe and T. L. Rose, "Charge injection limits of activated iridium oxide electrodes with 0.2 ms pulses in bicarbonate buffered saline," *IEEE Transactions on Biomedical Engineering,* vol. 35 (6), pp. 494-495, 1988.

[94] T. L. Rose and L. S. Robblee, "Electrical stimulation with Pt electrodes VIII. Electrochemically safe charge injection limits with 0.2 ms pulses," *IEEE Transactions on Biomedical Engineering,* vol. 37 (11), pp. 1118-1120, 1990.

[95] J. D. Weiland, D. J. Anderson, and M. S. Humayun, "In vitro electrical properties for iridium oxide versus titanium nitride stimulating electrodes," *IEEE Transactions on Biomedical Engineering,* vol. 49 (12), pp. 1574-1579, Dec, 2002.

[96] E. Guenther, B. Troger, B. Schlosshauer, and E. Zrenner, "Long-term survival of retinal cell cultures on retinal implant materials," *Vision Research,* vol. 39 (24), pp. 3988-3994, 1999.

[97] W. Mokwa, "MEMS technologies for epiretinal stimulation of the retina," *Journal of Micromechanics and Microengineering,* vol. 14 (9), pp. S12-S16, Sep, 2004.

[98] S. I. Fried, H. A. Hsueh, and F. S. Werblin, "A method for generating precise temporal patterns of retinal spiking using prosthetic stimulation," *Journal of Neurophysiology,* vol. 95 (2), pp. 970-978, Feb 1, 2006.

[99] A. K. Ahuja, M. R. Behrend, M. Kuroda, M. S. Humayun, and J. D. Weiland, "Spatial response properties of electrically stimulated retina," *Investigative Ophthalmology and Visual Science,* vol. 48 (5), p. 4444, May 10, 2007.

[100] P. Nasiatka, A. Ahuja, N. Stiles, M. Hauer, R. N. Agrawal, R. Freda, D. Guven, M. S. Humayun, J. D. Weiland, and A. R. Tanguay, Jr., "Intraocular camera for retinal prostheses," *Investigative Ophthalmology and Visual Science,* vol. 46 (5), p. 5277, May 1, 2005.

[101] P. Nasiatka, M. Hauer, N. Stiles, L. Lue, S. Takahashi, R. Agrawal, R. Freda, M. Humayun, J. Weiland, and A. Tanguay, Jr., "Intraocular camera for retinal prostheses," *Investigative Ophthalmology and Visual Science,* vol. 47 (5), p. 3186, May 1, 2006.

[102] W. Liu, M. Sivaprakasam, P. R. Singh, R. Bashirullah, and G. Wang, "Electronic visual prosthesis," *Artificial Organs,* vol. 27 (11), pp. 986-995, 2003.

[103] W. Liu, K. Vichienchom, M. Clements, S. C. DeMarco, C. Hughes, E. McGucken, M. S. Humayun, E. De Juan, J. D. Weiland, and R. Greenberg, "A neuro-stimulus chip with telemetry unit for retinal prosthetic device," *Solid-State Circuits, IEEE Journal of,* vol. 35 (10), pp. 1487-1497, 2000.

[104] M. Sivaprakasam, L. Wentai, M. S. Humayun, and J. D. Weiland, "A variable range bi-phasic current stimulus driver circuitry for an implantable retinal prosthetic device," *Solid-State Circuits, IEEE Journal of,* vol. 40 (3), pp. 763-771, 2005.

[105] Clariant, "AZ 5214E Image Reversal Photoresist Product Data Sheet," http://groups.mrl.uiuc.edu/dvh/pdf/AZ5214E.pdf (accessed: Jul 8, 2007).

[106] "Photolithography process," http://www.mse.vt.edu/faculty/hendricks/mse4206/GaAsTEK/Lithography/ladv.htm (accessed: Jul 8, 2007).

[107] Microchem Corp., "LOR and PMGI Resists Product Data Sheet," http://www.microchem.com/products/pdf/PMGI-Resists-data-sheetV-rhcedit-102206.pdf (accessed: Jul 8, 2007).

[108] C. Pang, J. G. Cham, Z. Nenadic, S. Musallam, Y.-C. Tai, J. W. Burdick, and R. A. Andersen, "A new multi-site probe array with monolithically integrated parylene flexible cable for neural prostheses," in Tech. Digest *Int. Conf. IEEE-EMBS 2005*, San Francisco, CA, USA, pp. 7114-7117, 2005.

[109] E. Meng and Y.-C. Tai, "Parylene etching techniques for microfluidics and bioMEMS," in Tech. Digest *IEEE Int. Conf. on MEMS*, Miami, FL, USA, pp. 568-571, 2005.

[110] T. A. Harder, Y. Tze-Jung, H. Qing, S. Chi-Yuan, and T. Yu-Chong, "Residual stress in thin-film parylene-C," in Tech. Digest *IEEE Int. Conf. on MEMS*, Las Vegas, NV, USA, pp. 435-438, 2002.

[111] J. J. Whalen, J. D. Weiland, and P. C. Searson, "Electrochemical deposition of platinum from aqueous ammonium hexachloroplatinate solution," *Journal of the Electrochemical Society,* vol. 152 (11), pp. C738-C743, 2005.

[112] C. A. Curcio and K. A. Allen, "Topography of ganglion-cells in human retina," *Journal of Comparative Neurology,* vol. 300 (1), pp. 5-25, Oct, 1990.

[113] S. B. Brummer and M. J. Turner, "Electrical stimulation with Pt electrodes: II-estimation of maximum surface redox (theoretical non-gassing) limits," *IEEE Transactions on Biomedical Engineering,* vol. 24 (5), pp. 440-443, 1977.

[114] S. B. Brummer and M. J. Turner, "Electrical stimulation with Pt electrodes: I-A method for determination of "Real" Electrode areas," *IEEE Transactions on Biomedical Engineering,* vol. 24 (5), pp. 436-439, 1977.

[115] E. Slavcheva, R. Vitushinsky, W. Mokwa, and U. Schnakenberg, "Sputtered iridium oxide films as charge injection material for functional electrostimulation," *Journal of the Electrochemical Society,* vol. 151 (7), pp. E226-E237, 2004.

[116] L. S. Robblee, J. L. Lefko, and S. B. Brummer, "Activated Ir- an electrode suitable for reversible charge injection in saline solution," *Journal of the Electrochemical Society,* vol. 130 (3), pp. 731-733, 1983.

[117] M. A. El Khakani, M. Chaker, and B. Le Drogoff, "Iridium thin films deposited by radio-frequency magnetron sputtering," *Journal of Vacuum Science & Technology A-Vacuum Surfaces and Films,* vol. 16 (2), pp. 885-888, Mar-Apr, 1998.

[118] J. D. Weiland, S. Cogan, and M. S. Humayun, "Micro-machined, polyimide stimulating electrodes with electroplated iridium oxide," in Tech. Digest *Int. IEEE Eng. in Med. and Biol. Soc. Meet.*, Atlanta, GA, USA, p. 378, 1999.

[119] R. D. Meyer, S. F. Cogan, T. H. Nguyen, and R. D. Rauh, "Electrodeposited iridium oxide for neural stimulation and recording electrodes," *IEEE Transactions on Neural Systems and Rehabilitation Engineering,* vol. 9 (1), pp. 2-11, 2001.

[120] G. T. A. Kovacs, C. W. Storment, and J. M. Rosen, "Regeneration microelectrode array for peripheral nerve recording and stimulation," *IEEE Transactions on Biomedical Engineering,* vol. 39 (9), pp. 893-902, 1992.

[121] S. Rogojevic, J. A. Moore, and W. N. Gill, "Modeling vapor deposition of low-k polymers: Parylene and polynaphthalene," *Journal of Vacuum Science & Technology A,* vol. 17 (1), pp. 266-274, Jan-Feb, 1999.

[122] P. W. Atkins, *General chemistry*. New York: Scientific American Books, 1989.

[123] A. P. Chandran, K. Oda, H. Shibasaki, and M. Pisharodi, "Spinal somatosensory evoked potentials in mice and their developmental changes," *Brain Dev,* vol. 16 (1), pp. 44-51, Jan-Feb, 1994.

[124] Y. Xu, Y.-C. Tai, A. Huang, and C.-M. Ho, "IC-integrated flexible shear-stress sensor skin," *Microelectromechanical Systems, Journal of,* vol. 12 (5), pp. 740-747, 2003.

[125] J. T. Butler, V. M. Bright, and J. H. Comtois, "Advanced multichip module packaging of microelectromechanical systems," in Tech. Digest *Int. Conf. on Solid-State Sensors and Actuators*, Chicago, IL, USA, pp. 261-264, 1997.

[126] W. Daum, W. E. Burdick, and R. A. Fillion, "Overlay high-density interconnect: A chips-first multichip module technology," *Computer,* vol. 26 (4), pp. 23-29, 1993.

[127] J. J. Licari and L. A. Hughes, *Handbook of polymer coatings for electronics : Chemistry, technology, and applications*, 2nd ed. Park Ridge, NJ, USA: Noyes Publications, 1990.

[128] R. R. Tummala, *Fundamentals of microsystems packaging*. New York: McGraw-Hill, 2001.

[129] D. C. Rodger and Y. C. Tai, "Microelectronic packaging for retinal prostheses," *IEEE Engineering in Medicine and Biology Magazine,* vol. 24 (5), pp. 52-57, Sep-Oct, 2005.

[130] D. C. Rodger, J. D. Weiland, M. S. Humayun, and Y.-C. Tai, "Scalable flexible chip-level parylene package for high lead count retinal prostheses," in Tech. Digest *Int. Conf. Solid-State Sensors, Actuators and Microsystems*, Seoul, Korea, pp. 1973-1976, 2005.

[131] H. Sharifi, T. Y. Choi, and S. Mohammadi, "Self-aligned wafer-level integration technology with high-density interconnects and embedded passives," *IEEE Transactions on Advanced Packaging,* vol. 30 (1), pp. 11-18, Feb, 2007.

[132] G. E. Loeb, R. A. Peck, W. H. Moore, and K. Hood, "BION system for distributed neural prosthetic interfaces," *Medical Engineering & Physics,* vol. 23 (1), pp. 9-18, Jan, 2001.

[133] W. Li, Personal communication, Jun 2007.

[134] W. Li, D. C. Rodger, J. D. Weiland, M. S. Humayun, and Y. C. Tai, "Integrated flexible ocular coil for power and data transfer in retinal prostheses," in Tech. Digest *Int. IEEE Eng. in Med. and Biol. Soc. Meet.*, Shanghai, China, pp. 1028-1031, 2005.